Hybrid Electromagnetic Vibration Isolation Systems

by

Ehsan Asadi

A thesis
presented to the University of Waterloo
in fulfillment of the
thesis requirement for the degree of
Doctor of Philosophy
in
Mechanical and Mechatronics Engineering

Waterloo, Ontario, Canada, 2017

Examining Committee Membership

The following served on the Examining Committee for this thesis. The decision of the Examining Committee is by majority vote.

External Examiner: Jun Yang
Professor, Dept. of Mechanical and Materials Engineering,
Western University

Supervisor(s): Mir Behrad Khamesee, and Amir Khajepour
Professor, Dept. of Mechanical and Mechatronics Engineering,
University of Waterloo

Internal Member: Soo Jeon
Professor, Dept. of Mechanical and Mechatronics Engineering,
University of Waterloo

Internal Member: Ehsan Toyserkani
Professor, Dept. of Mechanical and Mechatronics Engineering,
University of Waterloo

Internal-External Member: Ehab El-Saadany
Professor, Dept. of Electrical and Computer Engineering,
University of Waterloo

Abstract

Traditionally, dynamic systems are equipped with passive technologies like viscous shock absorbers and rubber vibration isolators to attenuate disturbances. Passive elements are cost effective, simple to manufacture, and have a long life span. However, the dynamic characteristics of passive devices are fixed and tuned for a set of inputs or system conditions. Thus in many applications when variation of input or system conditions is present, sub-optimal performance is realized. The other fundamental flaw associated with passive devices is that they expel the undesired kinetic energy as heat. Recently, the introduction of electromagnetic technologies to the vibration isolation systems has provided researchers with new opportunities for realizing active/semi-active vibration isolation systems with the additional benefit of energy regeneration (in semi-active mode). Electromagnetic vibration isolators are often suffer from a couple of shortcomings that precludes their implementations in many applications. Examples of these short comings include bulky designs, low force density, high energy consumption (in active mode), and fail-safe operation problem. This PhD research aims at developing optimal hybrid-electromagnetic vibration isolation systems to provide active/semi-active and regenerative vibration isolation for various applications. The idea is to overcome the aforementioned shortcomings by integrating electromagnetic actuators, conventional damping technologies, and stiffness elements into single hybrid packages. In this research, for both semi-active and active cases, hybrid electromagnetic solutions are proposed.

In the first step of this study, the concept of semi-active hybrid damper is proposed and experimentally tested that is composed of a passive hydraulic and a semi-active electromagnetic components. The hydraulic medium provides a bias and fail-safe damping force while the electromagnetic component adds adaptability and energy regeneration to the hybrid design. Based on the modeling and optimization studies, presented in this work, an extended analysis of the electromagnetic damping component of the hybrid damper is presented which can serve as potent tool for the designers who seek maximizing the adaptability (and regeneration capacity) of the hybrid damper. The experimental results (from the optimized design) show that the damper is able to produce damping coefficients of 1300 and 0–238 Nsm^1 through the viscous and electromagnetic components, respectively. In particular, the concept of hybrid damping for the application of vehicle suspension system is studied. It is shown that the whole suspension system can be adjusted such that the implementation of the hybrid damper, not only would not add any adverse effects to the main functionally of the suspension, but it would also provide a better dynamics, and enhance the vehicle fuel consumption (by regenerating a portion of wasted vibration energy).

In the second step, the hybrid damper concept is extended to an active hybrid electromagnetic vibration isolation systems. To achieve this target, a passive pneumatic spring is fused together with an active electromagnetic actuator in a single hybrid package. The active electromagnetic component maintains a base line stiffness and support for the system, and also provides active vibration for a wide frequency range. The passive pneumatic spring makes the system fail-safe, increases the stiffness and support of the system for larger masses and dead loads, and further guarantees a very low transmissibility at high frequencies. The FEM and experimental results confirmed the high force density of the proposed electromagnetic component, comparing to a voice coil of similar size. In the proposed design, with a diameter of $\sim 125\ mm$ and a height of $\sim 60\ mm$, a force variation of $\sim 318\ N$ is obtained for the currents of $I = \pm 2\ A$. Furthermore, it is demonstrated that the proposed actuator has a small time constant (ratio of inductance to resistance for the coils) of less than $5.2\ ms$, with negligible eddy current effect, making the vibration isolator suitable for wide bandwidth applications. According to the results, the active controllers are able to enhance the performance of the passive elements by up to 80% and 95% in terms of acceleration and force transmissibilities, respectively.

Acknowledgements

In the Name of Allah the most Compassionate, ever Compassionate. In summary I am thankful. Thankful for where I am and what I have been given in my life.

First and above all, I praise Allah, God Almighty, for providing me all the life opportunities and for guiding me all the way to proceed successfully.

I am extremely grateful to my parents, Abdolazim Asadi and Farkhondeh Mohammadi, for their love, prayers, caring and incredible sacrifices and continuing support for educating and preparing me for my future. My appreciation likewise extends to my brother Ali, my sister Nahid, my uncle Mohammad and my aunt Mitra for unflagging love and support throughout my life. There are not enough words in the whole world for me to describe how much I am grateful for having the most lovely family.

This dissertation would not have been possible without the guidance and the help of several individuals who in one way or another contributed and extended their valuable assistance in the preparation and completion of this study. First and foremost, my utmost gratitude goes to my supervisors Prof. Mir Behrad Khamesee and Prof. Amir Khajepour, for their inspirations and guidance throughout my research. I am sure that I could not have been here without their help, and I know that I could not ask for better supervisors. So truly THANK YOU for everything. I am also indebted to defense committee, Prof. Yang, Prof. Jeon, Prof. Toyserkani, and Prof. El-Saadany for kindly reviewing this thesis, and serving in my PhD committee.

My PhD journey finally came to an end, and I have to say that it's been a long but exciting journey doing my PhD in Waterloo. I wish I could say thank you to all the great people I feel lucky and happy for having them as friends. In particular, I would like to thank Anis, Zahra, Hannah, Hanieh, Mohammad, Nilgoun, Nazy, Mehdi, Pooneh, Alis, Mansour, Reza, Meysams, and Behrouz; Hassan, Mohammad, Thamir, Xiaodong, Roberto, Henry, and Sam; Emad, Abdollah, Moslem, Hamed, Faegheh, Saeideh, Atefeh, and Maryyeh; Siamak, Ali, Alireza, Elham, and Mohammad; Hadi, Saeid, Amirs, and all other friends from uw-quran session; Ebrahim, Alis, Alireza, and Fariborz; Hamid, Emitis, Farnaz, Mehdi, Reza, Hossein, Saber, Moein, and Elaheh; and finally Ehsan, Amin, Masoud, Milads, Meysam and Amirhossein for their friendship and help in the past few years.

Dedication

To my beloved parents.

Table of Contents

List of Tables

List of Figures

Nomenclature

Chapter 1

F_E	force contribution of the electromagnetic component
F_t	total damping force
f_t	transmitted force to fixture
F_v	force contribution of the viscous component
F_{air}	pneumatic spring force
$F_{e_{i,j}}$	the electromagnetic force from stack i to j
F_{ext}	external force on the top stack
g	gravitational acceleration
m	external mass
m_i	mass of stack i
m_{ext}	external mass (dead load) on the top stack
R_{ext}	apparent external resistance
T_a	acceleration transmissibility
T_f	force transmissibility
x_i	vertical position of stack i
$\ddot{x}_m$	transmitted acceleration to mass m

$\ddot{x}_s$	acceleration of oscillating body

Chapter 2

α	ratio of $\frac{C_L}{C_R}$
λ	magnetic flux linkage
μ	conductivity of the wire
μ_0	permeability of free space
μ_{Co}	relative permeability of copper
μ_{Fe}	relative permeability of iron
μ_{rec}	recoil permeability of the permanent magnets
ω	angular frequency of the excitation
ϕ	flux through each turn of coil
σ	conductivity of the wire
τ	summation of the thickness of iron pole piece and permanent magnet
τ_c	thickness of coils in the electromagnetic component
τ_i	thickness of iron pole pieces in the electromagnetic component
τ_m	thickness of permanent magnets in the electromagnetic component
θ	phase shift between input displacement and output force
A	excitation amplitude
A	wire cross section area
A_i	area of part i
A_{ij}	cross-sectional area size of the flow canal between sections i and j
AWG	american wire gauge
B	magnetic flux density

B_{rec}	remnant flux density of the permanent magnets
C_k	equals to k_v of the preliminary optimization design with Scf=1
C_L	equals to L_{cOil} of the preliminary optimization design with Scf=1
C_R	equals to R_{cOil} of the preliminary optimization design with Scf=1
C_{ij}	coefficient of discharge between sections i and j
D_p	diameters of piston
D_r	diameters of central rod
D_{it}	diameter of inner tube
f	excitation frequency
F_E	electromagnetic force
H	magnetic field strength
i	magnitude of the induced current
K	oil Bulk modulus
k_f	force constant
k_v	voltage constant
l	path of the induced current
L_{coil}	coil inductance
N	number of turns in a coil
P_E	regenerated power
P_i	pressure in section i
P_k	minimum pressure required to open the valve
P_{at}	atmosphere pressure
Q_{ij}	volume flow rate from section i to j

r_a	inner radius of coils in the electromagnetic component
R_c	internal resistance of the coil
r_c	outer radius of coils in the electromagnetic component
r_p	outer radius of iron conductor tube in the electromagnetic component
r_s	radius of the shaft in the electromagnetic component
r_w	outer radius of permanent magnets in the electromagnetic component
r_{avg}	average radius of the coil
R_{coil}	coil resistance
R_{ext}	external load (resistance)
r_{fv}	ratio of force over velocity
Sc_f	scale factor
V_i	volume of section i
V_{emf}	electromotive force
x	damper displacement
ρ_0	oil density at atmosphere pressure
ρ_{ij}	oil density
F_{Esin}	electromagnetic force for a sinusoidal displacement input
F_{EV_0}	electromagnetic force for a constant velocity input

Chapter 3

r	equals to $\frac{R_{ext}}{R_{coil}}$
R_{coil}	summation of the resistance of coils in any of the phases in the damper
R_{ext}	resistance of one of the branches of the external star/delta loads
V	voltage

z	gauss meter vertical location relative to the shaft iron pole pieces and magnets

Chapter 4

α	equals to $\frac{L_c}{R_c}$
β	a constant used in road modeling process
$\eta_{D/S}$	ratio of the dynamic force to the static force between tire and ground
σ	cost function
C_s	hydraulic damping coefficient
f_1	first cost function: related to the ride comfort quality
f_2	second cost function: related to the road holding quality
f_3	third cost function: related to the regenerated power
f_e	electromagnetic force of the damper
$G(s)$	low pass filter represent used in road modeling process
G_r	road-roughness coefficient
H	transfer function of the desired output when unit white noise is applied as input
I	current of generator coils
k_s	suspension stiffness
k_t	tire stiffness
K_v	machine constant
L_c	coil inductance
m_s	sprung mass
m_u	unsprung mass
P	regenerated electrical power
R_c	coil resistance

R_l	load (external) resistance
R_t	summation of R_l and R_c
S_0	a constant used in road modeling process
S_{PSD}	displacement power spectral density (PSD)
V	vehicle speed
v	spatial frequency for road modeling
v_0	spatial frequency for road modeling
W_{2631}	filter for weighting vibrations, according to human vibration sensitivity curves
x_s	displacement of sprung mass
x_u	displacement of unsprung mass
y	displacement of ground
Z_1	transfer function representing the ride comfort quality
Z_2	transfer function representing the road holding quality
Z_3	transfer function representing the regenerated power

Chapter 5

γ	surface constant of sliding mode controller for acceleration transmissibility case
λ	surface constant of sliding mode controller for force transmissibility case
σ_a	sliding surface for acceleration transmissibility
σ_f	sliding surface for force transmissibility
A_e	effective area of pneumatic spring
AWG	American Wire Gauge
B_r	magnetic flux density in radial direction
B_z	magnetic flux density in vertical direction

B_{rem}	remnant magnetic flux density of magnet
c_c	force coefficients of viscous frictions
c_r	force coefficients of coulomb frictions
$E(P)$	complete second elliptical integral
F_e	electromagnetic force
F_p	pneumatic force
F_r	friction force
F_{ed}	desired electromagnetic force, used in feedback linearization controller
F_{n0}	portion of the static force compensated by pneumatic spring
F_{st}	static load
g_{amp}	voltage to current conversion gain of the amplifier
I_{ed}	desired coil currents, used in feedback linearization controller
$K(P)$	complete first elliptical integral
K_n	number of coils energized by the amplifier
$k_{D,f}$	derivative coefficient for force transmissibility case
$k_{I,a}$	integral coefficient for acceleration transmissibility case
$k_{I,f}$	integral coefficient for force transmissibility case
$k_{P,a}$	proportional coefficient for acceleration transmissibility case
$k_{P,f}$	proportional coefficient for force transmissibility case
n	polytropic index of the gas
P_0	initial pressure if pneumatic spring
P_{at}	atmospheric pressure
R	flow resistance coefficient

r	radial position in cylindrical coordinate
V_a	volume of pneumatic spring
V_b	volume of auxiliary tank
V_c	command signal of the controller, sent to the amplifier
$V_{FL,f}$	control signal of feedback linearization controller for force transmissibility
$V_{i,j}$	control signal determined by the controller i for isolation case j
V_{pe}	penalty function
$V_{PI,a}$	control signal of proportional-integral controller for acceleration transmissibility
$V_{SMC,a}$	control signal of sliding mode controller for acceleration transmissibility
$V_{SMC,f}$	control signal of sliding mode controller for force transmissibility
W_0	specific weight of gas
x	relative displacement of top to bottom stacks
x_m	top stack displacement
x_s	bottom stack displacement
y	auxiliary variable in Nishimura model
z	distance between top and bottom stacks
z	vertical position in cylindrical coordinate
z_0	initial distance between top and bottom stacks

Chapter 6

AWG	american wire gauge
L_c	apparent inductance
R_c	coil resistance

Chapter 1

Introduction and Literature Review

1.1 Problem Statement

Hybrid electromagnetic vibration isolation systems are aimed at realizing new possibilities to the vibration isolation problem by combining electromagnetic technology with other traditional vibration isolation systems. The result is improvement of the performance of dynamic systems by realizing optimal vibration isolation. Traditionally, dynamic systems are equipped with passive technologies like viscous shock absorbers to attenuate disturbances. Passive elements are cost effective, simple to manufacture, and have a long life span. However, the dynamic characteristic of passive devices are fixed and tuned for a set of inputs or system conditions. Thus in many applications when variation of input or system conditions is present, sub-optimal performance is realized. Theoretically it is possible to overcome the performance shortcoming of passive systems by introducing force variability to the systems. Using more recently developed technologies, vibration isolators can be designed to adapt their characteristics to the conditions of the environment and system dynamically. This force variability allows for mitigation and optimal control of input disturbances.

Passive vibration isolation systems include a passive stiffness (e.g spiral springs) and a passive damping (e.g hydraulic shock absorber) mechanisms. In response to the functionality concerns of passive devices, different vibration isolation systems with controllable forces have been introduced to the market. These controllable systems are categorized into active and semi-active ones. A semi-active vibration isolation system is able to adjust its damping coefficient, C, in real time but without adding any work into the system. An active system, on the other hand, uses active forces to exert work and energy into the system, and can, in real time, control both stiffness, K, and damping, C, of the vibration isolation system. Active systems like electromagnetic active actuators and pneumatic/hydraulic cylinders attenuate the undesired vibration by inputting energy into the system. While providing superior efficiency and strong controllability, active devices suffer mainly from higher costs and power consumption that limit their applications to special systems. Furthermore, some of the active systems are not fail-safe and in case of electronics failure, they are not able to produce enough damping forces. Semi-active devices, on the other hand, are characterized as variable damping systems that are controlled through a low power signal. MR-dampers, ER-dampers and solenoid valve dampers are examples of technologies developed based on the semi-active definition. These technologies can regulate their damping properties over an acceptable force range. The energy consumption of semi-active systems is much lower than their active counterparts; however, they are still not helpful with respect to the system fuel (energy) economy.

With the employment of electromagnetic technology, it is possible to develop force variable systems with a power regeneration feature (in semi-active mode) [6]. Electromagnetic devices have a small time constant and therefore can be used for high bandwidth applications. However, there are some limitations associated with these devices that should be addressed. Electromagnetic based actuators generally are not fail-safe. They suffer from large weights and bulky designs. Downsized electromagnetic actuators, on the other hand, produce limited forces, specially in regenerative mode.

1.2 Conceptual Designs for Hybrid Electromagnetic Vibration Isolation systems

A potential approach to overcome the performance limitations of electromagnetic devices is to combine them with other technologies. In the follow, two conceptual hybrid designs are proposed for semi-active and active cases where electromagnetic components are combined with passive elements in single hybrid packages.

1.2.1 Semi-active Hybrid Electromagnetic Damper: Conceptual Design

In order to resolve the fail-safe and force range issues, which the electromagnetic dampers are associated with, it is proposed that the linear electromagnetic topology is chosen as the basis of a new design with the integration of a viscous medium for additional damping

(Figure 1.1). The proposed hybrid design will resolve the power consumption issue due to the electromagnetic machine capability to be run in a semi-active configuration. Therefore, comparing to the currently available semi-active dampers in the market (MR, ER and SV dampers), the proposed hybrid damper has the advantageous of zero power requirements, and furthermore has the possibility of energy regeneration. Making the damper fail-safe is realized by the integration of a viscous medium. In comparison with the semi-active linear and rotary electromagnetic dampers (mainly developed in academic sectors), that have weight and volume problems, the hybrid damper is able to provide a large sufficient baseline damping force, by the viscous component that prevents the hybrid damper to have bulky and heavy designs, makes the damper suitable for real use, and guarantees a fail-safe operation. Also the problem of fluid degradation in MR and ER dampers does not exist in the hybrid damper. Finally, the proposed design benefits from the high performance characteristics of the linear electromagnetic dampers: The electromagnetic dampers have low static friction, and further their damping force can be easily controlled through custom power electronics.

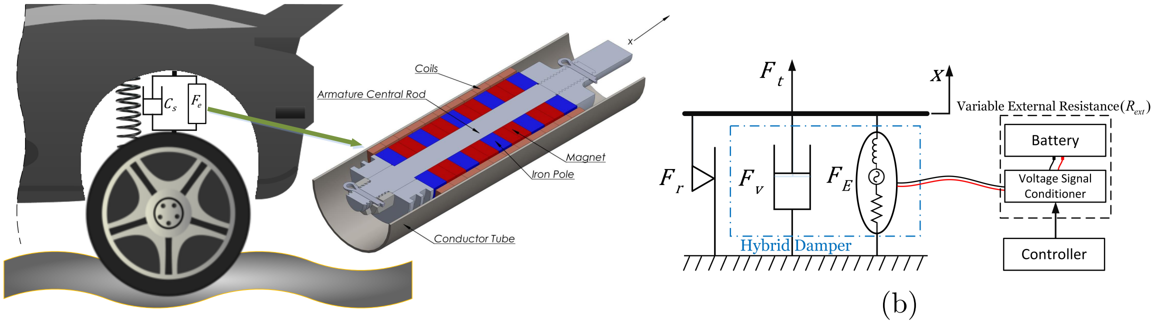

(a)

(b)

Figure 1.1: Concept of semi-active hybrid electromagnetic damper, a: a quarter car equipped with a hybrid electromagnetic damper (the zoomed part represents the schematic sectioned view of electromagnetic component), and b: a schematic view of a hybrid damper.

One of the main challenges in designing the hybrid damper, is that by combining the hydraulic and electromagnetic dampers in a single package, the size and weight of the damper tend to increase, and this is while the damper is required to fit inside the designated space, and is recommended to weigh less than 7 Kg [7]. In the present work, these requirements are considered throughout the modeling and design processes, to ensure that they are met by the final prototype.

The total damping force (F_t) of the device expressed by:

$$F_t = F_v + F_E + F_r \tag{1.1}$$

where F_v and F_E are the force contributions of the viscous and electromagnetic components of the hybrid damper respectively, and F_r is the mechanical friction force. The rates of the electromagnetic force (F_E) and regenerated power at a given excitation condition depend on the apparent external resistance (R_{ext}) of all the electronics connected to the electromagnetic coils. Generally, by increasing R_{ext} from zero (short circuited) to infinite (open loop) the electromagnetic force drops from a maximum value to zero. Implementing a voltage signal conditioner (discussed in Chapters 2 and 3) gives us the opportunity to adjust R_{ext} and, thus adapt the damper dynamic behavior based on the road condition and driving mode.

In Chapters 2 and 3, a hybrid semi-active actuator is developed and analysed based on electromagnetic and hydraulic technologies. The device is proposed as regenerative and adaptive damping mechanism, however, it can also be employed as active actuator by inducing currents in the electromagnetic coils. The fabricated prototype, is developed for vehicle suspension system, and designed to fit inside in the allocated space in the suspension system.

1.2.2 Active Hybrid Electromagnetic Vibration Isolator: Conceptual Design

As the first step toward designing an active hybrid vibration isolator, it is required to identify the design requirements for the system, and accordingly propose a conceptual solution to address those requirements. The proposed concept, will then be used as a guideline for the design process presented in the rest of this work.

The design criteria for the active hybrid vibration isolator are listed as follows:

1. A fast response device with a wide bandwidth that can be utilized in a wide range of actuation frequencies.
2. A low-profile design that can be installed in many locations with space limitations, yet with a high-density active force for implementation in heavy duty applications.
3. A modular device that could be easily reconfigured for applications with different stroke requirements.

4. A fail-safe operation for sensitive applications.

Starting with the first criterion, an electromagnetic component is employed to provide active force with a wide bandwidth. In order to address the second criterion, a device with low aspect ratio is proposed for this work. The electromagnetic component is required to be carefully designed and optimized to ensure high-density active force. Designing an electromagnetic actuator with these features is a challenging task as the current electromagnetic devices are often bulky with low-density active forces. In fact, satisfying the second criterion would be the main contribution of this work.

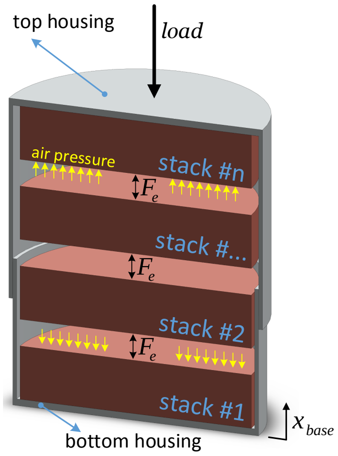

Figure 1.2: Active hybrid electromagnetic vibration isolator, a combination of an active electromagnetic actuator and a passive pneumatic spring.

Figure 1.2 explains how the last two criteria are addressed. This figure represents an electromagnetic based vibration isolator with a hybrid and modular design. The electromagnetic components include a number of cylindrical stacks, positioned in a vertical arrangement. The stacks employ contactless magnetic springs to float at a distance, on the top of each other, providing an stiffness for the device. Each stack has an electromagnetic coil that would be energized to affect the magnetic field and change the distance between the stacks, generating the actuation force. Once an stack is designed, the device can be reconfigured for other applications, with different stroke requirements, simply by including more or fewer number of stacks. While the magnetic springs provide the base stiffness, the incorporation of a pneumatic spring in the design allows for further adjustment in stiffness for heavier loads. The air pressure of the pneumatic spring is selected based on the applocationa and magnitude of static (dead) load. During the development, if there is a changes in dead load size and mass, the hybrid vibration isolator can be easily reused, by adjusting the gas pressure of the pneumatic spring. The hybrid design also guarantees a fail-safe operation. In case of failure in the electronics, the hybrid device would still operate as a passive unit.

Considering a hybrid design with n stacks, and the first stack being mounted to the foundation, the equation of motion can be written as:

$$\begin{aligned} m_2\ddot{x}_2 =& F_{e_{1,2}} - F_{e_{2,3}} - m_2 g \\ &\vdots \\ m_{n-1}\ddot{x}_{n-1} =& F_{e_{n-2,n-1}} - F_{e_{n-1,n}} - m_{n-1} g \\ \left(m_n + m_{ext}\right)\ddot{x}_n =& F_{e_{n-1,n}} + F_{air} + F_{ext} - m_n g \end{aligned} \tag{1.2}$$

where, m_i, x_i are the mass and vertical position of stack i, respectively. $F_{e_{i,j}}$ is the electromagnetic force from stack i to j, F_{air} is the pneumatic spring force, g is the gravitational acceleration, and finally, m_{ext} and F_{ext} are the external mass (dead load) and force on the top stack, respectively.

The above equation can be written in the matrix form as:

$$\begin{aligned} \begin{bmatrix} m_2 & & & \\ & \ddots & & \\ & & m_{n-1} & \\ & & & m_n + m_{ext} \end{bmatrix} \begin{bmatrix} \ddot{x}_2 \\ \vdots \\ \ddot{x}_{n-1} \\ \ddot{x}_n \end{bmatrix} &= \begin{bmatrix} 1 & -1 & 0 & \cdots & 0 \\ 0 & 1 & -1 & \ddots & \vdots \\ \vdots & \ddots & \ddots & \ddots & 0 \\ \vdots & & \ddots & 1 & -1 \\ 0 & \cdots & \cdots & 0 & 1 \end{bmatrix} \\ \times \begin{bmatrix} F_{e_{1,2}} \\ \vdots \\ F_{e_{n-2,n-1}} \\ F_{e_{n-1,n}} \end{bmatrix} &+ \begin{bmatrix} 0 \\ \vdots \\ 0 \\ 1 \end{bmatrix} \left[F_{air} + F_{ext}\right] - \begin{bmatrix} m_2 \\ \vdots \\ m_{n-1} \\ m_n + m_{ext} \end{bmatrix} g \end{aligned} \tag{1.3}$$

Equation (2) can be represented in simple matrix form as follows:

$$\left[M\right]\left[\ddot{x}\right] = \left[A\right]\left[F\right] + \left[B\right]\left[F_{air} + F_{ext}\right] - \left[M\right] g \tag{1.4}$$

In Chapters 5 and 6, based on the proposed idea, the design, prototyping and experimental evaluation of a new electromagnetic-pneumatic actuator is presented. The design, discussed in these chapters, has only two stacks (called bottom and top stacks), however, the discussions are held true for a general design with more number of stacks. The low-profile actuator is purposed to have a diameter of $\sim 120\ mm$, a maximum aspect ratio of ~ 0.5, and a maximum time constant of $10ms$. The nominal load mass for the isolator is considered to be $\sim 60\ kg$ or $\sim 600\ N$.

1.3 Literature Review

1.3.1 Semi-active Hybrid Electromagnetic Damper

Adaptive and regenerative dampers are used to improve the performance of dynamic systems by realizing optimal damping force with the added benefit of energy recovery in the system. Lack of adaptability is one of the main flaws of passive devices. The other fundamental flaw associated with passive devices is that they expel the undesired kinetic energy into heat. Using more recently developed technologies, dampers can be designed to adapt their characteristics to the conditions of the environment and system dynamically. In addition many of the adaptable damper designs have the ability to work as generators for energy recovery which improves the efficiency of the systems they are included in. For these reasons (adaptability and energy recovery), new features are gradually being added to the design of dampers for many applications such as tall buildings [8], highway bridges [9] and vehicle suspensions [10–13].

In particular, there is high level of interest in the automotive industry for such an adaptive and regenerative technology. Regarding the adaptability, in a vehicle suspension system, the damping mechanism is often provided through conventional passive hydraulic dampers which have fixed damping characteristics. Owing to possibility of various road profiles and driving conditions for a vehicle, it is vital to provide different damping characteristics. For instance, a driver prefers a softer suspension system when driving on a rough road to isolate the cabin from the road disturbances (comfort quality), and on the other hand, a stiffer suspension system is demanded when driving on a smooth road to have higher road holding quality for high speed maneuvering. Therefore, in a suspension system with fixed damping characteristics, the designer needs to choose a damping factor that works sub-optimally at a wide range of road profiles and driving conditions. Due to the variable nature of input experienced by vehicle suspension systems and the conflicting objectives of comfort and road-holding; it is apparent that having a damping mechanism with a time varying (adaptive) damping factor is a beneficial attribute. Regarding the energy regeneration, year by year, more restrictions are applied to the fuel economy standards of vehicles. According to the US standards, a light vehicle in 2012 was required to have an average fuel efficiency of 29 mile per gallon (mpg); however, by the year 2025, this standard will rise up to 54.5 mpg [14]. This has put the manufactures under pressure to implement new approaches to meet those requirements. According to the US department of energy, only $10\% - 16\%$ of the available fuel energy is used to overcome road friction and air drag [6] and the rest of the energy is wasted into heat. Many researchers have reported the high potential of available energy in the suspension systems for recovery purposes. An experimental study conducted by Zuo and Zhang [15] shows that an average power of 100, 400 and 1600 W is available for scavenging from vehicle suspension system (4 wheels) at 60 mph on ISO road classes B (good), C (average) and D (poor) respectively. By having 30% efficiency as the target for designing regenerative suspension systems, manufacturers are able to increase the fuel efficiency of the vehicles up to $\sim 0.8\%$. Implementing such technology into only 10% of Canadian light vehicles corresponds to annually saving 8.2 million liters of gasoline from burning into 43.2 Kilotons of greenhouse gas into the atmosphere.

A damper possessing the previously outlined characteristics (adaptability and energy regeneration) could increase fuel economy and further refine the driving experience. With this potential, significant scientific effort toward the design of adaptive and regenerative suspension systems has been put forth.

The first commercial implementation of an adaptable suspension system in the automotive industry was developed by Citron in the 1960s with its hydro-pneumatic suspension [16]. Since then various time varying (adaptive) damping solutions are developed by industrial and academic sectors. Delphi, Fludicon and Sachs are the three main players currently in the adaptable suspension system market, The systems developed by these companies are called the magnetorheological (MR), the electrorheological (ER) and the Solenoid Valve (SV) dampers respectively. At a slightly different level of commercialization (commercialized but with significant amount of proprietary intellectual property); Audi AG [17–19], Mercedes-Benz [20], and BMW [21] have all developed suspension systems to improve driving dynamics and passenger comfort. The core deficiency of the most of the commercially available force variable damping systems is their power consumption. Based on this fundamental shortcoming, a significant amount of work has been done to reduce the power consumption of the force variable damping systems, and further recover a portion of energy being wasted by the suspension systems. By employing linear electromagnetic motors, it is possible to develop semi-active and active damping mechanism with the capacity to recover energy [6]. The regenerative electromagnetic dampers that are developed in the academic world can be classified into two main categories: rotatory [22–32] and linear [22, 33–35]. When acting as generators, both of these categories have limited

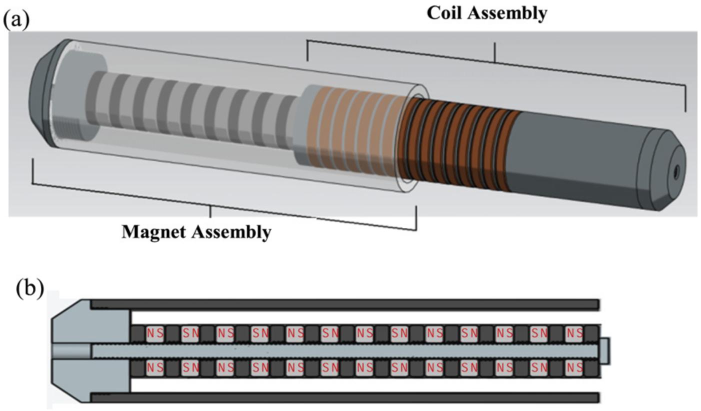

Figure 1.3: Schematic view of the linear electromagnetic shock absorber with conductor tube fixed to the magnets, a: shock assembly, and b: cross section of the magnet assembly [2].

force density; particularly at lower velocities. To overcome this performance limitation, alternative techniques have been proposed in the last two decades. For the linear topology, we can name J.F. Eastham work in which he has compared different topologies and highlighted that with respect to a general topology of machines, tubular permanent-magnet machines deliver the highest force density [36]. Lei Zuo et al. [2] have proposed a retrofitted electromagnetic damper, shown in Figure 1.3, in which the steel conductor tube is fixed together with the magnets instead of the coils. Using this technique, eddy current inside the conductor is minimized and higher rates of power are obtained. Another technique is to add slots to the coils stator to produce a higher magnitude of magnetic field inside the coils. This in turn increases the power and force densities; however fabrication of the slotted stator is more complicated, and thus more expensive. Furthermore when comparing the slottless and slotted designs, the latter has higher cogging and ripple force which is undesirable with respect to the dynamic performance [37].

Implementing multiple arrays of coils and magnets, as shown in Figure 1.4, also increases the damping force and the regenerated power [3, 4]. However it can also increase the weight and size of the damper. With that said it is a difficult task to keep the weight and size of such designs within required limits. For instance a vehicle shock absorber should fit inside a designated space in the suspension mechanism and also its mass is recommended to be less than 7 kg [10]. The most attractive aspect of these linear topologies for automotive applications is that no change in motion direction is required, making it a bit simpler to be implemented mechanically. In comparison to linear electromagnetic devices, a conversation mechanism is needed in the rotary topology to change the motion from

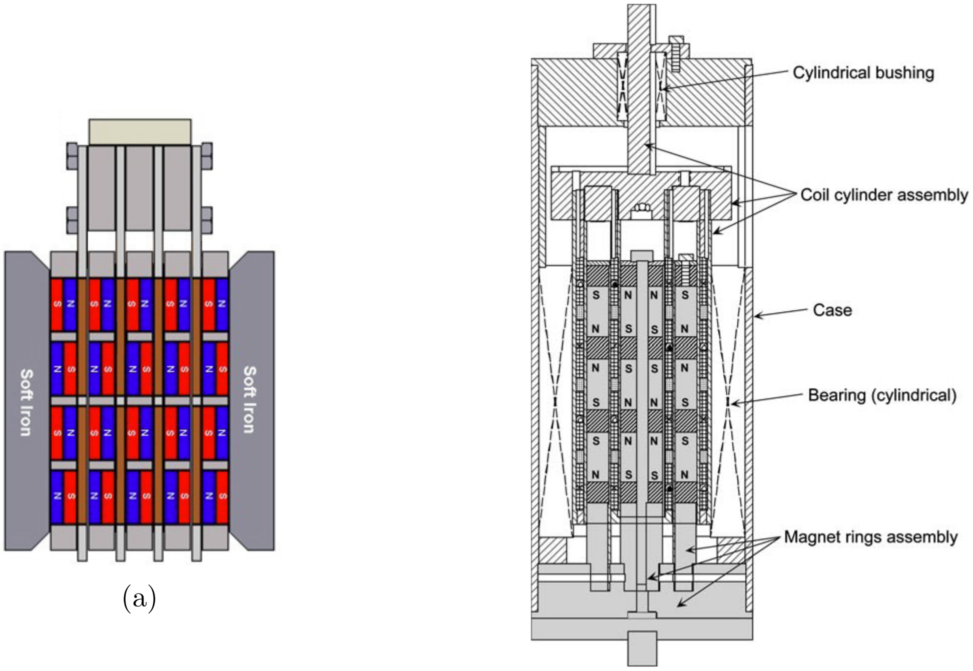

(a)

(b)

Figure 1.4: Multiple magnet/coil arrays in electromagnetic machines, a: Tang et al. rectangular design [3], and b: Gupta et al. tubular design [4].

linear to rotary. In the proposed rotary topologies, some researchers have implemented intermediate mechanisms (i.e. gears) to magnify the input velocity of the damper (shock absorber). By increasing the input velocity higher voltages are induced in the coils which corresponds to higher damping forces and regenerated power. There are, however, several drawback associated with those mechanisms that limits their implementation. Gears have a finite service life which ultimately leads to the requirement of servicing to maintain functionality. Also due to the backlash in the gears, there is a time delay in the response of these mechanisms. Zhang et.al. [38] used a ball-screw mechanism to convert the linear motion of the shock absorber to rotary and also to magnify the input. Experimentally it was shown that the mechanism loosens at high frequencies which results in adverse effects on the performance. In addition, gears introduce added mass to the system which at high speeds (or high frequencies) tends to degrade the dynamic behavior of the system due to the inertial effects [39, 40]. Montzeri et al. [41] suggested adding a spring in series with an electromagnetic damper to isolate the damper from high frequency disturbances. This solution however does not completely solve the problem.

Overall, the commercial products are attractive due to their proven performance and fail-safe operation. The major disadvantage results from the amount of power they consume. The linear and rotary electromagnetic dampers (in semi-active configuration) are attractive due to high performance characteristics and regenerative capacity. However, these systems are not fail-safe, and additionally, they tend to produces lower damping forces than commercial dampers of similar sizes.

1.3.2 Active Hybrid Electromagnetic Vibration Isolator

Active vibration isolation is the process of attenuating the transmitted vibration from one body to another by means of active elements. Active isolators are designed to address the drawbacks of traditional vibration isolators.

The performance of the vibration isolator is evaluated based on how effectively it minimizes the transmitted vibrations between two bodies, connected by the isolator. In this work, we experimentally study the effectiveness of a novel hybrid vibration isolator, in reducing acceleration (T_a) and force (T_f) transmissibilities. The acceleration transmissibility (Figure 1.5a) is the ratio of output/mass acceleration to input/oscillating body acceleration; and force transmissibility (Figure 1.5b) is defined as the ratio of the output dynamic force to the input/oscillating body acceleration.

In the past, active systems have been utilized to isolate optical systems from support structure vibrations [42], aircraft wing from external disturbances [43], vehicle cabins from

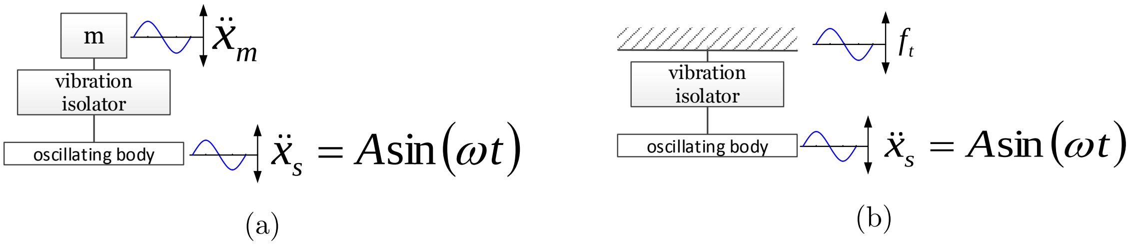

Figure 1.5: Schematic diagram of vibration isolation cases, a: case 1: acceleration $\ddot{x}_s$ is imposed at the oscillating body, and acceleration $\ddot{x}_m$ is transmitted to the mass m, and b: case 2: acceleration $\ddot{x}_s$ is imposed at the oscillating body, and force f_t is transmitted to a fixture.

tire vibrations generated by uneven road surface [44–46], vehicle cabins from engine induced vibrations [47], helicopter cabins from rotor gearbox vibrations [48], tall buildings from wind disturbances [49], and etc.

Commonly, vibration isolators consist of a passive spring and a damper. These passive elements are often inexpensive and simple to manufacture, and in addition have a long life span. They however, have limited dynamic performance [50]. In their design, there is often a trade-off between having an adequate vibration isolation and an allowable level of deflection [51]. The problem is that, while they are able to effectively isolate high frequency vibrations, they have a poor performance in low frequencies. In order to improve the vibration isolation in a resonance frequency, larger damping ratios can be chosen, but this change results in poor high frequency isolation. On the other hand, by decreasing the damping ratio, better high frequency vibration control is achieved at the cost of less resonance control [52].

A major advantage of implementing active elements in vibration isolators is to overcome the above-mentioned trade-off. Active vibration isolators exhibit improved performances especially in lower frequencies. They are also able to adjust to the changes in excitation conditions in a real time manner. Another positive aspect of active systems is their capability to dissipate energy as well as supply it [53].

Much effort has been made in designing and developing new active actuators with higher force densities and bandwidths. In the developed actuators, there are several active technologies that are mainly utilized: magnetostrictive [54–56], piezoelectric [5, 57–59], pneumatic [60–62], hydraulic [63], and electromagnetic (in form of rotary or linear motions) [64–66] actuators.

Magnetostrictive (Figure 1.6) and piezoelectric (Figure 1.7) actuators use the magne-

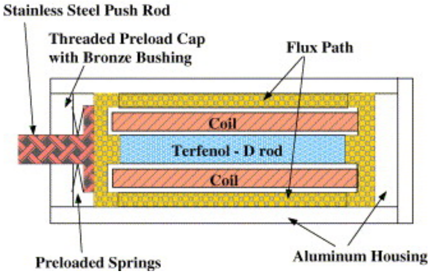

Figure 1.6: Schematic view of a magnetostrictive (Terfenol-D) actuator [5].

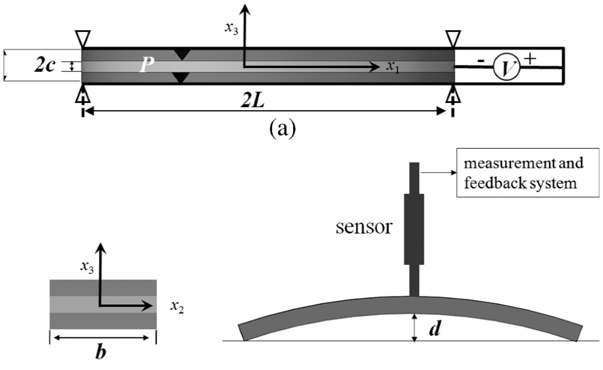

(a)

(b)

(c)

Figure 1.7: Schematic view of a piezoelectric actuator [5], a: piezoelectric actuator, b: the cross-section of actuator, and c: the dome height of actuator.

tostriction and piezoelectricity effects in which strains are generated in response to an applied magnetic and electric fields respectively [54, 67]. Magnetostrictive and piezoelectric actuators are generally compact, and can generate large forces for their size, however, their low-displacement characteristics precludes their implementations in many applications [68]. Furthermore, piezoelectric actuator are substantially more stiff comparing to the springs, and because of that, in devices with parallel arrangement of actuators and springs, the performance is reduced [52]. Hydraulic and pneumatic actuators have larger displacement strokes, however, they are associated with weight and bulky design problems, their bandwidth is limited, and their associated hydraulic/pneumatic supply unit must inconveniently be used. Electromagnetic technologies allows for the development of high bandwidth actuators with large strokes, yet, the electromagnetic actuators, similar to hydraulic/pneumatic actuators, suffer from large weights and volumes.

Voice coil is a kind of electromagnetic actuator that in particular has been used widely

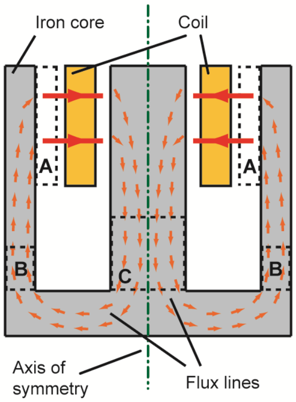

Figure 1.8: Schematic view of a cylindrical voice coil (the three possible locations for the permanent magnet are A, B and C) [1].

in both industrial and academic sectors in the past two decades [69–78]. As shown in Figure 1.8, it consists of a a magnetic housing a cylindrical coil. The voice coil actuator is originally used in amplifiers, however, owing to its positive attributes, it is frequently utilized in the applications in which rapid and controlled motions are required [79]. Using magnetic force, voice coil provides a superior acceleration and deceleration with a sufficient bandwidth required for many applications including vibration isolation [79,80] and precision motion [1].

1.3.3 Hybrid electromagnetic dampers and vibration isolators

By combining the electromagnetic machines with other technologies, different semi-active dampers and active vibration isolators are proposed in the past two decades. For instance, Foshage et al. [81] developed a hybrid damping system for spacecraft vibration isolation and suppression which consisted of a tuned passive isolator and a linear active voice coil motor. Suda et al. [82] proposed a vehicle suspension system that employs two linear electromagnetic machines in series. The primary machine works as a generator that stores the vibration energy into temporary electrical energy storage while the secondary machine uses the stored energy to actively control vibration. One of the drawbacks of such system, is the need for extra space for the secondary mechanism. Ebrahimi et al., [10] designed a hybrid active/passive damping system that utilized the eddy current effect as the main mechanism for providing a bias passive damping force and an electromagnetic linear motor as a complementary active damping mechanism. A similar system was proposed by Martin et al. [83], using a viscous system as the passive part. The most positive attribute of the Ebrahimi et al. and Martin et al. designs is the unification of two different mechanisms in a single package. This attribute simplifies the mechanism (reduced installation space requirements) and expands the application areas of the damping system. Since neither of these two designs was fabricated, no experimental data is available.

In particular in the active vibration isolation problem, Teel et.al state that it is widely accepted that in wide bandwidth vibration isolation, the hybrid design is the ideal solution [84]. Each of the components in the hybrid device are responsible for isolating a range of vibrations. At low frequencies, where the passive component suffers from undesired peaks, the desired degree of vibration isolation is achieved via an active feedback control loop (provided by the active electromagnetic actuator). At high frequencies, on other hand, the passive component guarantees the required performance.

1.4 Research Objective

Our interest in hybrid vibration isolation systems is primarily motivated by the need for active/semi-active, fail-safe, and compact vibration isolation devices for various applications. Based on this need, this PhD work proposes alternative hybrid designs in which an electromagnetic component is employed for providing active/semi-active force variation for the hybrid damping system. In a compact design, the electromagnetic component alone is not capable of producing enough control forces, and furthermore it is usually not fail-safe. Therefore it is integrated with a complementary passive component which produces a large baseline fale-safe force. Both of semi-active and active case are considered in this work. Accordingly in the first step, the concepts of a semi-active hybrid electromagnetic damper and an active hybrid electromagnetic vibration isolation system were previously introduced in this chapter. Based on both concepts, two prototype are designed, optimized and fabricated; and finally using the fabricated prototypes, the proposed hybrid solutions are experimentally validated.

1.5 Contributions

The main contribution of this thesis is the introduction and experimental validation of novel hybrid vibration isolation systems. This PhD work demonstrates the effectiveness of using hybrid systems for vibration isolation applications. Furthermore, it advances the state of the knowledge in the design and optimization techniques of electromagnetic machines including tubular and low profile linear actuators. By incorporating different analysis methods such as theoretical, numerical, finite element, and experimental ones, this PhD work comprehensively investigates the problem of hybrid vibration isolation. The outcomes of this work also contribute to many related fields and applications including eddy current effects, vehicles suspension systems, and voltage conditioning in energy regenerative systems.

1.6 Thesis Structure

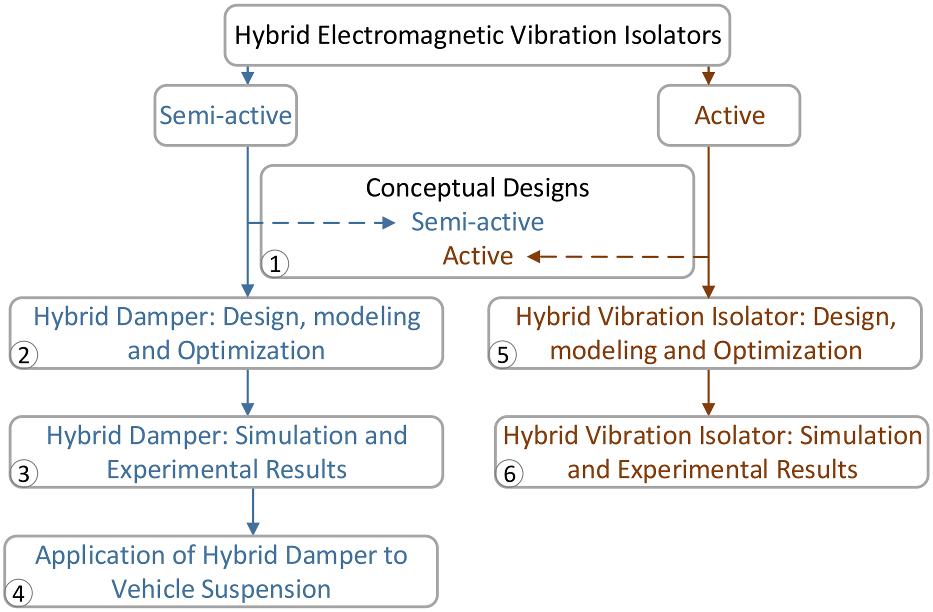

Figure 1.9: Schematic flowchart of the thesis structure (chapter numbers are given in small circles).

The structure of this thesis is as follows (also shown in Figure 1.9).

- Previously in Chapter 1 problem of force control in vibration isolation systems was stated, and for both semi-active and active cases, alternative conceptual hybrid designs were proposed to address the problem. In the proposed concepts, electromagnetic components are combined with other passive elements in hybrid single packages. Chapter 1 also reviewed the literature and previous works done in the areas of semi-active electromagnetic damping and and active electromagnetic vibration isolation. For both semi-active and active cases, the advantageous of electromagnetic devices, over other technologies were listed, and furthermore the shortcomings of electromagnetic devices, that limit their applications were reported.

- Starting with the semi-active damping case, in Chapter 2, the design, modeling and optimization of a new semi-active hybrid electromagnetic damper are presented. By choosing vehicle suspension systems as the target application, the detail design of a hybrid electromagnetic damper is presented. The hybrid damper is configured to operate with viscous and electromagnetic subsystems. The viscous medium provides a bias and fail-safe damping force while the electromagnetic component adds adaptability and the capacity for regeneration to the hybrid design. The electromagnetic component is modeled and analyzed using analytical approach (lumped equivalent magnetic circuit) and electromagnetic finite element method (FEM). By implementing both modeling approaches, an optimization for the geometric aspects of the electromagnetic subsystem is obtained. An extended optimization analysis of the electromagnetic damping component of the hybrid damper is also presented which can serve as potent tool for the designers who seek maximizing the adaptability (and regeneration capacity) of the hybrid damper. An analytical model is also presented for viscous damping force.

- In Chapter 3, experimental and simulation results of the semi-active hybrid electromagnetic damper are presented. Based on the designed (and optimized) electromagnetic hybrid damper, a prototype is fabricated. Different simulation and experiments are conducted to characterize the damping properties of hydraulic and electromagnetic components. Furthermore, friction forces as well as power capacities are scrutinized. The experimental results validate the accuracy of the models and the preliminary optimization solution.

- Chapter 4 presents the application of the semi-active hybrid electromagnetic damper to vehicle suspension systems. A primarily challenge in implementing hybrid damper in the vehicle suspension system is to add adaptability and energy regeneration benefits to the system without introducing any adverse effect to the system main functionality. For analyzing the system, the electromagnetic component is modeled and integrated into a 2 DOF quarter car model. Three criteria are considered for evaluating the performance of the suspension system: ride comfort, road holding, and regenerated power. Using the genetic algorithm multi-objective optimization (NSGA-II), the suspension design is optimized to improve the performance of the vehicle with respect to the selected criteria.

- Chapter 5 is allocated to the design and geometrical optimization, and controller design of a new active hybrid electromagnetic vibration isolation system. The hybrid vibration isolator, designed in this work, is composed of a passive pneumatic spring and an active electromagnetic actuator in a single hybrid package. The electromagnetic component is modeled and optimized using analytical and FEM approaches. In order to evaluate the performance of the optimized solution, the force density of the optimized electromagnetic component is compared with a voice coil actuator, that is widely used in both academic and industrial sectors. The pneumatic components is modeled using commonly used Nishimura method. Finally, model based and non model based controllers are developed for two cases: acceleration and force transmissibilities.

- Chapter 6 presents experimental and simulations results for the designed active hybrid electromagnetic vibration isolator. A prototype is fabricated based on the optimized solution. The accuracy of the models in predicting the device vibration forces, and also its acceleration and force transmissibilities is experimentally validated.
- Finally, conclusions and future works are presented in Chapter 7.

It should be mentioned that the work presented in Chapters 2 and 3 is conducted with the collaboration of Roberto Ribeiro, an M.A.Sc. candidate [85] within the same research group. For the hybrid damper prototype, both of the teammates have equally contributed to the development of the general topology design as well as the structural design of different parts of the damper. Detailing and CAD drawing of the designed damper is done by Roberto using SolidWorks software package. The components of the final design have been either outsourced (mostly done by Roberto Ribeiro) or been fabricated, by the two teammates, at the university machine shop. The setup preparation, experimental testing and data post processing, all conducted jointly by the teammates at the Maglev and Mechatronic Vehicle Systems labs.

Chapter 2

Semi-active Hybrid Electromagnetic Damper: Design, Modelling, and Optimization

2.1 Damper Design

The semi-active hybrid damper design proposed in this study integrates a viscous medium and an electromagnetic semi-active generator into a single unit. The viscous dampers are the most widely used damping mechanisms in industry. Their reliability, capacity to handle large force and high speed, and their predictability made them a good candidate for producing a baseline damping force. The electromagnetic component is employed for adding energy recovery and adaptability features to the hybrid damping system.

2.1.1 General Design Requirements

The first step towards designing the device is to determine the general specifications based on the desired application. For the design of hybrid electromagnetic damper, a vehicle suspension is selected as the target application; however this design plan can be implemented for other applications as well. The main requirements for the selected application (i.e. vehicles suspension) are the required damping force and geometric considerations. Depending on the vehicle, the damping coefficient of suspension systems can vary from 1200 to 2000 Nsm^{-1}. Here, a total damping coefficient of 1500 Nsm^{-1} is targeted. The

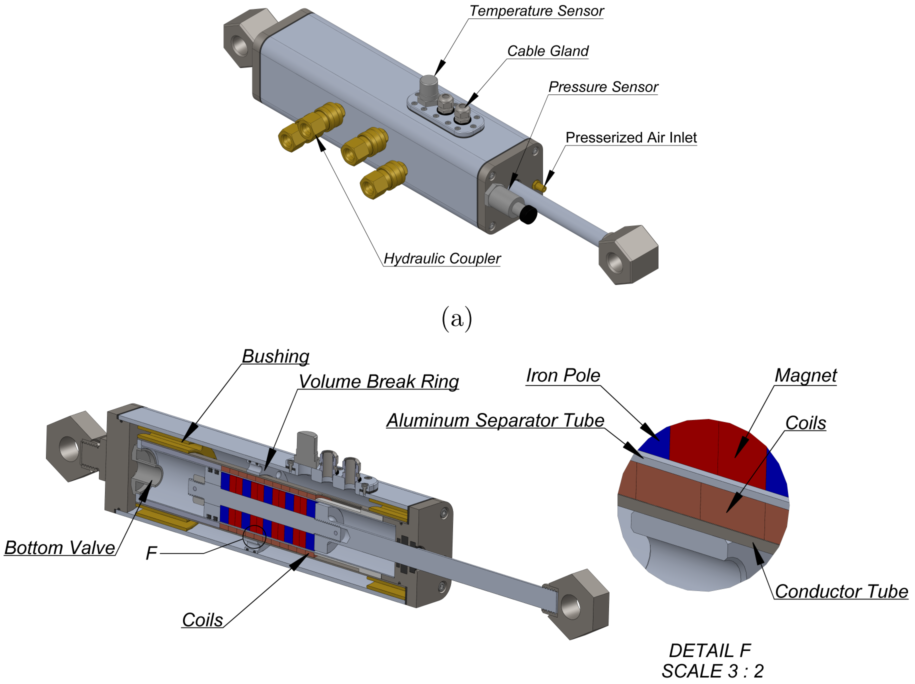

(a)

(b)

Figure 2.1: Hybrid damper twin tube design (with a width and height of $H = W = 76.2\ mm\ (3.0\ in)$, and a length (fully retracted) of $L = 468.630\ mm\ (18.450\ in)$), a: isometric view, and b: cross sectioned view.

initial goal is set to generate an approximately 200-300 Nsm^{-1} damping force via the electromagnetic component. The rest of the demanded damping force is provided through the viscous medium. The damper is required to have a stroke of 76.2 mm (3 in) and its fully extended length should be less than 508 mm (20 in). Furthermore, the outer diameter of the damper should not be greater than 76.2 mm (3 in) so it can fit inside the allocated space in the suspension system.

The proposed hybrid damper design is depicted in Figure 2.1. This design is made up of a conventional twin-tube viscous damper and an electromagnetic generator; located in the inner tube.

To maximize the force density of the electromagnetic component, a tubular topology is selected where the iron-magnet arrays are mounted on the central moving piston and the coils are set stationary in the stator. The space between the coils and the piston is filled with oil, which could result the impurities and floating particles in the oil wearing out coil coating (potentially causing a short). Also due to the small clearance, the piston can touch the coils and deform them. To avoid these problems, a thin (aluminum) separator tube is putted in between to protect the inside of the coils. The outside of the coils is protected by the conductor tube which is made of steel. The conductor tube is also responsible for separating the inner and outer sections of the twin-tube damper design. A maximum outer diameter of 50.8 mm (2 in) is selected as the design restriction for the conductor tube so that enough space is available for the oil to flow in the outer section. The clearance between the piston and inner tube wall and the orifice size of bottom valve, both are fixed and therefore it is not possible to set the damping coefficient of the viscous component. As a result, an additional tool is required to add adjustability to a passive system. To achieve this goal the outer section is firstly divided into two separate chambers by installing a block ring (labeled as *volume break ring* in Figure 2.1) in the middle of the outer section. Secondly, those volumes are connected thorough external adjustable valves (through the hydraulic couplers).

With respect to the material selection, except for the brass bushings, copper coils, magnets, and iron conductor tubes and iron poles, the remaining parts are made of aluminum to minimize the weight of the damper. Aluminum also helps to minimize the magnetic flux leakage (into the piston central rod). The hydraulic component is filled with the same oil that is used in vehicle shock absorbs. These oils, have a long life span and do not suffer from the degradation problems that exist in MR and ER dampers.

2.2 Modeling of the Electromagnetic Component

Comparing to simple structure of hydraulic dampers, the electromagnetic machines are relatively complex systems, and a poor design would significantly hinder their performances. Therefore, in this section, a linear electromagnetic machine is modeled and analyzed to obtain a better understanding of the system functionality. First, the machine is modeled as a semi-active damper using lumped equivalent magnetic circuit (LEMC) method. Afterward, this model in conjunction with FEM simulations is used to probe the effect of some important factors on the performance of the electromagnetic damper. These analyses, help the designers to employ a better optimization strategy for maximizing the damping force (and the regenerative capacity).

Figure 2.2 schematically represents the three-phase tubular electromagnetic comonent with the adopted nomenclature. In this machine coils are assumed to be stationary mounted to the iron conductor while magnets (and iron poles) are mounted on the moving shaft. The magnets are magnetized axially (shown with red arrow). The black arrows represent the flux circuit inside the machine. The electromagnetic component is a 3 phase linear motor. Each phase has 5 coils that are named R1-R5, G1-G5 and B1-B5 in phases R, G and B respectively. This gives the damper 15 coils in total. The performance of the linear electromagnetic component of the system in terms of regenerative capacity and damping force is highly dependent on its geometry. Therefore, an optimization of the geometry is required to enhance the performance of the system. The two most commonly used models for optimization purposes are LEMC [8, 86] and FEM [2, 87, 88]. The LEMC approach is straight forward and less computationally expensive. This method aims to simplify the spatially distributed electromagnetic system by replacing it with a series of interconnected simple discrete elements. Due to its simplicity, this method had become the most common approach in establishing a relation between design parameters and machine performance. In terms of optimization however, the LEMC does not have enough accuracy and leads to different optimization results from author to author. FEM can be considered as the most accurate approach for modeling the electromagnetic damper. However, FEM methods are complex to implement and have significant computational costs.

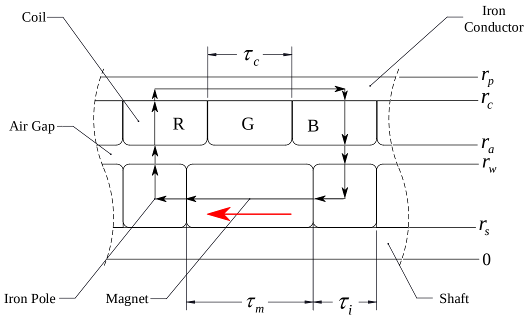

Figure 2.2: A schematic view of a three-phase tubular electromagnetic machine. Coil phases are named R, G, and B (the adopted names are derived based on RGB color system).

2.2.1 Electromagnetic Modeling Using Lumped Equivalent Magnetic Circuit Model (LEMC Model)

The electromagnetic component of the hybrid design is based on the Faraday-Lenz and Lorentz laws. Faraday's law of induction states: the change of total flux in a closed circuit results in an induced electromotive force proportional to the rate of change of flux through the integral path. According to Lenz's Law, the induced magnetic field produced by the induced current will oppose the direction of the original magnetic field. The Faraday-Lenz law can be mathematically represented by the following expression:

$$V_{emf} = -\frac{d\lambda}{dt} = -\frac{d\phi}{dt} \tag{2.1}$$

where V_{emf} represents the electromotive force in volts, λ is the magnetic flux linkage, N represents the number of turns in a conductor coil and ϕ represents the flux through each turn of coil.

Lorentz' law quantifies the electromagnetic force F_E experienced by the conductor coil and is obtained by:

$$F_E = \oint i d\boldsymbol{l} \times \boldsymbol{B} \tag{2.2}$$

where i and $\boldsymbol{l}$ are magnitude and path of the induced current, $\boldsymbol{B}$ is the magnetic field flux density, and × denotes the cross product.

In order to formulate the electromagnetic damper, the distribution of magnetic field needs to be obtained with respect to the given design parameters. This can be achieved by using any of the following three main techniques: 1-lumped equivalent magnetic circuit ([86,89]), 2-numerical solution (finite element method) ([2,87]) and 3-analytical solution (separation of variables) ([2,90]).

When compared to the other two mentioned methods, the lumped equivalent magnetic circuit is straightforward and less computationally expensive. This has led to the lumped equivalent magnetic circuit method becoming the most common approach in establishing a relationship between design parameters and machine performance. This method aims to replace the spatially distributed electromagnetic system with a series of interconnected simple discrete elements.

In Figure 2.2 a lumped magnetic circuit model of the electromagnetic damper is shown. The analysis is conducted for a magnet-iron pair but the same concept holds for all the pairs. By neglecting the magnetic flux leakage in the center rod, Ampere's law is applied to the contour C as follows:

$$\oint_C H dl = \oint_{magnet} H dl + \oint_{iron} H dl + \oint_{air} H dl + \oint_{copper} H dl = 0 \tag{2.3}$$

$$\oint_C Hdl = H_m\tau_m + 2\int_{r_s}^{r_w} \frac{B_{pole}}{\mu_0\mu_{Fe}}dr + \frac{B_{p\ tube}}{\mu_0\mu_{Fe}}(\tau_m + \tau_i) + 2\int_{r_w}^{r_a} \frac{B_{air}}{\mu_0}dr + 2\int_{r_a}^{r_c} \frac{B_{coil}}{\mu_0\mu_{co}}dr = 0 \tag{2.4}$$

where H is the magnetic field strength, μ_0 is the permeability of free space and μ_{Fe} and μ_{co} are the relative permeability of iron and copper, respectively.

In order to solve equation 2.4 and find the operation point of the machine, H_m, B_{pole}, $B_{p\ tube}$, B_{air}, and B_{coil} are written in terms of B_m. The permanent magnetic characteristic equation defines the relation between H_m and B_m as:

$$H_m = \frac{B_m - B_{rem}}{\mu_{rec}} \tag{2.5}$$

where B_{rec} and μ_{rec} are the remnant flux density and recoil permeability of the permanent magnets, respectively. These parameters are obtained from the demagnetization curve of the permanent magnets. Since the magnetic flux leakage is neglected, the continuity condition can be applied to determine the magnetic flux densities for the various volumes in terms of B_m:

$$A_m B_m = A_{pole}B_{pole} = A_{ptube}B_{ptube} = A_{air}B_{air} = A_{coil}B_{coil} \tag{2.6}$$

where A_i represent the area of part i. Solving equation 2.6 for magnetic flux densities yields:

$$\begin{aligned}
B_{pole} &= \frac{\pi(r^2 - {r_s}^2)B_m}{2r\pi\left(\frac{\tau_i}{2}\right)} \\
B_{p\ tube} &= \frac{\pi({r_w}^2 - {r_s}^2)B_m}{\pi\left({r_p}^2 - {r_c}^2\right)} \\
B_{air} &= \frac{\pi({r_w}^2 - {r_s}^2)B_m}{2r\pi\left(\frac{\tau_i}{2}\right)} \\
B_{coil} &= \frac{\pi({r_w}^2 - {r_s}^2)B_m}{2r\pi\left(\frac{\tau_i}{2}\right)}
\end{aligned} \tag{2.7}$$

Using equation 2.7, the elements of equation 2.4 can be obtained as follows:

$$\int_{r_s}^{r_w} \frac{B_{pole}}{\mu_0\mu_{Fe}}dr = \frac{1}{\mu_0\mu_{Fe}\tau_i}\left[\frac{{r_w}^2 - {r_s}^2}{2} - {r_s}^2 \ln\left(\frac{r_w}{r_s}\right)\right] B_m = k_{pole}B_m \tag{2.8}$$

$$\frac{B_{p\ tube}}{\mu_0\mu_{Fe}}(\tau_m+\tau_i)=\frac{({r_w}^2-{r_s}^2)(\tau_m+\tau_i)}{({r_p}^2-{r_c}^2)\mu_0\mu_{Fe}}B_m=k_{p\ tube}B_m \tag{2.9}$$

$$\int_{r_w}^{r_a}\frac{B_{air}}{\mu_0}dr=\frac{{r_w}^2-{r_s}^2}{\mu_0\tau_i}\ln\left(\frac{r_a}{r_w}\right)B_m=k_{air}B_m \tag{2.10}$$

$$\int_{r_a}^{r_c}\frac{B_{coil}}{\mu_0\mu_{co}}dr=\frac{{r_w}^2-{r_s}^2}{\mu_0\mu_{co}\tau_i}\ln\left(\frac{r_c}{r_a}\right)B_m=k_{coil}B_m \tag{2.11}$$

By substitution of equations 2.8-2.11 and 2.5 into equation 2.4, the operation point of the electromagnetic damper is obtained as:

$$B_m=\frac{B_{rem}\tau_m}{\tau_m+\mu_{rec}\left(2k_{pole}+k_{p\ tube}+2k_{air}+2k_{coil}\right)} \tag{2.12}$$

By substituting equation 2.12 into equation 2.7, the magnetic flux density at the different parts of electromagnetic damper can be evaluated. In the following sections, the obtained magnetic flux density in the coils is used to calculate the induced voltage across the coils.

Coil Induced Current

The relative velocity of armature (magnet-pole arrays) relative to the stator coils induces voltage across the coils. Applying the FaradayLenz's law for a single coil turn gives us:

$$V_{emf_{single\ turn}}=-2\pi rB_{coil}\frac{dx}{dt}=-\frac{2\pi({r_w}^2-{r_s}^2)B_m}{\tau_i}\frac{dx}{dt} \tag{2.13}$$

Therefore the total electromagnetic induction across the coil is:

$$V_{emf}=-N\frac{2\pi({r_w}^2-{r_s}^2)B_m}{\tau_i}\frac{dx}{dt}=-k_v\frac{dx}{dt} \tag{2.14}$$

where N is the number of excited turns in the coil and $k_v=N\frac{2\pi({r_w}^2-{r_s}^2)B_m}{\tau_i}$ is called the voltage constant of the coil.

The relationship between the induced current (i) and the electromagnetic voltage (V_{emf}) in the coils is dependent on the how the coils are connected (star, delta, etc) to the external circuit. For the case where each coil is connected to an external load R_{ext} (coined as "standard configuration" for this PhD work), the induced current (i) and regenerated power (P_E) can be obtained from:

$$L_{coil}\frac{di}{dt} + (R_{coil} + R_{ext})\, i = V_{emf} = -k_v\frac{dx}{dt} \tag{2.15}$$

$$P_E = R_{ext}i^2 \tag{2.16}$$

where L_{coil} and R_{coil} are the coil's inductance and resistance, respectively, and R_{ext} and x are the external load and the damper displacement, respectively.

Electromagnetic Force

For a single coil turn, the experienced electromagnetic force is obtained using Lorentz's law as follows:

$$F_{E_{single\ turn}} = 2\pi r B_{coil} i = \frac{2\pi({r_w}^2 - {r_s}^2)B_m}{\tau_i} i \tag{2.17}$$

Therefore the total electromagnetic damping force is:

$$F_E = N\frac{2\pi({r_w}^2 - {r_s}^2)B_m}{\tau_i} i = k_f i \tag{2.18}$$

where $k_f = N\frac{2\pi({r_w}^2 - {r_s}^2)B_m}{\tau_i}$ is called the force constant of the coil and has the same value as k_v. By multiplying equation 2.15 by k_f, the force-velocity relationship of the electromagnetic damper is obtained as:

$$L_{coil}\frac{dF_E}{dt} + (R_{coil} + R_{ext})\, F_E = -{k_v}^2\frac{dx}{dt}, \tag{2.19}$$

For a sinusoidal armature displacement profile in the form of $x = A\sin(\omega t)$, the electromagnetic damping force is given by:

$$F_E = Ce^{-\frac{R_{coil}+R_{load}}{L_{coil}}t} + \frac{{k_v}^2}{\sqrt{(R_{coil} + R_{load})^2 + (\omega L_{coil})^2}} A\omega\cos(\omega t + \theta) \tag{2.20}$$

where A and ω are the amplitude and angular frequency of the excitation and C is a constant determined based on the initial condition. As can be observed in equation 2.20, there is a phase shift between input displacement and output force and its value is given by:

$$\theta = \tan^{-1}\left(-\frac{\omega L_{coil}}{R_{coil} + R_{load}}\right) \tag{2.21}$$

It should be noted that the electromagnetic force (F_E), in the equations 2.19 and 2.20, is derived only for one pair of iron-magnet, and its magnitude should be multiplied by the number of iron-magnet pairs used in the electromagnetic component. As it is seen in equations 2.19 and 2.20, if a variable external load is applied between the two ends of the coil a variable amount of damping force could be achieved. Based on this feature, custom electronics can be designed to tune the external load (R_{ext}) in a real time manner, and thus adapt the dynamic behavior of the hybrid damper to satisfy the time varying damping requirements of the vehicle.

2.2.2 Electromagnetic Modeling Using Finite Element Method (FEM)

The electromagnetic component is also modeled using FEM. For this task, COMSOL Multiphysics software package (version: 4.3b) is used. COMSOL is a finite element based solver that enables the coupling of multiple physics domains into a single model. The modeling included three main steps as follows: 1- Modeling the electromagnetic structure as a stationary system (Magnetic Field or mf physics), 2- Modeling the harmonic motion of the armature (Moving Mesh or ale physics) and 3- Modeling the electrical circuit shunted with the coils (Electrical Circuit or cir physics). Figure 2.3 reflects the evaluated magnetic field density of the system at different locations. The magnitudes of the magnetic flux density are represented by the shown color map (intensity increases from dark blue to dark red, minimum to maximum).

As it can be observed, all the sharp edges in the COMSOL model are rounded. This is mainly because sharp edges create singularities when using the Maxwell stress tensor for force calculations and thus should be avoided if possible. Furthermore to avoid magnetic oversaturation, the nonlinear B-H curve in Figure 2.4 has been implemented as the constitutive relation for describing the magnetic behavior of all steel parts (armature poles and conductor tube). In order to ensure that the results of the FEM model are accurate, a few steps are taken. Mesh densities are refined until no further changes in the results are

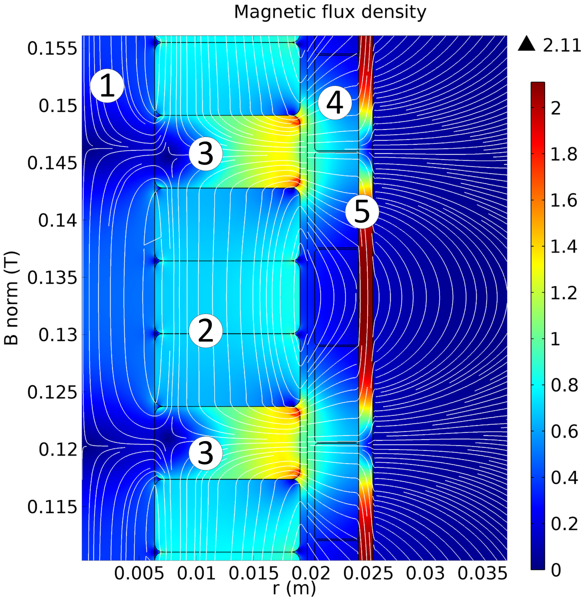

Figure 2.3: Magnetic flux density at different locations, 1: armature central rod, 2: iron poles, 3: magnets, 4: coils, and 5: conductor tube.

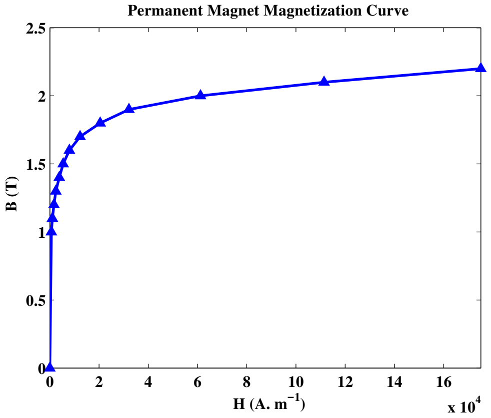

Figure 2.4: $B - H$ curve implemented in the FEM model for describing the magnetic behavior of steel parts.

observed. Furthermore, the electromagnetic forces of armature and stator are separately calculated and compared. These two forces are required to be exactly opposite of each other at every moment. Finally, experimental results are obtained and compared with the

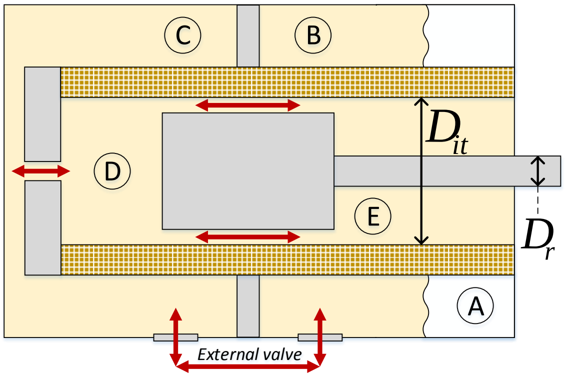

Figure 2.5: Schematic view of the twin tube viscous damper, red lines show the connections between different sections of the damper. section includes A: pressurized air, B: upper part of outer tube, C: lower part of outer tube, D: compression chamber, and E: extension chamber.

FEM results (will be presented in future sections). Table 2.1 presents the details of the COMSOL FEM model of the semi-active electromagnetic component

Table 2.1: Details of COMSOL FEM model of the Semi-active electromagnetic component.

Mesh Type	Mesh Maximum Size	Time Step	Boundary Condition	Termination Relative Tolerance
triangular	boundary: 8 [mm], iron, magnet and coil: 8 [mm], other: 10 [mm]	1e-4 [s]	magnetic insulation	1e-4

2.3 Modeling of the Hydraulic Component

Figure 2.5 presents a schematic view of the twin tube viscous damper. Compression chamber (section D), extension chamber (section E) and lower part of outer tube (section C) are fully filled with damper oil, while the upper part of the outer tube is partially filled with oil (section B) and partially with pressurized inert gas (section A). In this figure the red arrows show the direction oil flows between different sections of damper.

The damping force produced by viscous component (F_v) is given by:

$$F_v = \frac{\pi}{4}\left(P_D {D_p}^2 - P_E({D_p}^2 - {D_r}^2)\right) \tag{2.22}$$

in which P_i is pressure in section i, and D_p and D_r are diameters of piston and central rod respectively. Oil pressure at sections A-E are evaluated using the following equations:

$$\dot{P}_E \frac{V_E}{K} = -\dot{V}_E + Q_{DE} \tag{2.23}$$

$$\dot{P}_D \frac{V_D}{K} = -\dot{V}_D - Q_{DE} + Q_{CD} \tag{2.24}$$

$$\dot{P}_C \frac{V_C}{K} = -Q_{CD} + Q_{BC} \tag{2.25}$$

$$\dot{P}_B \frac{V_B}{K} = -\dot{V}_B - Q_{BC} \tag{2.26}$$

$$P_A = P_B \tag{2.27}$$

In these equations V_i is the volume of section i, Q_{ij} is the volume flow rate from section i to j, and K is oil Bulk modulus.

Volumes of sections V_A, V_B, V_D and V_E are further determined by:

$$\dot{V}_A = -\frac{\dot{P}_A V_A}{P_A} \tag{2.28}$$

$$\dot{V}_B = -\dot{V}_A \tag{2.29}$$

$$\dot{V}_D = \frac{\pi}{4} {D_{it}}^2 \dot{x} \tag{2.30}$$

$$\dot{V}_E = \frac{\pi}{4} ({D_{it}}^2 - {D_r}^2) \dot{x} \tag{2.31}$$

where D_{it} is the diameter of inner tube and $\dot{x}$ is the velocity of the damper. Finally, the following relationship are used to describe the values of volume flow rates (Q_{ij}):

$$Q_{ij} = C_{ij} A_{ij} \; sign(P_i - P_j) \sqrt{\frac{2|P_i - P_j|}{\rho_{ij}}} \tag{2.32}$$

where C_{ij} and A_{ij} are coefficient of discharge and cross-sectional area size of the flow canal between sections i and j. ρ_{ij} represent the oil density and its value is given by [91]:

$$\rho_{ij} = \begin{cases} \rho_i & \rho_i \geq \rho_j \\ \rho_j & \rho_i < \rho_j \end{cases} \tag{2.33}$$

$$\rho_i = \rho_0 \; exp\left(\frac{P_i - P_{at}}{K}\right) \tag{2.34}$$

where ρ_0 is the oil density at atmosphere pressure (P_{at}).

The orifice size of the bottom valve, located between sections C and D, is not constant, and its area varies based on the pressure difference of sections C and D. To include this variation into the modeling, Ferdek and Luczko [92] used arctan function to approximate the valve orifice area (A_{CD}) at different pressures. At an absolute pressure difference of $\triangle P$, A_{CD} is approximated as:

$$A_{CD} = \begin{cases} A_{CDmax}\left[\frac{2}{\pi}\tan^{-1}(\triangle P - P_k)\right] & \triangle P \geq P_k \\ 0 & \triangle P < P_k \end{cases} \tag{2.35}$$

where A_{CDmax} is the orifice area when valve is fully open, and P_k is the minimum pressure required to open the valve.

2.4 Optimization of the Electromagnetic Component

Electromagnetic machines are relatively complex systems, making their optimization a challenging and time consuming task, particularly if accurate FEM models are used. The other challenge is that the geometric results yielded through a global optimization process cannot be directly applied to the design. This is due to the hybrid system external geometric restrictions, manufacturing limitations and availability of components such as permanent magnets. Therefore, the scope of optimization is narrowed to a limited number of design parameters in this study. The optimal geometric parameters for the electromagnetic damper are obtained through the following steps:

Step 1: Predetermined parameters:

The modeling nomenclature of the linear electromagnetic damper for optimization purposes were previously depicted in Figure 2.2. The dimension of the conductor tube (r_p) is not considered a design variable in the preliminary optimization process. Instead, these dimensions are manually selected to comply with the viscous design (the hybrid damper design is discussed in section 2.1). The outer and inner diameters of the conductor tube are set to $2r_p = 50.8mm$ ($2\ in$) and $2r_c = 48.54mm$ ($1.91\ in$). The armature central rod ($2r_s$) has 12.7 mm (0.5 in) diameter. The magnets are made of rare earth materials (NdFeB) and have a grade of N42 with outer diameter of $2r_w = 38.1mm$ ($1.5\ in$). This value is chosen based on the availability of the magnets on the market. This selection gives us a ratio of $\frac{r_w}{r_c} = 0.7888$ for the outer magnet radius to inner conductor tube radius, which is close to 0.8, suggested by [93]. The thickness of each coil (τ_w) is accordingly determined using:

$$\tau_w = \frac{\tau_m + \tau_i}{number\ of\ phases} \tag{2.36}$$

where the number of phases in the design is selected to be three (named: R, G and B phases).

The remaining parameters for optimization are: the size of coil wires (A_{wire}) or American Wire Gauge (AWG)), the ratio of the magnet thickness to the iron pole thickness ($\frac{\tau_m}{\tau_i}$), and the length of each stack of magnets and iron poles ($\tau = \tau_m + \tau_i$).

Step 2: Initial Optimization Using the LEMC Method: In this section the LEMC method is used to find an initial optimization solution.

Using the LEMC model, Figure 2.6 is produced; where the normalized magnetic field in the coil ($\frac{\phi_{coil}}{\tau}$) is evaluated for different combinations of $\frac{\tau_m}{\tau_i}$ and τ.

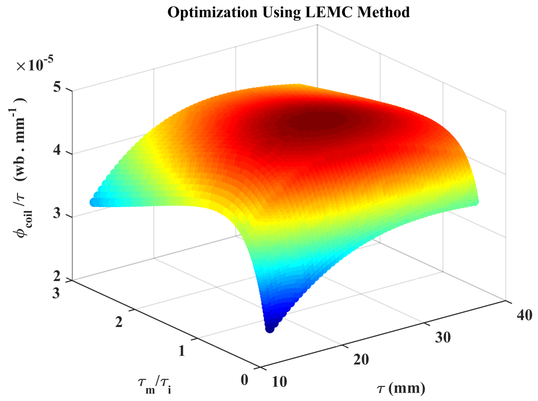

Figure 2.6: Optimization results using LEMC method.

According to this figure, the values of 1 and 24.7 (mm) are the optimal values for $\frac{\tau_m}{\tau_i}$ and τ respectively. We have previously obtained similar results for a smaller scale of proposed electromagnetic damper (presented in reference [94]). References [10,95] has also used the LEMC method and reported 1 as the optimal value for $\frac{\tau_m}{\tau_i}$ ratio for the armature arrangement.

Step 3: Final Optimization Using the FEM Method:

To finalize the geometric optimization, the values for $\frac{\tau_m}{\tau_i}$ and τ were evaluated on the basis of producing maximum damping force. Different combinations of these parameters are evaluated using FEM simulations to obtain damping force. For the simulations, each coil is short circuited which maximizes the damping force (and minimizes the regenerated energy). Also the armature is excited by an amplitude (A), and the frequency (f) of 12.7 mm, and 15 Hz respectively. According to the simulation results, it is found that changing AWG does not affect the generated forces and power. Consequently, the wire size (AWG) is set to 28. Figure 2.7 reflects the FEM results obtained through optimization for $\frac{\tau_m}{\tau_i}$ and τ parameters.

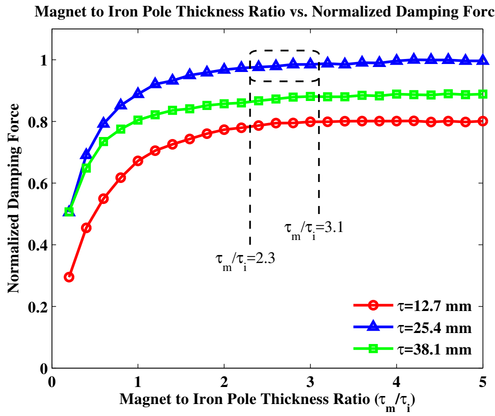

Figure 2.7: Optimization results using FEM method.

Based on the work done by Wang et al. [93], the ratio of the magnet thickness to the thickness of the iron pole is one of the main parameters of interest for optimization of an actuator. It can be seen in Figure 2.7 that by increasing this ratio, the damping force increases, however from approximately a ratio of 2.3, all the curves level off, indicating that that the minimum required ratio is 2.3. This result is consistent with the results published by Wang et al. [93] after converting the ratio shown above into an equivalent ratio for comparison. Wang et al. [93] also showed that, although the normalized damping force is maximized at these ratios ($\frac{\tau_m}{\tau_i} > 2.3$), an equivalent ratio between 2.3 and 3.1 will reduce the effects of force ripple on the actuator. Based on these results, values of 3 and 25.4 mm are chosen for $\frac{\tau_m}{\tau_i}$ and τ respectively.

The FEM and LEMC methods predicts similar values (25.4 and 24.7 mm respectively) for τ, however there is a difference in the suggested values for $\frac{\tau_m}{\tau_i}$. While FEM method suggests a thickness ratio between 2.3 and 3.1, the lumped model estimates the thickness ratio as 1 which gives approximately 10% difference in the damping force values calculated from FEM. The LEMC method, in addition to providing useful insight into the system functionality, can be used as starting point for the FEM optimization process.

Using the obtained parameters, an electromagnetic machine is configured with 4 iron poles and 3 magnets in the armature and 15 coils in the stator. In the following section, the results obtained from the FEM simulations of this machine are presented.

2.4.1 FEM Simulation Results for the Optimized Design

For a given input excitation, the V_{emf} curves of the coils are constant, however the produced damping force and regenerated power of the electromagnetic component depends on the coils connections and electrical circuit. By implementing cir physics (Electrical Circuit) in the COMSOL FEM model, the system behavior under different circuit configurations is studied. To quantify the effects of the external circuit on the damper output, an external load is connected to each of the 15 coils (coined as standard circuit configuration for this work). By changing the magnitude of the external loads, a multitude of simulations are carried out. Figure 2.8 shows the results of these simulations for damping force and power.

Figure 2.9 presents a summary of the results obtained for both metrics of interest. As seen in these figures, the highest rates of damping force ($F_{max} = 284.5\ N$) and regenerated power ($P_{rms} = 48.5\ W$) are obtained when the external loads are zero (short circuited) and when they are matched with the internal resistances of the coils ($R_c = 7.97\ \Omega$), respectively. These results show that a proper controller can regulate the damping coefficient of the electromagnetic component to any level between 0 to 238 Nsm^{-1}.

2.4.2 Additional Important Considerations in Optimization of Electromagnetic Machines

An electromagnetic damper is a relatively complex system that its performance, with respect to regenerative capacity and damping force, is highly dependent on the geometry of

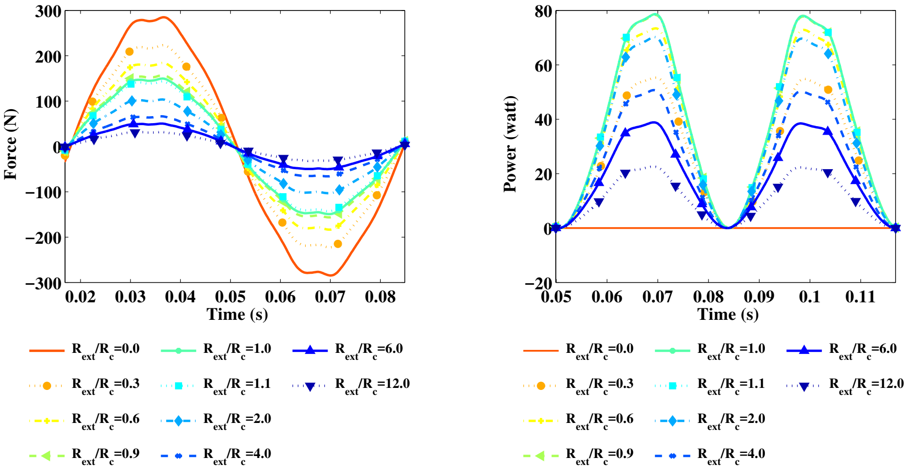

(a) (b)

Figure 2.8: Effect of external load (in ”standard configuration”) on a: damping force, and b: regenerated power.

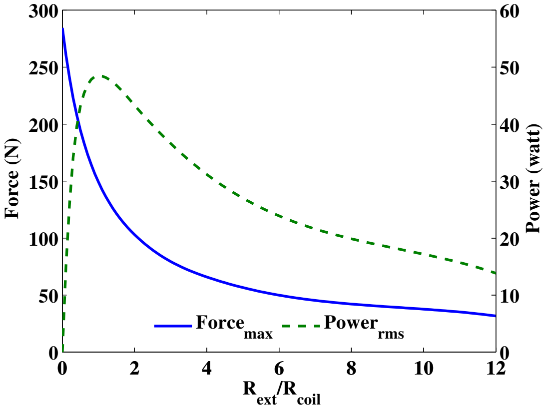

Figure 2.9: Damping force and regenerative power vs. resistance (”standard configuration”).

the system. Many studies have been carried out by researchers to optimize the geometry of electromagnetic machines, however, an inconsistency is observed between the proposed optimal design parameters. This inconsistency is owing to the implementation of different modeling approaches (with different levels of accuracy), and the diversity of step-by-step optimization strategies (each with a different set of assumptions). Previous sections utilized the lumped equivalent magnetic circuit (LEMC) model and finite element methods (FEM) to optimize the geometry of the electromagnetic component [50]. However, in that preliminary optimization, only a limited number of design parameters were considered. In this section, effects of some parameters on the performance of the electromagnetic damper are investigated which, despite their effect on the system performance, in many studies are either neglected or not considered [96]. Once the effects of these parameters are thoroughly understood, the obtained knowledge can be used toward presenting an extended optimization strategy in future works. These parameters are discussed in the following sections.

Material Properties (and Thickness) of Conductor Tube

The steel conductor tube is one of the main parts of the electromagnetic motors as it closes the magnetic flux circuit, and prevents the flux leakage into air. Similar to armature iron pole pieces, conductor tube is made of high permeable materials (e.g. stainless steel) to increase the flux density in the coil medium. The dimensions of the conductor tube were not considered as variable parameters in the preliminary optimization process, and instead, were manually selected to make the part fit inside the damper main body. It is found that the magnitudes of the magnetic flux densities inside the conductor steel reached the magnetic saturation point. The saturation occurs because, in the FEM model, the steel B-H curve is implemented as the constitutive relation for describing the magnetic behavior of the material. Based on this curve, once the magnetization reaches a certain value (2.1-2.2 T), it levels off. It is possible that magnitudes of the magnetic flux at different locations including coil medium are limited by this saturation phenomenon, meaning that the performance of the damper can be potentially improved if the conductor has a higher saturation point or its thickness increases. To examine this possibility, Figure 2.10 is provided which presents the damping force of the damper at displacement amplitude and frequencies of 7.203 mm and 5 Hz, respectively. Comparing with the original model (blue color), in the case study 1 (shown by red), the magnetic properties of the steel in the model are altered to eliminate the saturation limit. This is done by replacing the B-H curve of the constitutive relation with a simple relative permeability with no saturation limit. Due to this change, the magnetic flux density at all locations increases which results in 28.7% improvement in the damping force. This value, however, is not realistic as the B values in the conductor tube exceed 4 T. Another option for avoiding saturation is to increase the thickness of the conductor tube. The thickness of the tube in the built prototype is 0.0485 inches. By increasing this thickness by 50% in case study 2 (green curve) and 100% in case study 3 (black curve), the maximum force improves 19.5% and 30% respectively.

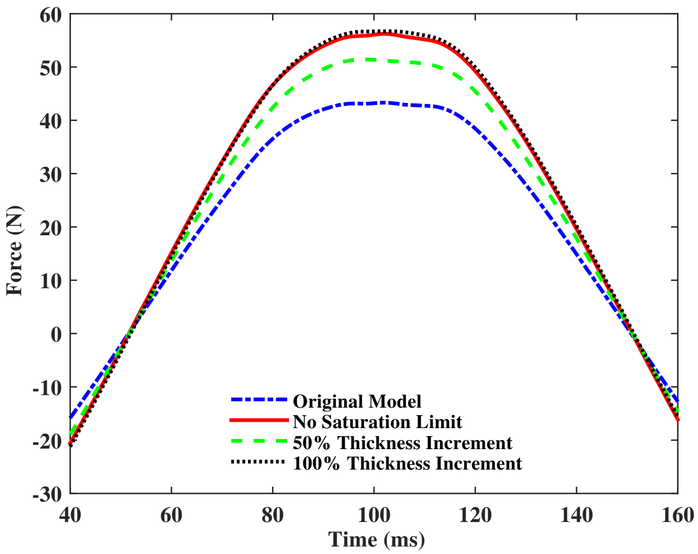

Figure 2.10: The effect of dimension and material of conductor tube on the electromagnetic damper performance.

These results highlight the effects of conductor tube dimensions and properties on the damper performance. By increasing the thickness of the tube even further, higher force values would be acquired, but the weight and cost of the product would also increase and, thus, it should be possible to derive an optimum thickness for the conductor tube. With respect to the material, it is essential to include the B-H curve in the steel modeling to avoid unrealistic results. This point, however, is ignored in many optimization strategies.

Coil Inductance Effects at Different Excitation Frequencies and Design Scales

The inductance of the stator coils is an important factor in determining the performance of the electromagnetic device. The effects of the inductance on the damping force and power are neglected for some electromagnetic machines; however, it can be shown that if the scale of the designed machine or the excitation frequency increases, those effects become more and more considerable. Consequently, ignoring those effects, results in inaccurate force and power predictions. In the rest of this section, the effects of the inductance on the damper performance is studied at different design scales and excitation frequencies.

For the simplest case assuming that $\frac{dx}{dt} = V_0$, the corresponding damping force (F_{EV_0}), based on equation 2.19, is calculated as:

$$F_{EV_0} = C_1 e^{-\frac{R_{coil}+R_{ext}}{L_{coil}}t} + \frac{-{k_v}^2}{R_{coil}+R_{ext}} V_0, \tag{2.37}$$

where C_1 is obtained based on the initial condition. By neglecting the transient response and only considering the second term of the above equation, it can be seen that the ratio of force over velocity ($r_{fv} = \frac{F_E}{\frac{dx}{dt}}$) is constant for all values of V_0.

For a time varying velocity, however, the r_{fv} ratio is not constant. For a sinusoidal displacement profile ($x = A\sin(\omega t)$), the electromagnetic damping force (F_{Esin}) is given by:

$$\begin{aligned} F_{Esin} = & C_2 e^{-\frac{R_{coil}+R_{ext}}{L_{coil}}t} \\ & + \frac{-{k_v}^2}{\sqrt{(R_{coil}+R_{ext})^2 + (\omega L_{coil})^2}} A\omega\cos(\omega t+\theta), \end{aligned} \tag{2.38}$$

where A and ω are the amplitude and angular frequency of the excitation, C_2 is a constant determined based on the initial condition, and θ is the phase shift between input displacement and output force which is given by:

$$\theta = \arctan\left(-\frac{\omega L_{coil}}{R_{coil}+R_{ext}}\right), \tag{2.39}$$

Neglecting the first term of equation 2.38, the r_{fv} ratio is found to be:

$$r_{fv} = \frac{{k_v}^2}{\sqrt{(R_{coil}+R_{ext})^2 + (\omega L_{coil})^2}}, \tag{2.40}$$

For simplicity, consider the case where coils are short circuited (R_{load}=0). The r_{fv} for this case becomes:

$$r_{fv_{short\ circuited}} = \frac{{k_v}^2}{\sqrt{(R_{coil})^2 + (\omega L_{coil})^2}}, \tag{2.41}$$

Here we assume that an original damper has been built, and then we are building a new damper similar to the original one but in a larger or smaller scale. We define a parameter, Sc_f scale factor, to represent the scale of a new damper comparing to the original one. This means that in the new damper, all the dimensions of the original damper are multiplied by Sc_f. By keeping the same geometry design ratios (like $\frac{\tau_m}{\tau_i}$, $\frac{\tau}{r_c}$ from Figure 2.2, etc.), and taking the scale factor (Sc_f) and wire size (A_{wire}) as variables, the values of R_{coil}, L_{coil} and k_v (given in equation 2.41), can be expanded as follows:

$$R_{coil} = \frac{2\pi r_{avg}}{\sigma A_{wire}} N \propto \frac{Sc_f}{A_{wire}} \frac{{Sc_f}^2}{A_{wire}} \propto \frac{{Sc_f}^3}{{A_{wire}}^2}, \tag{2.42}$$

$$L_{coil} = \frac{N^2}{\int \frac{dl}{\mu A_{coil}}} \propto \frac{\left(\frac{{Sc_f}^2}{A_{wire}}\right)^2}{\frac{Sc_f}{{Sc_f}^2}} \propto \frac{{Sc_f}^5}{{A_{wire}}^2}, \tag{2.43}$$

$$k_v \propto \left(\frac{{Sc_f}^2}{A_{wire}}\right) \frac{{Sc_f}^2}{Sc_f} \propto \frac{{Sc_f}^3}{A_{wire}}, \tag{2.44}$$

where r_{avg}, N, A_{wire}, σ, μ, A_{coil} and dl are the average radius of the coil, the number of turns in the coil, the area of the wire, the conductivity of the wire, permeability of coil core, the area of the coil and an infinitesimal length of the coil along its axis respectively. According to equations 2.42-2.44, each of R_{coil} and L_{coil} and k_v has different proportionalities to A_{wire} and Sc_f. Due to these differences, as the wire size and scale for the same design change, the damper exhibits different performances. The effect of A_{wire} on the damper performance is studied later in Section 2.4.2. For this section, it is presumed that the wire gauge of the coils is kept the same as the original design, the parameters of R_{coil}, L_{coil} and k_v are then rewritten as:

$$R_{coil} = C_R {Sc_f}^3, \tag{2.45}$$

$$L_{coil} = C_L {Sc_f}^5, \tag{2.46}$$

$$k_v = C_k {Sc_f}^3, \tag{2.47}$$

In these equations, C_R, C_L and C_k are respectively equal to R_{coil}, L_{coil} and k_v of the preliminary optimization design ([50]) with Sc_f=1.

In the next step, equations 2.45-2.47 are replaced into equation 2.41 to establishes a relation between the r_{fv} (force over velocity ratio) of the designed damper, and the scale factor and the excitation frequency.

$$r_{fv} = \frac{{C_k}^2}{\sqrt{\frac{{C_R}^2}{{Sc_f}^6} + \frac{\omega^2 {C_L}^2}{{Sc_f}^2}}}, \tag{2.48}$$

Based on this relation, the impact of the inductance on the damper performance varies at different scales and frequencies. Figure 2.11 illustrates the inaccuracies of the models in predicting the force and r_{fv} values respectively if the inductance is neglected. According

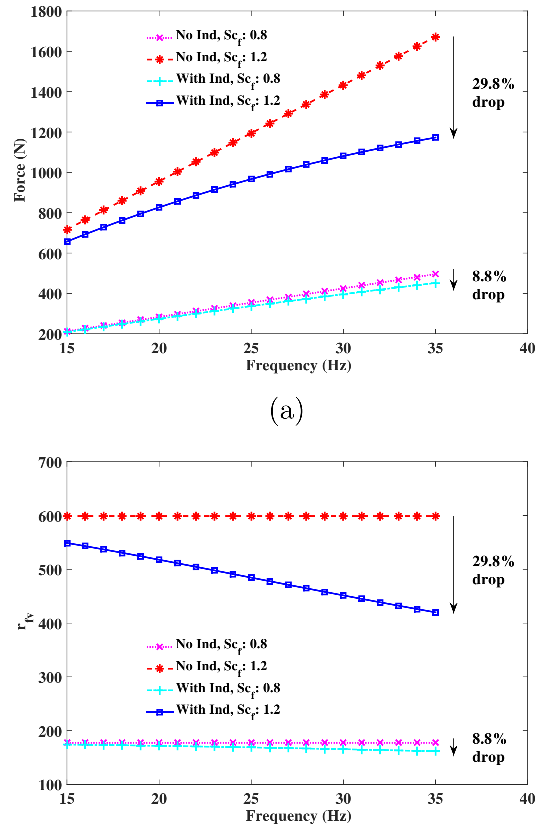

(a)

(b)

Figure 2.11: The effect of neglecting inductance in calculating a: damping force, and b: force over velocity ratio (r_{fv}).

to this figure, as excitation frequency increases or the damper scales up to larger sizes, the effects of the inductance become more relevant and thus less negligible. One practical conclusion is that if an existing damper design developed for a specific application, is taken as a basis for building new dampers at different scale sizes and/or working frequencies, then the designer needs to have an estimation for the performance of the current design at those new conditions. For example, consider the original designed damper and the new damper to have a scale factor of Sc_{f_1} and Sc_{f_2}, a working frequency of ω_1 and ω_2, and a force to velocity ratio of r_{fv_1} and r_{fv_2} respectively. In the follow, for comparing the force to velocity ratio of the new damper and the original one, $\frac{r_{fv_2}}{r_{fv_1}}$ is calcualted where r_{fv_1} and r_{fv_2} are obtained from equation 2.48. In the first case, the working frequency of the new damper is kept the same as the original one (i.e. $\omega_2 = \omega_1 = \omega$). By setting the scale factor of the original design to $Sc_{f_1} = 1$, the force to velocity ratio of the new damper (r_{fv_2}) at different scale factors (Sc_{f_2}) is calculated by as:

$$\frac{r_{fv_2}}{r_{fv_1}} = \frac{\sqrt{1+\omega^2\alpha^2}}{\sqrt{\frac{1}{{Sc_{f_2}}^6} + \frac{\omega^2\alpha^2}{{Sc_{f_2}}^2}}}, \tag{2.49}$$

where α is a constant that represents $\frac{C_L}{C_R}$, and for a damper with short circuited coil, its magnitude (based on the definition and and geometric formulas of L_{coil} and R_{coil}) is equal to:

$$\alpha = \frac{\sigma\mu_0\left(r_c - r_a\right)\left(r_c + r_a\right)^2}{4}, \tag{2.50}$$

In the second case, the scale factor of the new damper is kept the same as the original one (i.e. $Sc_{f_2} = Sc_{f_1} = Sc_f$). By presuming the working frequency of the original damper design to be $\omega_1 = 2\pi \times 15\ rad/sec$, the force to velocity ratio of the new damper (r_{fv_2}) is calculated as:

$$\frac{r_{fv2}}{r_{fv_1}} = \frac{\sqrt{\frac{1}{(Sc_f)^4} + {\omega_1}^2\alpha^2}}{\sqrt{\frac{1}{(Sc_f)^4} + {\omega_2}^2\alpha^2}}, \tag{2.51}$$

Figures 2.12 and 2.13 present the results of these two case studies obtained from FEM and analytical models (equations 2.49 and 2.51 respectively).

Figures 2.11-2.13 are generated for given $\alpha = 0.00321$ (obtained from equation 2.50) for a damper prototyped in Section 3.1. Similar graphs can be generated for other designs with different α.

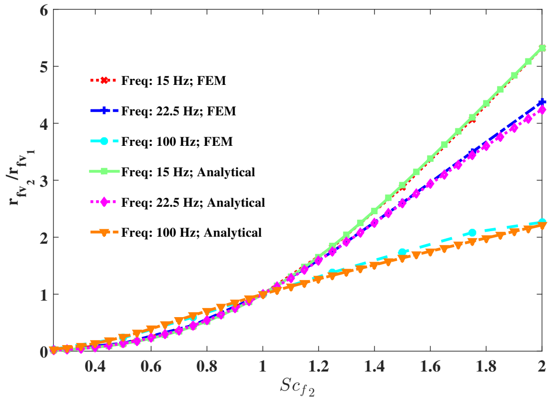

Figure 2.12: Variation of force over velocity ratio (r_{fv}) at different scale factors ($\omega_2 = \omega_1$, $Sc_{f_1} = 1$).

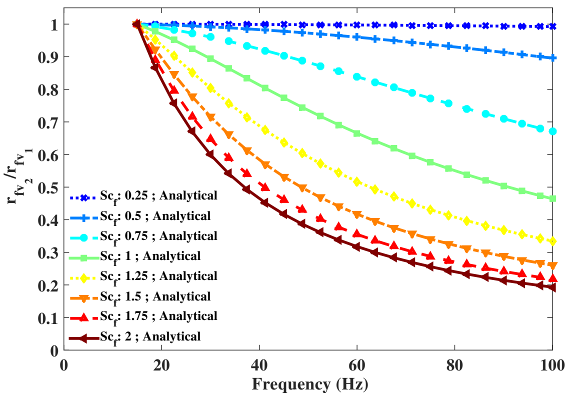

Figure 2.13: Variation of force over velocity ratio (r_{fv}) at different frequencies ($Sc_{f_2} = Sc_{f_1}$, $\omega_1 = 2\pi \times 15$).

The results presented in this section, question the suitability and representability of force and power densities parameters for comparison purposes. Currently force and power densities are known as the most common approaches for comparing different damper designs. In this approach, the damping force and regenerated power are divided by the damper volume (to obtain the force and power densities) so that optimized designs at different sizes can be compared to each other. It should be highlighted that the volume of a design is increasing cubically with Sc_f value, and this is while equation 2.49 indicates that the r_{fv} increments is cubic only if the inductance C_L of the original design is negligible (which is not in some cases) or the working frequency (ω) is zero (constant velocity: $\frac{dx}{dt} = V_0$).

Another relevant raised question about the damper design is that whether the geometry optimization process should be repeated if the scale and working frequency of damper are changed or the same geometric ratios (i.e. $\frac{\tau_m}{\tau_i}$, $\frac{\tau}{r_c}$, etc.) can be implemented. This answer to this question is left as a future research topic.

Effects of Excitation Amplitude

Researchers perform the process of geometry optimization by maximizing the damping force of the device at a presumed excitation condition. The excitation condition is chosen in accordance with the targeted application, and typically includes a harmonic excitation with constant amplitude. Since the application of those designs varies among the researchers, different excitation amplitudes are implemented in the optimization process. The relation between the displacement amplitude and the damper output was previously given in equations 2.15, 2.16 and 2.19 where for simplicity it was assumed radial magnetic field density inside the coils (B_c) is constant, and this is while, B_c value varies along the armature shaft. In order to illustrate this variation, Figure 2.14 is provided using FEM, where radial magnetic flux density inside the coils is shown by color map.

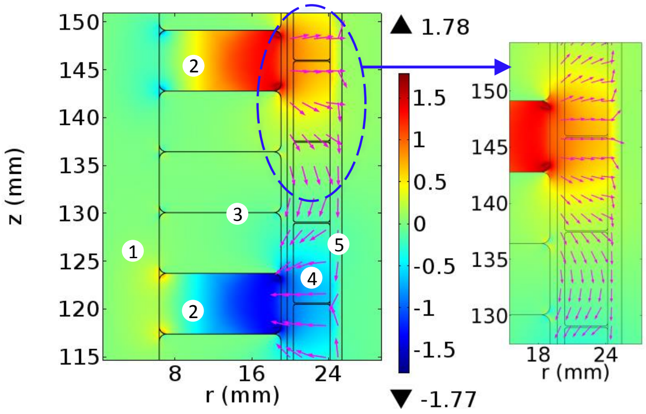

Figure 2.14: Radial magnetic flux density at 1: armature central rod, 2: iron poles, 3: magnets, 4: coils, and 5: conductor tube. Magenta arrows represents the magnetic flux direction inside the coils.

Due to the variation of the radial magnetic flux in the coils, it is possible that the displacement amplitude (selected based on the application) can affect optimization results. To examine this possibility, two series of simulations are performed with excitation amplitudes of 3.175 mm (0.25 in) and 9.525 mm (0.75 in). The idea here is to maximize the damping force at those displacement amplitudes by changing the $\frac{\tau_m}{\tau_i}$ ratio while keeping the rest of the damper dimensions constant. Also, in order to avoid magnetic saturation, the thickness of conductor tube is doubled comparing with the original model. The results of these simulations are presented in Figure 2.15. The results demonstrate that by increasing the excitation amplitude from 3.175 mm (0.25 in) to 9.525 mm (0.75 in), the $\frac{\tau_m}{\tau_i}$ ratio that corresponds to the maximum force peak changes from 5.2 to 6. A supporting finding is also reported in the study by D. Zhu et al., [97, 98]. They have implemented different magnet arrangements to maximize the power of their energy harvester. They reported that some arrangements such as halbach array can help to increase the B_{max}, however, higher powers are rather generated using simple magnets with proper magnet ratio (in the presented case the equivalent ratio is $\frac{\tau_m}{\tau_i}$). Furthermore, due to magnetic flux gradient effects, the value of the proper magnet ratio varies for different excitation amplitudes.

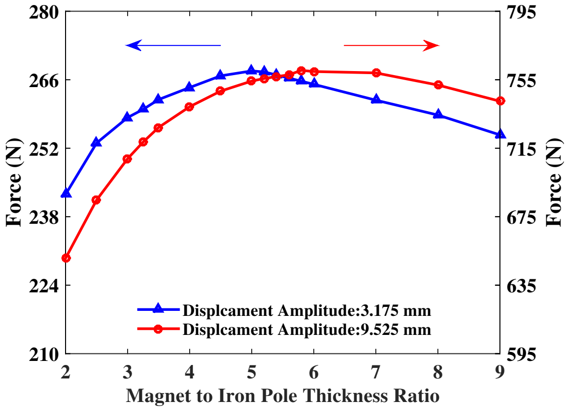

Figure 2.15: The effect of displacement amplitude on the optimum τ_m/τ_i ratio.

To the best of our knowledge, no study has dealt with the variation of the excitation amplitude in the electromagnetic dampers and hence it is desirable to conduct a more extensive study to assess the preliminary conclusions given here.

Coil Wire Size (or A_{wire})

In optimization strategies, the wire size (A_{wire}) is not usually considered as a parameter of interest and rather is set constant [7]. In this section, the effect of varying A_{wire} on system performance is briefly discussed. There are two groups of systems that need to be discussed separately (A summary of these discussions is presented in Table 2.2).

In the first group (group 1), the profile of the input velocity ($\frac{dx}{dt}$) to the damper is strictly enforced, meaning that damper excitations are not affected by damper properties. For those systems, it can be proven that that the maximum damping force (situation 1) occurs when impedance of the load is equal to zero. To understand the effect of A_{wire} on this force, one can look at equations 2.42-2.44 where the dependency of R_{coil}, L_{coil} and k_v to the wire size are given. By implementing these values into r_{fv} equation for a system with zero load impedance, it can be shown that varying the size of wire does not affect the magnitude of the maximum damping force. For the purpose of obtaining the maximum power regeneration (situation 2), the Thevenin maximum power transfer theorem should be employed. The theorem states that, the impedance of the external load should match the coils impedance. Similar to situation s1, for situation s2 again can it be shown that the value of the maximum power is independent of A_{wire}; however, if the external resistance is already chosen, then the coils A_{wire} should be selected accordingly such that the theorem is satisfied.

Table 2.2: Summary of the methods used for selecting internal and external resistances.

	Electromagnetic Damper			
Condition (group #)	Enforced velocity (group 1)		Not Enforced velocity (group 1)	
Objective (situation #)	Maximum Damping (situation 1)	Maximum power (situation 2)	Optimum Damping (situation 3)	Maximum Power (situation 4)
Implemented Theory	—	Thevenin maximum power transfer	Hartog fixed point [99]	Design procedure of Soilman et.al.
Summary of Theory	$R_{ext} = 0$	$R_{ext} = R_{coil}$	Modify the location of the fix point in frequency response curves by changing the total resistance	1- Match electrical and mechanical damping coefficients by changing total resistance. 2- Optimize the ratio of internal to external resistance
Must select wire size and the external load simultaneously?	No	No	Yes	Yes

Unlike the first group, in the second group (group 2) the velocity profile of the damper is not prescribed and, based on the properties of the electromagnetic damper, it can change (e.g. a 2 DOF vehicle suspension model with an electromagnetic damper). The reason for such behavior is that, because the mechanical and electrical subsystems of the electromagnetic damper are dynamically coupled, changing the properties of one will affect the other [100]. As a consequence, the requirements for the optimal damping and maximum power objectives are different than previous group. Hence, different theorems should be implemented for obtaining those objectives. For achieving the optimal damping coefficient (which depends on the application and is not necessarily a maximum value), the fixed point method by Hartog [99] can be utilized (situation 3). All the frequency response curves of a mass-spring-damper system pass a fixed point which according to the Hartog method can be used to modify impedance of the total circuit (summation of internal and external impedances) for optimizing the damping coefficient. To obtain the maximum power regeneration mode (situation 4), the design procedure of Soliman et.al. [100] can be applied. This procedure includes two steps. In the first step, the total impedance of the electrical subsystem (internal coils plus external loads) is tuned to make the electrical and mechanical damping coefficients equal to each other. This adjustment ensures that the energy flow from the mechanical to electrical subsystem is maximized. Since the mechanical damping coefficient depends on the ambient condition, the first step should be repeated for new applications. In the second step, the wire size (A_{wire}) and the storage unit load are selected together such that, while still maintaining the tuned total impedance, the maximum fraction of power is delivered to the external load rather than being lost in the coils.

Most of the damping systems are categorized in the second group (g2). Despite the first group, here the designers have more challenging tasks as they need to take into account the application as well as the ambient condition of the damper. Furthermore, for these systems, they have limitations with respect to the external resistance and coil wire size selection because they must be chosen simultaneously (and not consecutively). For a system in second group where the either coils wire size (A_{wire}) or external load is already chosen, the same theories, as discussed above, can be applied for choosing the proper value of the other one; however, the objective (optimal damping or maximum power) might not be completely achievable. For instance, in a system in situation s3, if the preselected internal resistance is already larger than the optimal total resistance, then the optimal condition is not reachable [101].

Chapter 3

Semi-active Hybrid Electromagnetic Damper: Experimental and Simulation Results

In this chapter, based on the proposed design and the optimization results, a hybrid electromagnetic damper is prototyped. In order to validate the FEM model, the electromagnetic component is experimentally characterized. The results show a good agreement in the estimation of the magnetic field density, electromagnetic damping force and regenerated power. The analytical model for the viscous damping force, is also validated with experimental results. Finally, in Section 3.4, the design of a custom signal conditioning circuit is presented for the management of the various output voltages. This circuit is responsible for regulating the output of the damper to the requisite level for energy storage in batteries.

3.1 Prototype Development

Based on the design described in the previous chapter, the hybrid damper prototype is built, and is shown in Figure 3.1.

The first prototype has a stroke of 76.2 *mm* (3 *in*) with a fully extended length of 506.73 *mm* (19.95 *in*). The main body is 76.2 *mm* (3 *in*) by 76.2 *mm* (3 *in*) by 307.975 *mm* (12.125 *in*). The damper weights 6.42 *kg* (14.15 *lbs*), however this is not representative weight of the commercial product. It is anticipated that a commercial implantation could reduce weight by 35% to $\sim$ 4.17 *kg* (9.19 *lbs*).

Figure 3.1: Hybrid damper prototype.

During the manufacturing process a few problems occurred that made the first prototype deviate from the target optimized design in some aspects. The purchased coils were slightly bigger than the provided spaces (between separator aluminum tube and conductor tube). This is addressed by taking out a layer of wires from the outer diameter of the coils. This change roughly reduces the number of turns in each coil from ~ 275 to ~ 245. Also the conductivity of the coils is measured and found to be around $5.3e7\ Sm^{-1}$; which is lower than the expected value of $5.96e7\ Sm^{-1}$. These factors reduce the performance of the electromagnetic component of the damper with respect to the damping force and regenerative power. A modified version of the FEM model is also developed based on these changes so that its output could be compared with the experimental results. In the rest of this report this model is called *modified FEM model*.

3.2 Magnetic Flux Measurement

To validate the accuracy of the modified FEM model, the magnetic field density is measured experimentally and compared with the modified FEM model.

In the experimental setup shown in Figure 3.2a, B_r is measured using a Lakeshore 410 gauss meter. To move the gauss meter accurately, it is attached to a SCARA robot built by EPSON. The robot is able to move the meter in a 3D space with a displacement resolution of $\sim 0.003\ mm$. Using the robot the meter is placed at a distance of $0.5\ mm$ relative to the surface of the magnets and poles, and then moved vertically (z direction) up and down ($0 \leq z \leq 3.25\tau$).

The comparison between the experimental data and model-predicted values is presented in Figure 3.2b. This figure indicates an excellent agreement between simulation and experimental results. This result validates the accuracy of the FEM model and the optimization solution.

In Figure 3.2b, the irregularities that are observed in locations like $z = 0.5\tau = 12.7\ mm$

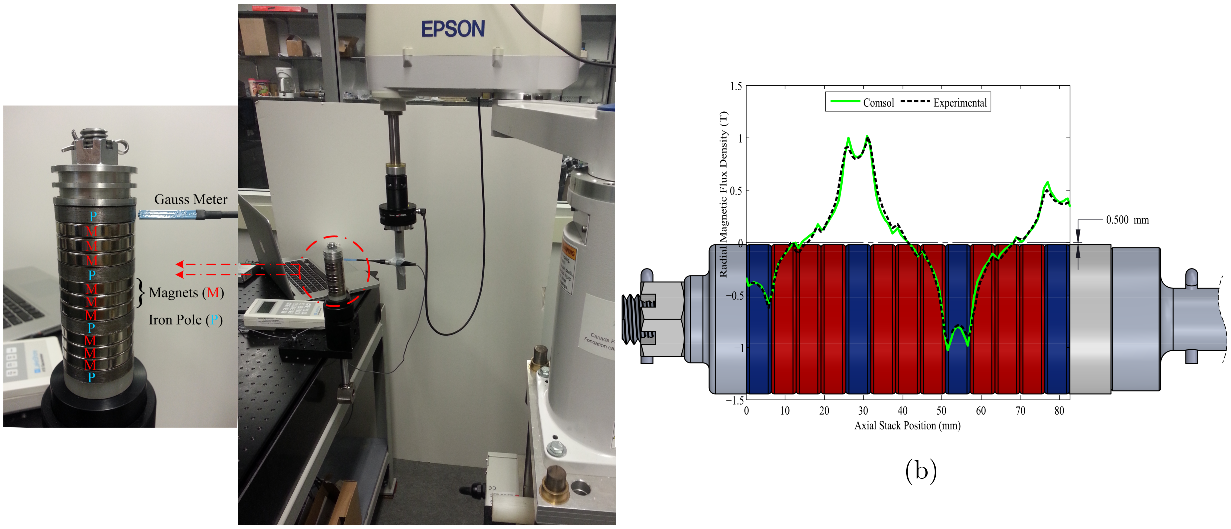

(a)

(b)

Figure 3.2: Magnetic flux density measurement along the armature magnet-iron array, a: experimental setup, and b: measured radial flux densities.

($0.5\ in$) and $z = 0.75\tau = 19.05\ mm$ ($0.75\ in$) are attributed to the corner fillets of the magnets. Each magnet section in the armature array is a not a single part but rather is made of three small magnets with $\tau_m/3$ thickness. It is observed that reducing the fillet size of the small magnets in the modified FEM model would eliminate those irregularities but makes the results less accurate relative to the experimental results.

3.3 Hybrid Damper Force and Power

The experimental setup shown in Figure 3.3 is configured to measure damping force and regenerated power of the damper at different combinations of input excitation and shunted external resistance to the coils. A Futek LCF450 pancake force transducer and a Celesco SP2 string potentiometer are employed to measure force and displacement. The pressure and the acceleration of the damper are also measured using a Honeywell PX2 pressure transducer and a Kistler 8305B10M2 accelerometer. All of the sensors are interfaced with LABVIEW using an NI-6210 DAQ. Furthermore a NI-6225 DAQ is used to measure the voltages and currents (using current sensor resistance) of coils and external loads. A V721 LDS shaker is used to excite the hybrid damper. This shaker can operate within a frequency range of 5-4000 Hz with either a sine wave or random profile. To connect the damper to the shaker, a spherical rod end is used on the top and bottom. Using a function generator as the controller, the shaker is configured to apply a sinusoidal excitation to the hybrid damper according to the selected frequency and amplitude.

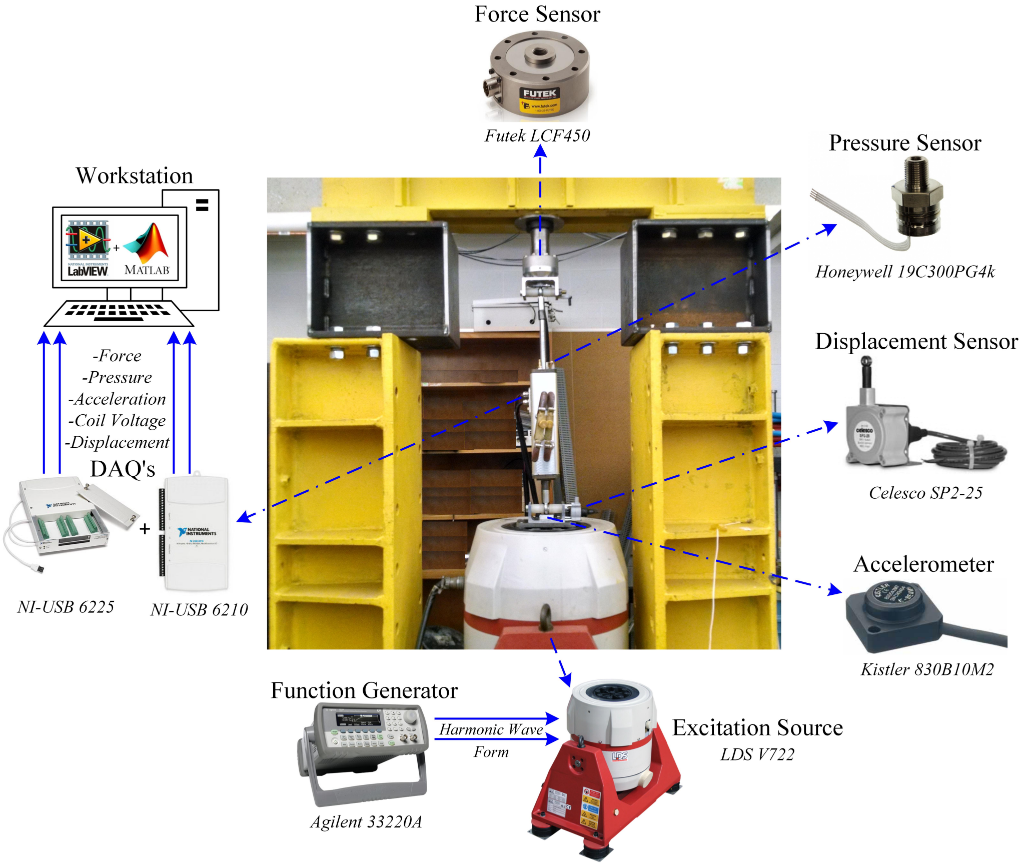

Figure 3.3: Experimental setup for harmonic excitation.

Due to the experimental limitations of the shaker controller, the amplitude and frequency of the excitations could not be chosen independent of each other. Therefore it is not possible to excite the damper at exactly the same frequency-amplitude pair as the one used for previous simulations and optimizations. Here for each circuit condition, the damper is tested at frequencies from 5 to 15 Hz (to 25 Hz for friction force) in increments of 5 Hz. To compare the experimental results with simulations. The experimental amplitudes measured at those frequencies are then used to simulate the modified FEM model.

The two main parameters of interest for the characterization are: A) regenerated power and B) damping force. The power is solely generated by the electromagnetic component, while the damping force is produced by both of electromagnetic and hydraulic components. Additionally, friction force is an avoidable factor, and should be considered in the characterization experiments. Therefore, experimental protocols are developed to characterize electromagnetic power as well as hydraulic, electromagnetic and friction forces. It should be noted that, in the experimental results, due to the weight of the equipment, there is an offset in the measured forces that is removed (by subtracting the average of the forces).

3.3.1 Friction and Hydraulic Forces

The friction force is attributed to interaction of the seals (located inside the top cap) and the piston rod. Once the friction force is characterized, it can be subtracted from other experiments measurements so that electromagnetic and hydraulic forces can be calculated. If the friction force is not accounted for, the obtained damping forces for electromagnetic and hydraulic components will be skewed. With respect to the friction, in Figure 3.4, it is observed that the damper holds the same force-velocity characteristics at all the applied excitations.

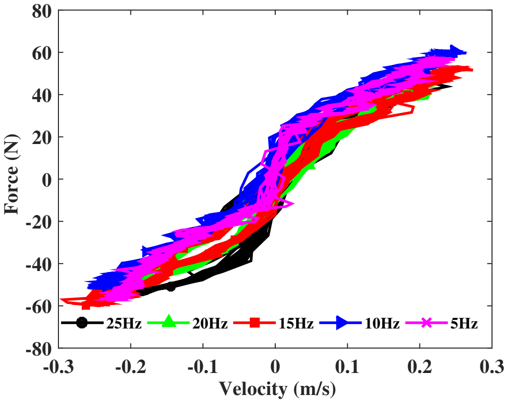

Figure 3.4: Experimental results for friction force.

The experimental test for hydraulic force is performed by disabling the electromagnetic component (putting all the coils in open circuit configuration), adding oil into the viscous medium and pressurizing the oil (80 psi) by inert gas. Figure 3.5 compares the hydraulic force results for an excitation of 10 Hz obtained from simulation and experiments. This figure shows that a good agreement exists between the simulation and experimental results that validates the accuracy of the hydraulic model. Furthermore, the haydralic force for other frequencies are also presented in Figure 3.6. On average, the damping coefficient of the hydraulic component is measured to be 1302 Nsm^{-1}. This coefficient can be further adjusted by tuning the external unidirectional valves, if required.

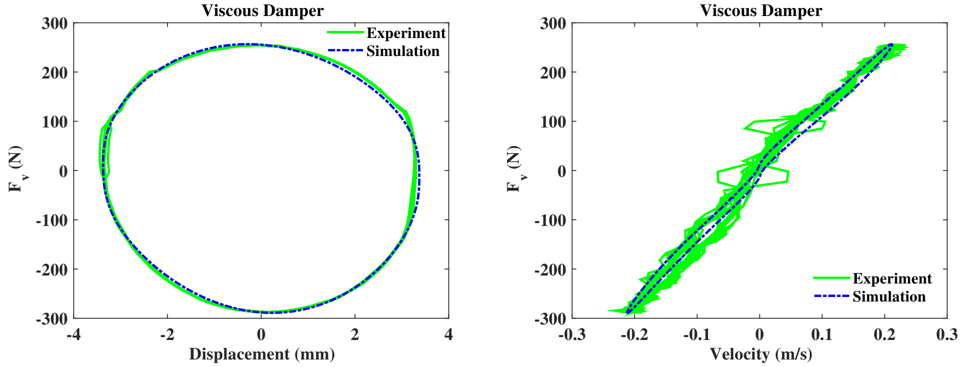

(a) (b)

Figure 3.5: Twin tube viscous damper, a: damping force versus displacement, and b: damping force versus velocity.

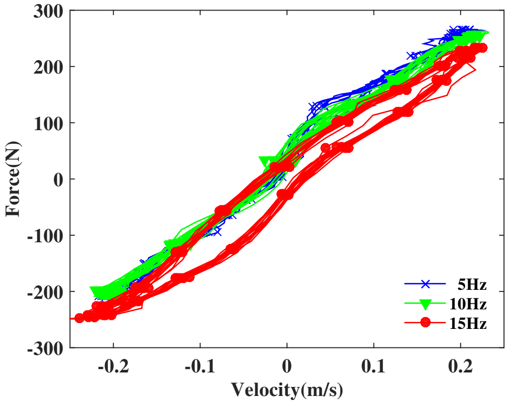

Figure 3.6: Experimental hydraulic force characterization at 80 psi gas pressure.

3.3.2 Electromagnetic Force and Power

The electromagnetic component is a 3 phase linear motor. At a given excitation condition, the performance of the electromagnetic component, in terms of regenerated power and electromagnetic force, depends on the circuit as well as the external load. The connections that are used in this work include standard, delta and star. The standard configuration consists of each coil being connected to an individual variable resistance. In the star and delta configurations, the coils R1-R5, G1-G5 and B1-B5 are connected in series to make the three phases (R, G and B) of damper. Then for the star/delta configuration, the three phases are connected to each other in star/delta, and further are connected to a star/delta load, respectively (Figure 3.7). Comparing to other circuit conditions, standard configuration is able to generate higher forces. This can be explained based on the phase shift of coils voltages. The voltages of different coils have phase shifts with respect to each other which results in voltage cancellation, and thus lower force generation if they are connected to each other. In standard configuration, however, coils are separately short circuited to themselves and thus no voltages cancellation occurs

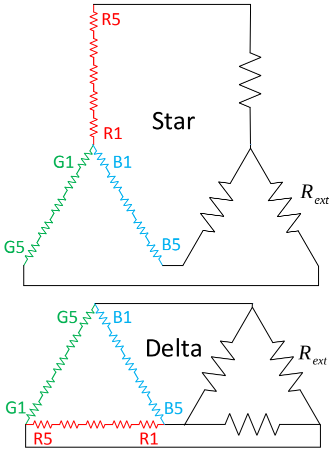

Figure 3.7: Star and delta configurations, R1-R5, G1-G5 and B1-B5 represent the 15 coils of the three-phase damper, and R_{ext} represents the external resistance.

The maximum achievable electromagnetic damping force at any circuit configurations (standard, star and delta) occurs when the external load is set to zero which also corresponds zero power generation. The damping forces for a short circuit standard configuration are shown in Figure 3.8. These results are measured at an amplitude and frequency of

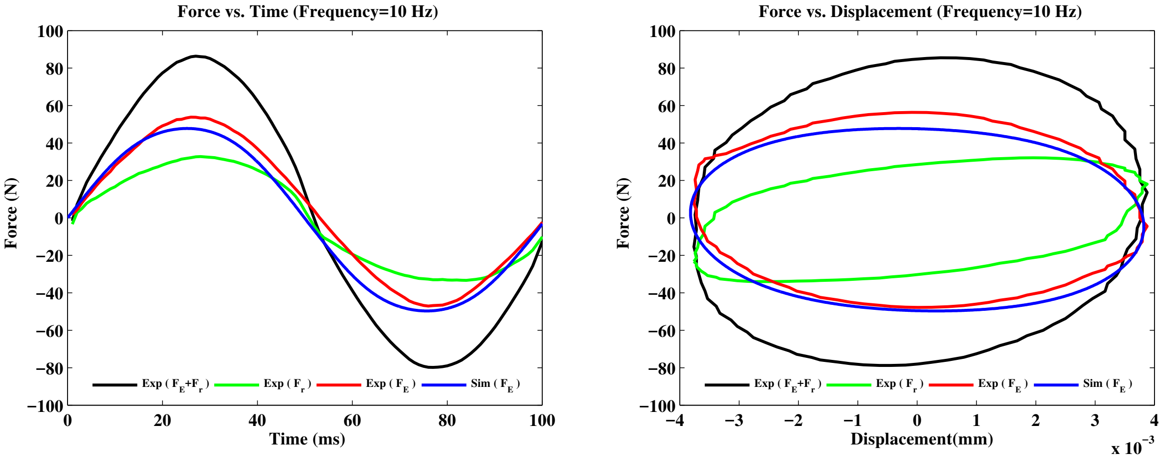

(a) (b)

Figure 3.8: Experimental results for maximum electromagnetic damping force, a: force vs. time, and b: force vs. displacement.

3.82 mm (0.15 in) and 10 Hz respectively. In order to compare the experimental results with the simulation, first the friction force is measured and then deducted from the total (friction and electromagnetic) force. As seen in Figure 3.8, a nice agreement between the results of experiments (red color) and simulations (blue color) is obtained.

The electromagnetic damping force, in standard configuration, is also measured for other excitation frequencies and depicted in Figure 3.9.

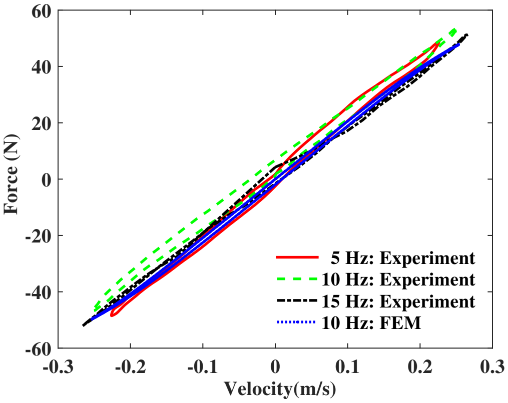

Figure 3.9: Electromagnetic damping force in short circuited standard configuration.

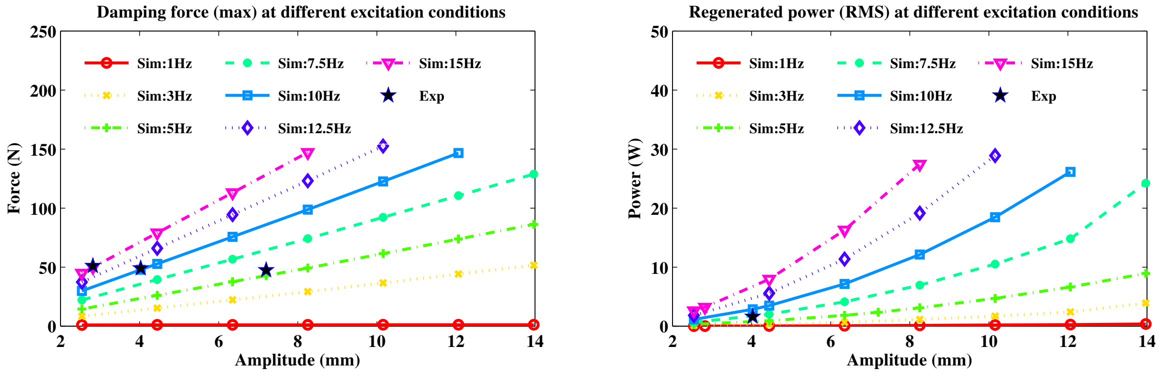

(a) (b)

Figure 3.10: Electromagnetic damper performance at different excitation conditions, a: force (max), and b: power (RMS).

The corresponding electromagnetic damping coefficient for obtained results is $\sim 200\ Nsm^{-1}$. This means that by changing the external resistance connected to each coil from zero (short circuited) to infinity (open loop), the damping coefficient of electromagnetic component can vary between $\sim 200\ Nsm^{-1}$ to 0 respectively. This value is slightly lower than 238 Nsm^{-1} that the damper is initially designed for (Section 2.4.1). This is ultimately attributed to the previously mentioned manufacturing errors.

To better understand the performance of the electromagnetic component, further simulations are carried out for the standard configuration at various input excitations. Figure 3.10 presents the maximum force and maximum regenerated power obtained from simulations at those excitations. For finding the maximum force, each coil is short circuited while the maximum regenerated power is obtained by matching the external resistance with the internal resistance of each coil. For a limited number of the input conditions; experimental data is also available and added to the figures.

Effect of External Resistance

Figure 3.11 illustrates the effect of changing the external electrical load on electromagnetic damping force and regenerated power for standard, star and delta configurations. The showcase experimental results obtained for amplitude and frequency of 4.03 mm and 10 Hz, respectively. In Figure 3.11, for star/delta configurations, R_{ext} represents the resistance of one of the branches of the external star/delta loads and R_{coil} is the summation of the resistance of coils in any of the phases in the damper (e.g. G1+G2+...+G5).

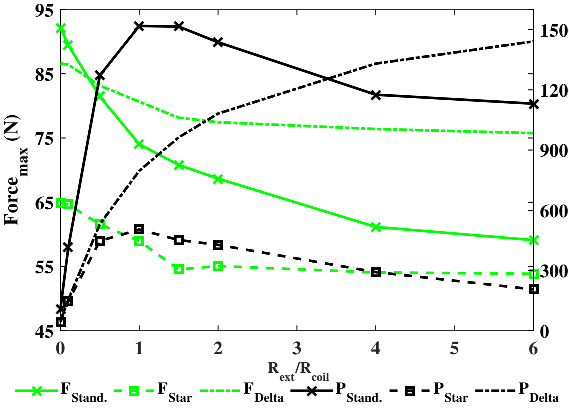

Figure 3.11: The effect of external load on damper performance for standard, star, and delta configurations.

In all the configurations, as $r = R_{ext}/R_{coil}$ ratio increases from zero to infinity, the damping force decrease from its maximum (happening at $r = 0$) to its minimum value which is mechanical friction force. The regenerated power, on the other hand, increases from zero (happening at $r = 0$) until it reaches a maximum value and then it drops to zero again. Comparing to the other two configurations, the standard configuration shows the highest rates of damping force and regenerated power; however, this configuration requires a more complicated electronic system for storing the regenerated energy from all 15 coils into a storage unit. Also, delta configuration shows higher outputs comparing to star, and its performance is less sensitive to variation of external load.

Damping Tuning

The corresponding damping coefficient of the viscous component of the damper is measured to be 1302 Nsm^{-1}. By adding this coefficient to one from the electromagnetic system (0-238 Nsm^{-1}), the hybrid damper is able to produce a total variable damping coefficient of 1300-1538 Nsm^{-1}. This variability can be exploited as a tool to enhance the dynamic performance of system according to the road profile and driving condition. To achieve variable damping, the apparent external resistance shunted across each coil requires adjustment through an electrical circuit and controller. In the next section, this requirement is met by designing a custom signal conditioner circuit.

3.4 Voltage Signal Conditioning

Signal conditioning for this design is an imperative task due to its effect on damper performance (force and power recovery). Electromagnetic dampers are usually subjected to wideband excitations which results in a time-varying output voltage and current profiles. Furthermore, the energy storage units such as batteries present variable load characteristics. Due to these variations, energy storage efficiency can be significantly affected by the power electronics circuits used in the system. The settings of the signal conditioner also affect the functionality of the damper. As it is seen in the simulations and experiments, by defining the apparent resistance of shunted circuit (here the signal conditioner), we can control the rate of the produced power and forces in the electromagnetic damper. Thus, custom electronics are required to properly condition the voltage such that the recovered energy can be stored efficiently, and the performance of the damper be tuned according to the demand.

Signal conditioning of an electromagnetic damper with a random voltage source is still an active area and different researches have tried to propose techniques to address the above mentioned concerns. Readers are referred to [102] for more information on the research in this area. In this study, a preliminary circuit board is designed based on a DC-DC buck booster chip.

The induced voltage is an alternating voltage whose amplitude and frequency depends on the damper input excitation. In order to find the typical input excitations for a vehicle suspension damper, road profile of class C (average) is generated using PSD method [103] and is fed as input to a conventional suspension system. Based on the damper displacements in the average road, an excitation condition with an amplitude and frequency of 12.7 mm (0.5 in) and 15 Hz is assumed as the worst-case scenario. Considering these assumptions, simulations are conducted, and it is found that the output voltage could vary between -75 to 75 V. Accordingly, it is decided to condition the generated voltages in two steps. In the first step, the AC voltage is rectified to produce a DC voltage (the fabricated rectifier printed circuit board (PCB) is shown in Figure 3.12), and in the second step the level of the DC voltage is adjusted according to the charging characteristics of the storage unit as well as the desired rate of damping force and power. The voltage regulator should have a high efficiency to minimize the energy loss, and also it should have a wide working range due to the excitation of the damper yielding anything from a few volts to 75 V. The LT8705 buck booster from Linear Technology Corporation is an efficient (up to 98%) switching buck booster that can regulate the output voltages above, below or equal to the input voltage [104]. Figure 3.13 shows the designed circuit (and the fabricated PCB) using the LT8705 chip.

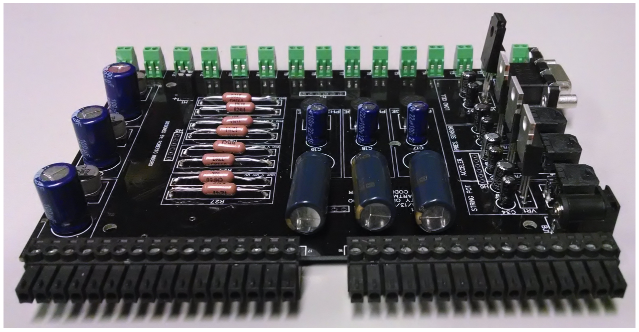

Figure 3.12: Rectifier PCB.

In this circuit, by changing the value of $\frac{R_{11}}{R_{12}}$ or R_{12} the user can regulate the output voltage or current respectively. To study the functionality of the proposed design, LT spice VI software package is utilized to model the circuit. This software has a built-in library that allows for circuit simulation using the LT8750 chip.

A harmonic voltage signal in the form of:

$$V = 15 + 7\sin(2\pi t) + 2\sin(20\pi t) + 0.5\sin(60\pi t) \tag{3.1}$$

is applied to the circuit. This voltage is the summation of a bias, low, medium and high frequency sinusoidal signal. The results shown in Figure 3.14 indicates that the circuit is able to regulate the fast varying input signal to produce a relatively constant output current RMS.

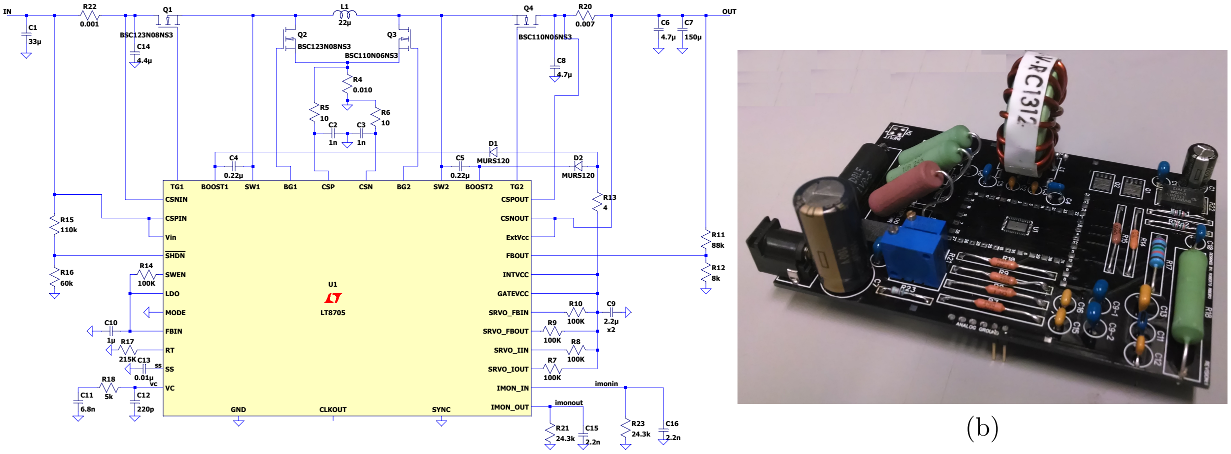

(a)

(b)

Figure 3.13: Buck-booster circuit using the LT8705 chip, a: the designed circuit, and b: the fabricated PCB.

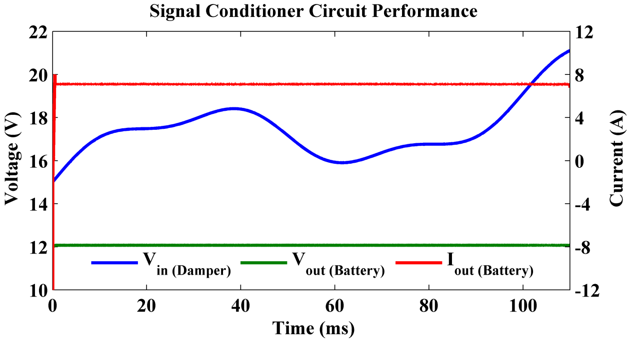

Figure 3.14: Buck- booster circuit performance under the variation of the input signal.

Chapter 4

Application of Hybrid Electromagnetic Damper to Vehicle Suspension System

This chapter is allocated to optimization and performance evaluation of a suspension system, equipped with a hybrid electromagnetic damper. The hybrid damper is configured to operate with a hydraulic and an electromagnetic component. For analyzing the system, the electromagnetic component is modeled and integrated into a 2 DOF quarter car model. Three criteria are considered for evaluating the performance of the suspension system: ride comfort, road holding, and regenerated power. Using the genetic algorithm multi-objective optimization (NSGA-II), the suspension design is optimized to improve the performance of the vehicle with respect to the selected criteria. The multi-objective optimization method provides us with a set of solutions called Pareto front in which all solutions are equally good and selection of each one depends on conditions and needs. Among the given solutions in the Pareto front, a few cases, with different design purposes, are selected. The performances of the selected designs are compared with two reference systems: a conventional and a not-optimized hybrid suspension system. The results show that the ride comfort and road holding qualities of the optimized hybrid system are improved, and the regenerated power is considerably increased.

In Chapters 2-3 we proposed a hybrid electromagnetic damper to overcome the limitations of the electromagnetic dampers. In this new design, a passive hydraulic medium was integrated with an electromagnetic semi-active generator into a single unit. The electromagnetic and hydraulic components have different dynamic properties that should be considered when designing the hybrid suspension system. For instance, the electromagnetic generator does not show a pure damping characteristic, thus, its functionality can affect the rest of the suspension components. Another point to consider is that a larger electromagnetic component corresponds to higher inherent inductance and time delay while a downsized electromagnetic component has insufficient rates of power regeneration. Therefore, it is a valid question that whether it is possible to design a hybrid suspension that performs dynamically equal or better comparing to a conventional damper with the added benefit of power generation. In this chapter, we try to answer the above question by choosing an adequate selection of the suspension parameters, a task that is accomplished using a multi-objective optimization approach. As an adaptive and regenerative system, the suspension is required to provide not only ride comfort and handling quality but also maximum regenerated power. A trade-off should be done between these three criteria which arises complexity in the design process.

The compromise between the design criteria could be handled using optimization methods. The optimum suspension design has been an important practical problem for all kind of conventional, active and semi-active suspension systems [105–109]. Optimization of suspension systems are often performed by combining the design requirements into a single weighted objective function [105–109]. However, the significant drawback of this approach is that the arbitrary weighting coefficients need to be preselected, and the obtained results largely depend on the weighting coefficient [110, 111]. Using this approach, the user needs knowledge about the problem. Furthermore, the designer may be interested to have alternative optimum solutions rather than one single solution. Consequently, the multi-objective optimization methods are considered that are able to optimize all the performance criteria simultaneously without the need to preselected weighting coefficients. In contrast to single-objective optimization with a single solution, in multi-objective optimization methods, a set of optimal solutions is provided which is known as Pareto front or Pareto optimal solutions [110–112]. The Pareto front includes solutions that are equally good, and none of the ones in the set dominates others with respect to all objective functions. In other words, considering all objective functions, none of them is better than others, and any improvement in one objective function degrades at least one other. Multi-objective optimization methodologies have been used for suspension design [110, 113–117]. A significant work is done by [110] where three important criteria are considered as the objective function including ride comfort, suspension travel, and road holding; the design variables are suspension stiffness and damping parameters. They employed a quarter-car model to study a system with constant and dual-rate passive suspension damper. They further examined simplified models with semi-active suspension systems. The problem is solved using Strength Pareto Evolutionary Algorithm. The multi-objective optimization strategy is also used for a suspension system including MR damper [118]. The optimization process is based on two performance objectives that are ride quality and thermal performance of the damper. That study involves the control algorithms, and the optimization is carried on to find the optimal control parameters. A multi-objective genetic algorithm (MOGA) is used to solve the problem.

For solving a multi-objective optimization problem, Evolutionary Algorithms (EAs) have been recognized to be a suitable method from the beginning of their developments [119]. Since EAs work with multiple individuals, they can search for multiple solutions simultaneously and take the advantages of all possible solutions [111, 119]. On the other hand, conventional optimization techniques, such as gradient-based methods, cannot deal with multiple solutions in parallel, so in practice, they reformulate the multi-objective problem as a single-objective problem prior to optimization [119]. EAs also can handle complex problems such as discontinuous or multi-modal problems; in fact, for multi-objective optimization EAs have distinct advantages compared to other strategies [119, 120]. Among the existing evolutionary algorithms, one of the most prominent algorithms is the non-dominated sorting genetic algorithm (NSGA-II) [111, 112, 120, 121]. This algorithm is one of the first EAs and has been used for solving many engineering multi-objective optimization problems [122, 123].

In the follow, the multi-objective optimization strategy is employed for the design of a suspension system equipped with a hybrid electromagnetic damper. Ride comfort, road holding, and regenerated power are considered as objective functions, and accordingly suspension and electromagnetic parameters are designed. The NSGA-II which is a well-known evolutionary algorithm is used for solving the problem, and a set of optimum solutions is derived.

4.1 System Modeling

Comparing to a conventional suspension, the hybrid design has the electromagnetic generator as an extra component. As the suspension system moves up and down, a repulsive force is produced by the electromagnetic generator. Furthermore, an AC voltage with a time varying frequency and amplitude is induced within the generator coils. This voltage cannot be directly connected to the energy storage unit (e.g battery), and special electronics are required to properly rectify and condition it before feeding into the battery. In order to model the functionality of the electromagnetic component, we adopted the model presented by Ribeiro et.al. [94]. They have utilized the lumped equivalent magnetic circuit

(LEMC) method to obtain:

$$L_c \frac{df_e}{dt} + (R_c + R_l) f_e = -{k_v}^2 \frac{dx}{dt} \tag{4.1}$$

In this model, x is the generator displacement, L_c is the coil inductance, k_v is the electromagnetic machine constant and R_c and R_l are the coil and load resistances. The external load includes the total apparent resistance of energy storage unit (e.g. battery), electrical rectification and conditioning circuitry. Based on equation 4.1, the conditioning circuitry can alter the force applied by the electromagnetic damper (f_e) by changing the apparent external load resistance (R_l). Generally, by increasing the R_l from zero to infinity, the f_e decreases from a maximum value to almost zero forces. With respect to the power generation, the maximum power can be obtained once the impedance of external load is equal to the internal impedance. It should be noted that, there is an energy loss associated with electrical rectification and conditioning circuitry that hasn't been taken into consideration in this study. In a vehicle application, it is possible for the driver to alternate the value of the R_l to realize different working modes for the suspension system, according to the road condition. In this study, however, for simplicity the value of the external load is set to the 30 percentage of the coil resistance (R_c). Based on the above model, the electromagnetic generator does not simply work like a conventional damper with a force proportional to the given velocity. This is because the produced electromagnetic force is altered by the inductance and inherent time delay of the component [124]. When the electromagnetic component acts as an active system, this issue can be addressed with proper controlling techniques such as using current amplifier, however, when working as a generator, it is harder to avoid this issue. Depending on the dimension of the coils, the magnitudes of R_c and L_c are defined. For the electromagnet generators that are designed for a vehicle suspension application, typically $\alpha = \frac{L_c}{R_c}$ has the order of magnitude of around 0.001 to 0.005. Here for simplifying the problem, we assume that $\alpha = \frac{L_c}{R_c} = 0.0025$.

4.1.1 Suspension Model

A quarter car model is used in this study for investigating the performance of the hybrid damper and also for optimization purposes. The electromagnetic component is integrated into a two degree of freedom quarter car model as shown in Figure 4.1.

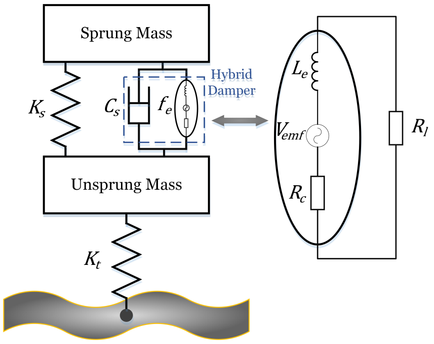

Figure 4.1: Schematic of a quarter car suspension system equipped with a hybrid electromagnetic damper.

The dynamic behavior of the hybrid suspension system is expressed by:

$$\begin{aligned} m_s\ddot{x}_s + k_s(x_s - x_u) + C_s(\dot{x}_s - \dot{x}_u) &= f_e \\ m_u\ddot{x}_u - k_s(x_s - x_u) - C_s(\dot{x}_s - \dot{x}_u)) + k_t(x_u - y) &= -\, f_e \\ L_c\dot{f}_e + (R_c + R_l)f_e &= -\, {k_v}^2(\dot{x}_s - \dot{x}_u)) \end{aligned} \tag{4.2}$$

where m_s is the sprung mass and m_u is the unsprung mass. Also k_s, k_t, and C_s represent suspension stiffness, tire stiffness, and hydraulic damping coefficient, respectively. L_c, R_c, R_l and k_v are the electromagnetic dampers parameters, and f_e is the electromagnetic damping force. Finally, x_s, x_u and y represent displacements of sprung and unsprung masses, and ground respectively. Rewriting equation 4.2 in the state space format yields:

$$\dot{X} = AX + By \tag{4.3}$$

where

$$X^T = [x_1, x_2, x_3, x_4, x_5] = [x_s, \dot{x}_s, x_u, \dot{x}_u, f_e] \tag{4.4}$$

and

$$A = \begin{bmatrix} 0 & 1 & 0 & 0 & 0 \\ -\frac{k_s}{m_s} & -\frac{c_s}{m_s} & \frac{k_s}{m_s} & \frac{c_s}{m_s} & \frac{1}{m_s} \\ 0 & 0 & 0 & 1 & 0 \\ \frac{k_s}{m_u} & \frac{c_s}{m_u} & -\frac{k_s+k_t}{m_u} & -\frac{c_s}{m_u} & -\frac{1}{m_u} \\ 0 & -\frac{{k_v}^2}{L} & 0 & \frac{{k_v}^2}{L} & -\frac{R_t}{L} \end{bmatrix}$$

$$B = \begin{bmatrix} 0 \\ 0 \\ 0 \\ \frac{k_t}{m_u} \\ 0 \end{bmatrix} \tag{4.5}$$

in which $R_t = R_c + R_l$. In this study, the analyses are carried out in frequency domain. In the following, we present the details of road modeling and objective function calculations in frequency domain.

4.1.2 Road Modeling

The road roughness is modeled as a stationary Gaussian stochastic process of a given displacement power spectral density (PSD) in $m^2/(cycle/m)$ [125]:

$$S_{PSD}(v) = \frac{s_0 v^{\beta}}{{v_0}^{\beta}} = G_r v^{\beta} \left[\frac{m^3}{cycle}\right] (6) \tag{4.6}$$

In this equation, v represents the spatial frequency and $v_0 = \frac{1}{2\pi}$ $[cycle/m]$ represents the reference spatial frequency. Also S_0 is the displacement PSD at v_0, $G_r = S_0/(v_0^{\beta})$ is the road-roughness coefficient, and the value of β is usually approximated as -2. Based on the road classification of international standard organization (ISO), the values of S_0 mean for a class C (average) road is 64×10^{-6}.

For a vehicle speed of V, the power spectral density of road excitation in terms of temporal frequency ($\omega = 2\pi V v$) is obtained as [126]:

$$S_{PSD}(\omega) = \frac{2\pi G_r V}{\omega^2 + {\omega_0}^2} \tag{4.7}$$

In order to constraint the displacement value to be finite at very small frequencies, a small cut-off frequency ω_0 is defined and added to the equation. Based on equation (4.7), the road displacement input to the system can be stated as a unit-intensity white noise signal passing through a low-pass filter of the form:

$$G(s) = \sqrt{\frac{2\pi G_r V}{s + \omega_0}} \tag{4.8}$$

This first order filter shows that for very small ω_0, the ground velocity input $\dot{x}_0$ is a white noise with intensity of $2\pi G_r V$ [126].

4.2 Multi-Objective Optimization of the Vehicle Suspension System

There are different objective functions available in the literature to optimize the hybrid design and compare its performance with other systems, among which ride comfort, road holding and regenerated power are utilized in this study. The first two ones are known as the most common criteria for optimization purposes. Additionally, the regenerated power is chosen to be the third criterion as it is the main motivation for the new hybrid design. Based on the linear system theory, when the input is a white noise (equation (4.8)), the RMS values of a systems responses are obtained from H2 norm. Using this concept, the RMS values of the selected objective functions are calculated as:

$$\sigma = \left\|H\right\|_2 = \left[\frac{1}{2\pi}\int_{-\infty}^{\infty} trace\left(H^*(j\omega)H(j\omega)\right)d\omega\right]^{\frac{1}{2}} \tag{4.9}$$

in which, H is the transfer function of the desired output (i.e. objective function) when unit white noise is applied as input.

4.2.1 Ride Comfort

Ride comfort refers to human perception inside a moving vehicle. This perception is directly related to the level of cabin's vibration, mostly generated by road surface irregularities and transferred through the suspension system. Human perception, and consequently ride comfort, depends on the characteristics of the applied vibration such as magnitude, frequency, direction, and location. According to ISO 2631 standard, the effect of vibration on human can be evaluated by weighting the RMS values of accelerations with human vibration-sensitivity curves (ISO 2631-1 [127]). To imply the weighting for vertical vibrations, a low order filter is proposed in reference [128] as:

$$W_{2631} = \frac{80.03s^2 + 989s + 0.02108}{s^3 + 78.92s^2 + 2412s + 5614} \tag{4.10}$$

For the quarter car model, the RMS of sprung mass acceleration, weighted by W_{2631}, indicates the ride comfort quality for the vehicle [126].

$$\begin{aligned} f_1 =& \sigma_{\ddot{x}_s} \\ \sigma_{\ddot{x}_s} =& \left[\frac{1}{2\pi} \int_{-\infty}^{\infty} 2\pi G_r V \left| W_{2631} \frac{\ddot{x}_s}{\dot{y}} \right|^2 d\omega \right]^{\frac{1}{2}} \end{aligned} \tag{4.11}$$

4.2.2 Road Holding

Road holding is the contact force between the vehicle wheel and the ground. In a poorly designed system, at a severe vibration condition, the contact force may be too low or even the wheel may lose its contact with the ground. In this condition, the vehicle may not be properly controlled during steering, accelerating, and braking. This shows that the contact force between wheels and ground, called road holding, affects the handling and performance of the vehicle, and thus is an important criterion for suspension system design. This criterion is defined as the ratio of the dynamic force to the static force between tire and ground represented by:

$$\eta_{D/S} = \frac{k_t(x_u - y)}{(m_s + m_u)g} \tag{4.12}$$

where a ratio equal to or more than 1 indicates the loss of contact between the wheel and the ground. The RMS value of this ratio is considered as criterion for evaluating the road holding quality of the suspension system:

$$\begin{aligned} f_2 =& \frac{k_t}{(m_s + m_u)g} \sigma_{x_1 - y} \\ \sigma_{x_1 - y} =& \left[\frac{1}{2\pi} \int_{-\infty}^{\infty} 2\pi G_r V \left| \frac{x_u - y}{\dot{y}} \right|^2 d\omega \right]^{\frac{1}{2}} \end{aligned} \tag{4.13}$$

4.2.3 Power Regeneration

With the integration of an electromagnetic generator into the suspension system, a portion of the vibration energy is converted into useful electrical power. The regenerated electrical power (P) can be calculated using:

$$P = R_l I^2 \tag{4.14}$$

where R_l and I are the external resistance and current of the generator coils. According to the method of lumped equivalent magnetic circuit, the current (I) is obtained by:

$$I = \frac{f_e}{k_v} \tag{4.15}$$

The RMS value for the ratio of the regenerated power to the input velocity $({f_3}')$ is given by:

$$\begin{aligned} \sigma_{f_e} =& \left[\frac{1}{2\pi} \int_{-\infty}^{\infty} 2\pi G_r V \left| \frac{f_e}{\dot{y}} \right|^2 d\omega \right]^{\frac{1}{2}} \\ {f_3}' =& R_l \left(\frac{\sigma_{f_e}}{k_v} \right)^2 \end{aligned} \tag{4.16}$$

Unlike the first two objective functions (f_1 and f_2), the regenerated power needs to be maximized, thus we take the negative of the ${f_3}'$ as the third objective function.

$$f_3 = -{f_3}' \tag{4.17}$$

The analytical solution for $\sigma_{\ddot{x}_s}$, $\sigma_{x_1 - y}$ and σ_{f_e} can be calculated using the formulas given in the appendix A.

4.2.4 Multi-objective Optimization Problem

As mentioned before, for this study, three criteria are selected for optimization and evaluation of the hybrid suspension design. Also four parameters from the suspension system are considered as design variables, including suspension spring stiffness (k_s), hydraulic damper coefficient (c_s), and two parameters from electromagnetic generator (R_c, k_v). Then, the problem is defined as:

$$\begin{aligned} min\ F(v) &= [f_1(v), f_2(v), f_3(v)] \\ v &= (k_s, c_s, R_c, k_v) \end{aligned} \tag{4.18}$$

By applying the multi-objective GA algorithm NSGA-II to the above problem, a set of optimal solutions (a Pareto front) is obtained for suspension system design.

4.3 Simulation Results

To evaluate the performance of the optimized designs, they are compared with a conventional suspension system and a not-optimized hybrid suspension system. Parameters of the conventional suspension system are adopted from a typical passenger car. From literature [126], these parameters include sprung mass $m_s = 362.7\ kg$, unsprung mass $m_u = 40\ kg$, tire stiffness $k_t = 182087\ N/m$, suspension stiffness $k_s = 20053\ N/m$, and suspension damping coefficient $c_s = 1388\ Ns/m$. For the not-optimized hybrid suspension system, the parameters are purposefully selected such that this system shows similar dynamic responses to the conventional one while recovering a portion of the vibration energy into useful electrical power. For the road modeling purposes, in this study, the average road (class C) category is selected where the road roughness coefficient is $G_r = 64 \times 10^{-7}$ based on the ISO standards.

4.3.1 Pareto Front

The lower and upper bounds (lb, and ub, respectively) for the design variables of this problem are selected as $lb = [4000, 100, 4, 18]$ and $ub = [30000, 3000, 50, 300]$.

For the three objective functions, a three-dimensional Pareto front is obtained, shown in Figure 4.2. The projections of this Pareto set are illustrated in Figures 4.3, 4.4, and 4.5. In Figure 4.3 ride comfort is demonstrated versus road holding. As can be seen, this plot includes a minimum (road holding) point. For the points before this point, the objective functions of ride comfort and road holding change conversely, meaning that better ride comfort results in worse road holding and vice versa. For the points after the minimum point, however, both of the ride comfort and road holding objective functions change in the same direction (i.e. both increase as we move forward to the right hand sided points). These right hand sided points exhibits the highest rates of regenerated power which can be recognized from Figure 4.4, where inverse of power versus ride comfort is reflected. Therefore, considering the third objective function, the right hand sided points in Figure 4.3 are also non-dominated. Figure 4.4 shows that the ride comfort and the regenerated power change in opposite manner. Better ride comfort results in less regenerated power and more regenerated power exacerbates quality of ride. Figure 4.5 shows that the best designs, in terms of road holding, are also able to regenerate more power, meaning that these two criteria are accordant to each other. In this plot a huge number of points gathered in the same location. This location represents the best values for road holding and regenerated power objective functions.

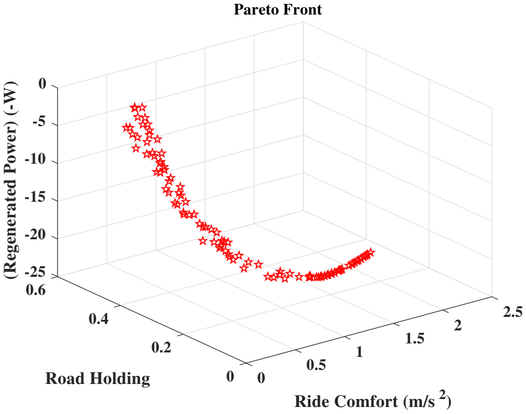

Figure 4.2: 3D Pareto front obtained from the multi-objective GA (ride comfort vs road holding vs negative of regenerated power).

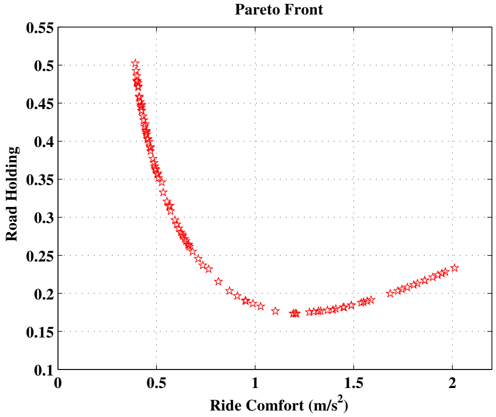

Figure 4.3: 2D Pareto front obtained from the multi-objective GA (road holding vs ride comfort).

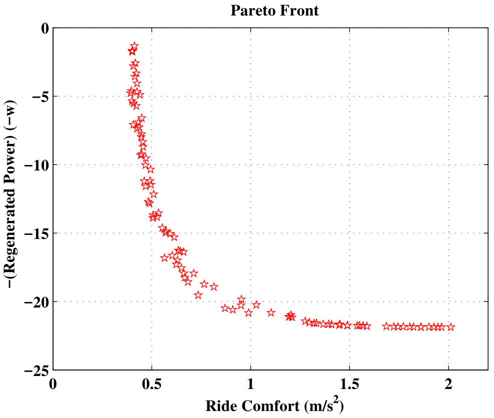

Figure 4.4: Pareto front obtained from the multi-objective GA (negative of regenerated power vs ride comfort).

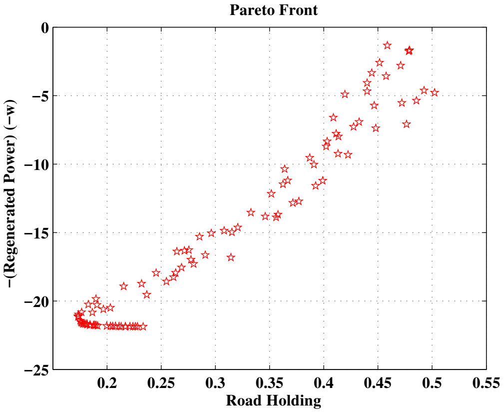

Figure 4.5: Pareto front obtained from the multi-objective GA (negative of regenerated power vs road holding).

4.3.2 Selected Designs

The Pareto front provides a big set of solutions to choose from, among which an optimal case is selected and compared with the conventional suspension system and the not-optimized hybrid system. This optimal case (named case 1) is selected, from the Pareto front, to have the best overall performance with respect to all design criteria. In other words, this overall-optimized design has better ride comfort and road holding, and also generates more power, comparing to the conventional and not-optimized systems. The design variables and corresponding performance indexes of these models are listed in Table 4.1.

Table 4.1: Design parameters and performance indexes of conventional, not-optimized hybrid and overall-optimized hybrid systems.

Design Type	Ride Comfort	Road Holding	-Power	k_s	c_s	R_c	k_v
Conventional system	1.0138	0.1916	-	20053	1388	-	-
Not-optimized	1.0172	0.1903	-6.9599	20053	955.3	10	75
Overall-optimized (Case 1)	**0.9947**	**0.1847**	**-19.643**	9808.5	189.7	23.12	197.55

The RMS values of objective functions, in frequency domain, are calculated and plotted for different vehicles speeds to evaluate the performance of the overall-optimized hybrid system. Figures 4.6, 4.7 and 4.8 depicts the evaluated values for ride comfort, road holding, and regenerated power objective functions, respectively.

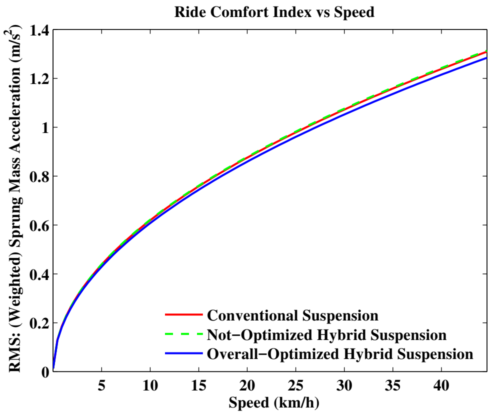

Figure 4.6: Ride comfort analysis over vehicle speeds on an average road.

Figure 4.6 indicates that the overall-optimized system has better ride comfort than the others; although, the improvement in ride comfort is not too much. Also according to Figure 4.7, the overall-optimized system can improve the road holding quality of the vehicle. The RMS of regenerated power for these three types of damper is illustrated in Figure 4.8. The evaluated regenerated power is proportional to vehicles speed, and is considerably improved for the overall-optimized system. Based on this plot, the regenerated power of this optimized case (case 1) is about three times more than that of the not-optimized system. In addition to the first chosen overall-optimized design, described above, we can consider criterion priority when picking a solution from the Pareto front set. This means

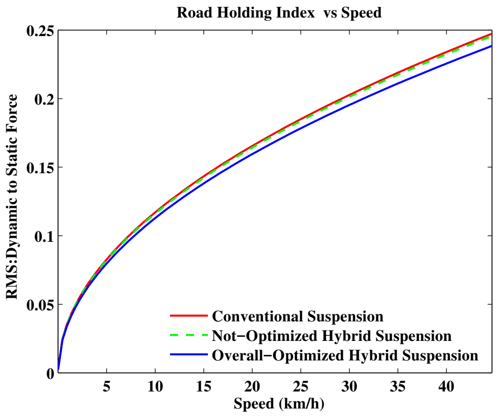

Figure 4.7: Road holding analysis over vehicle speeds on an average road.

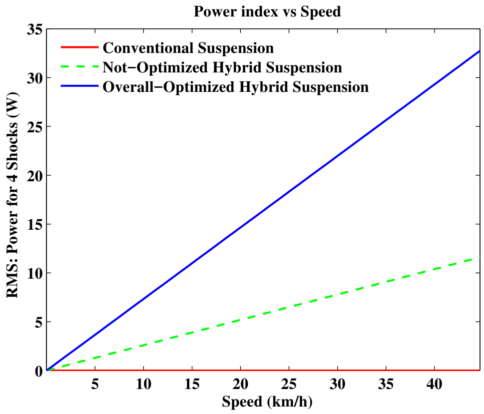

Figure 4.8: Power regeneration analysis over vehicle speeds on an average road.

that depending on needs and conditions, other optimal cases can be chosen from the set of optimal solutions. For example, if required, the designers have the option to select a solution with considerably better ride comfort while other criteria are still acceptable. In Table 4.2, some other optimized cases with different criterion priority are listed.

4.3.3 Bode Plots

For more investigation and understanding the performance differences between the selected optimal cases, Bode plots are employed to compare the first and second optimized cases (from Table 4.2) with the conventional and the not-optimized suspension system. For each

Table 4.2: Design parameters and performance indexes of different optimized hybrid cases.

Design Type	Ride Comfort	Road Holding	-Power	k_s	c_s	R_c	K_v
Case1: Without Priority	**0.9947**	**0.1847**	**-19.643**	9808.5	189.7	23.12	197.55
Case 2: Ride Priority	**0.8060**	0.2189	-15.563	9161.1	282.9	31.60	161.61
Case 3: Road Holding Priority	1.1758	**0.1737**	-20.851	13684.9	154.9	12.71	180.81
Case 4: Power Priority	1.2902	0.1740	**-21.196**	14032.8	147.2	13.28	207.20

system, the Bode plots of transfer functions $Z_1 = \frac{\ddot{X}_s}{Y}$, $Z_2 = \frac{X_u - Y}{Y}$ and $Z_3 = \frac{\sqrt{P}}{Y} = \frac{\sqrt{R_l}}{k_v}\frac{F_e}{Y}$ are calculated to compare the performances of suspension systems with respect to ride comfort, road holding and regenerated power, respectively. The resulting diagrams are shown in Figures 4.9, 4.10 and 4.11. The not-optimized hybrid suspension system delivers similar ride comfort and road holding performance to the conventional one, but it also regenerates some amount of power. Comparing to these two suspension systems, it can be seen in Figures 4.9 that ride comfort quality of both of the overall-optimized hybrid suspension (case 1) and the comfort-optimized hybrid suspension (case 2) are improved; although the improvement for case 2 is more considerable. Figure 4.10 shows the same improvement in road holding quality for case 1, while for case 2, road holding at some frequencies is worse than other systems. Figure 4.11 demonstrates that for both optimal cases (1 and 2) the magnitude of the regenerated power is increased, comparing to the not-optimized hybrid design. The regenerated power of the second optimal case is less than the first case; however, it is still more than that of the not-optimized hybrid suspension system. It should be noted that according to definitions of the Society of Automotive Engineers, for the design of a vehicle suspension system, usually vibration frequencies of less than 25 Hz are considered [129].

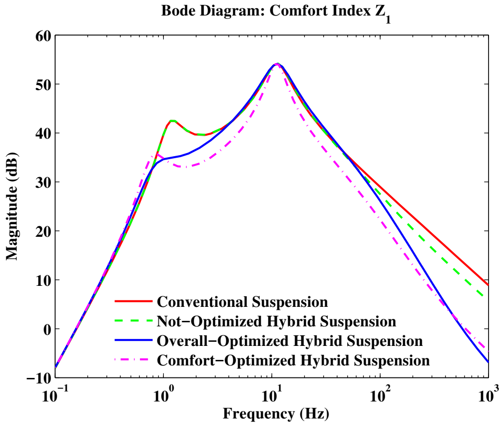

Figure 4.9: Frequency analysis (Bode plot) of ride comfort on an average road.

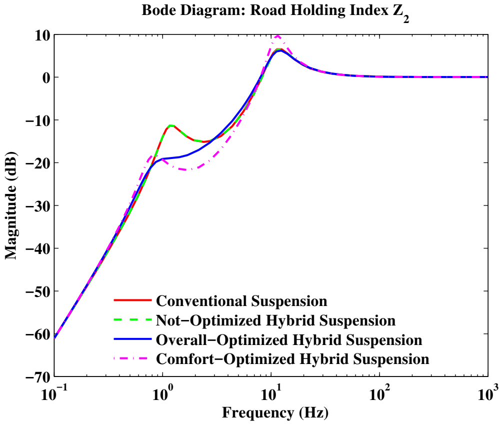

Figure 4.10: Frequency analysis (Bode plot) of road holding on an average road.

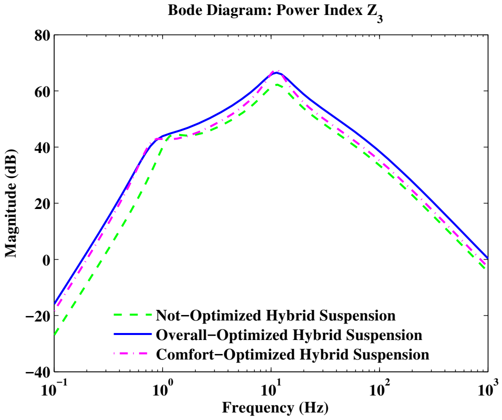

Figure 4.11: Frequency analysis (Bode plot) of regenerated power on an average road.

4.3.4 Time Domain Results

To better describe the time domain performance of the above four suspension systems (conventional, not-optimized hybrid, overall-optimized hybrid, and comfort-optimized hybrid suspension systems), they are excited by a haversine type bump with the height of 10 centimeter and length of 1 meter. The simulation is done at the vehicle speed of 96.56 km/h (60 mph). The results of the haversine bump passing simulation are shown in Figure 4.12, 4.13, and 4.14. The not-optimized hybrid design has almost identical behavior to the conventional one but it is also able to produce about 124 joules of energy by passing over the bump. Comparing to these two systems, the overall-optimized design (case 1) has lower rates of sprung mass acceleration. According to Figure 4.13, the dynamic to static force (road holding index) of the overall-optimized system has the same peak value which is around -1. With respect to settling time, again the overall-optimized system shows a better performance. The summation of the power for the overall-optimized system in Figure 4.14 equals to 361 joules which is 2.9 times the power generated by the not-optimized system. The comfort-optimized design (case 2) has, by far, the best ride comfort quality among all these systems, however, its settling time and regenerated power (194 joules) are worse than the overall-optimized design (case 1).

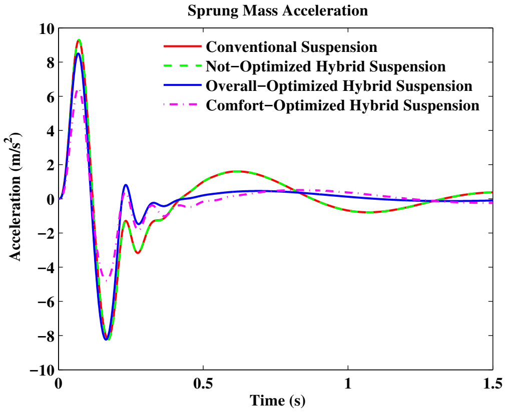

Figure 4.12: Sprung mass acceleration during the ride over a haversine bump.

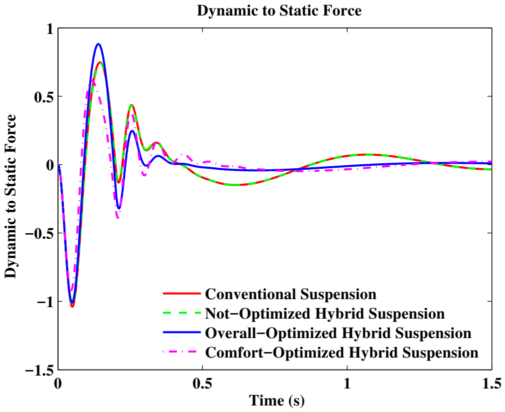

Figure 4.13: Dynamic to static force during the ride over a haversine bump.

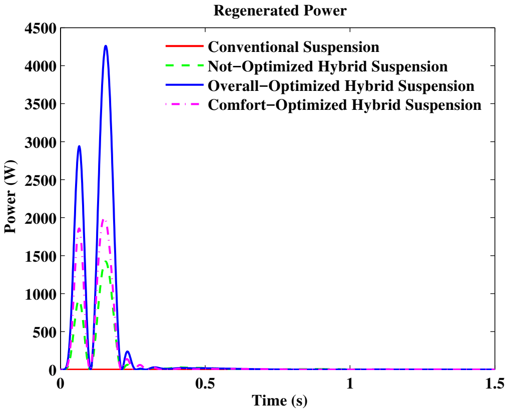

Figure 4.14: Regenerated power during the ride over a haversine bump.

According to the results presented in this chapter, the overall-optimized suspension system delivered better ride comfort and road holding quality, compared to the conventional and not-optimized hybrid design, and is also able to regenerate higher rates of electrical energy compared to the not-optimized regenerative suspension model.

Chapter 5

Active Hybrid Electromagnetic Vibration Isolator: Design, Modelling, and Optimization

This chapter presents the design, modeling, and optimization of a new active hybrid electromagnetic vibration isolator that is developed based on the conceptual design presented in Section 1.2.2. The design of the electromagnetic component of the hybrid actuator is an important part of the present work as it is responsible for active force generation. This component is further required to provide a contactless magnetic stiffness for the device. These two goals are achieved by incorporating electromagnetic coil and magnet in each stack. A multitude of configurations are designed and evaluated for the best possible performance, among which, the design, modeling and optimization of the selected configuration are presented.

5.1 Principle of Magnetic Flux Density and Force Modeling

In order to model the magnetic flux density and electromagnetic forces, the works done by Derby and Olbert [130], and Robertson et. al. [131] can be used, respectively. In the follow, these models are briefly presented.

Consider two cylindrical electromagnetic units, with radiuses R_1 and R_2, and heights

h_1 and h_2, that are located in a vertical arrangement, as shown in Figure 5.1. Each of the units can be either a magnet or a thin coil.

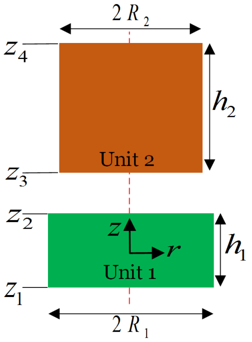

Figure 5.1: Schematic view of two cylindrical electromagnetic units in a vertical arrangement, each unit can be either a solid magnet or a thin coil.

The produced magnetic field by unit 1, at any location (r,z) is given by:

$$B_r = B_0 \left(\alpha_+ C\left(k_+, 1, 1, -1, \right) - \alpha_- C\left(k_-, 1, 1, -1, \right)\right) \tag{5.1}$$

and

$$B_z = \frac{B_0}{a + r} \left(\beta_+ C\left(k_+, \gamma^2, 1, \gamma, \right) - \beta_- C\left(k_-, \gamma^2, 1, \gamma, \right)\right) \tag{5.2}$$

with

$$B_0 = \begin{cases} \frac{B_{rem}}{\pi}, & magnet \\ \frac{\mu_0 N I}{(h_1)\pi}, & thin\ coil \end{cases} \tag{5.3}$$

$$z_\pm = z \pm \frac{h_1}{2} \tag{5.4}$$

$$\alpha_\pm = \frac{R_1}{\sqrt{{z_\pm}^2 + (r + R_1)^2}} \tag{5.5}$$

$$\beta_\pm = \frac{z_\pm}{\sqrt{{z_\pm}^2 + (r + R_1)^2}} \tag{5.6}$$

$$\gamma = \frac{R_1 - r}{R_1 + r} \tag{5.7}$$

$$k_{\pm} = \frac{\sqrt{{z_{\pm}}^2 + \left(R_1 - r\right)^2}}{\sqrt{{z_{\pm}}^2 + \left(R_1 + r\right)^2}} \tag{5.8}$$

where B_{rem} is remnant magnetic flux density of magnet, and C represents the generalized complete elliptic integral, given by:

$$\begin{aligned} &C\left(k_c, p, c, s\right) = \\ &\int_0^{\pi/2} \frac{c\,\cos^2\!\phi + s\,\sin^2\!\phi}{\left(\cos^2\!\phi + p\,\sin^2\!\phi\right)\sqrt{\cos^2\!\phi + {k_c}^2\,\sin^2\!\phi}} d\phi \end{aligned} \tag{5.9}$$

where the values of C can be obtained by utilizing the code written by Derby and S. Olbert [130].

The electromagnetic force (F_e) between the two units, in vertical direction, is:

$$F_e = \frac{J_1 J_2}{4\mu_0} \sum_{k_1=1}^{2} \sum_{k_2=3}^{4} d_1 d_2 d_3 f_e (-1)^{k_1+k_2} \tag{5.10}$$

where

$$J_i = \begin{cases} B_{rem},\ \mathit{magnet} \\ \frac{\mu_0 N I}{h_i},\ \mathit{thin\ coil} \end{cases} \quad i = 1, 2 \tag{5.11}$$

in which $\mu_0 = 4\pi \times 10^{-7}$, and N and I are the coil number of turns and current, respectively. The rest of parameters in equation (13) are defined as follows:

$$f_e = K(d_4) - \frac{1}{d_2} E(d_4) + \left(\frac{d_1^2}{d_3^2} - 1\right) \Pi \left(\frac{d_4}{1 - d_2} | d_4\right) \tag{5.12}$$

with

$$d_1 = x_{k_1} - x_{k_2} \tag{5.13}$$

$$d_2 = \frac{\left(R_1 - R_2\right)^2}{d_1^2} + 1 \tag{5.14}$$

$$d_3^2 = (R_1 + R_2)^2 + d_1^2 \tag{5.15}$$

$$d_4 = \frac{4 R_1 R_2}{d_3^2}, \quad 0 < d_4 < 1 \tag{5.16}$$

where $K(p)$, $E(p)$, and $\Pi(p|q)$ are the complete first, second and third kind of elliptical integrals, respectively.

The above equations are developed for solid magnets and thin coils, however, the employed methods can be slightly modified to incorporate ring-shape magnets and thick coils. A ring-shape magnet, with magnetization B_{rem}, and outer and inner radiuses r_{1o} and r_{1i}, respectively, can be modeled as summation of two solid magnets: one with radius r_{1o} and magnetization B_{rem}, and one with radius r_{1i} and magnetization $-B_{rem}$. In case of having a thick coil in the system, the unit can be modeled as summation of a number of concentric thin coils.

5.1.1 Stack Design and Optimization

Figure 5.2a schematically illustrates the configuration 1 for stack's design with the adopted nomenclature. This configuration includes a ring-shape vertically magnetized magnet, surrounded by a cylindrical coil.

The total magnetic flux density in radial (B_r) and vertical (B_z) directions at any point is the superposition of magnetic flux densities due to magnets M1 and M2, and coils C1 and C2, as:

$$\begin{aligned} B_r &= B_{r_{M1}} + B_{r_{C1}} + B_{r_{M2}} + B_{r_{C2}} \\ B_z &= B_{z_{M1}} + B_{z_{C1}} + B_{z_{M2}} + B_{z_{C2}} \end{aligned} \tag{5.17}$$

and the total electromagnetic force from the bottom to top stack is given by:

$$F_e = F_{e_{M1,M2}} + F_{e_{M1,C1}} + F_{e_{C1,M2}} + F_{e_{C1,C2}} \tag{5.18}$$

where $F_{e_{i,j}}$ represents the force applied from j to j.

In a zero current state, the top stack will rest at a distance, above the bottom one, such that the electromagnetic force between the top and bottom magnets equals the load masses. Therefore the base stiffness of the actuator merely depends on the magnets' configuration. Once a current is supplied to the top and bottom coils, due to the interaction of coils and magnets, a variation in the electromagnetic force will happen, providing the actuation force. Therefore, this force variation depends on the magnet/coils configuration as well as the applied current.

The two main metrics for optimizing the design are zero-current force, and force variation at a constant stacks distance. Zero-current force represents the electromagnetic force

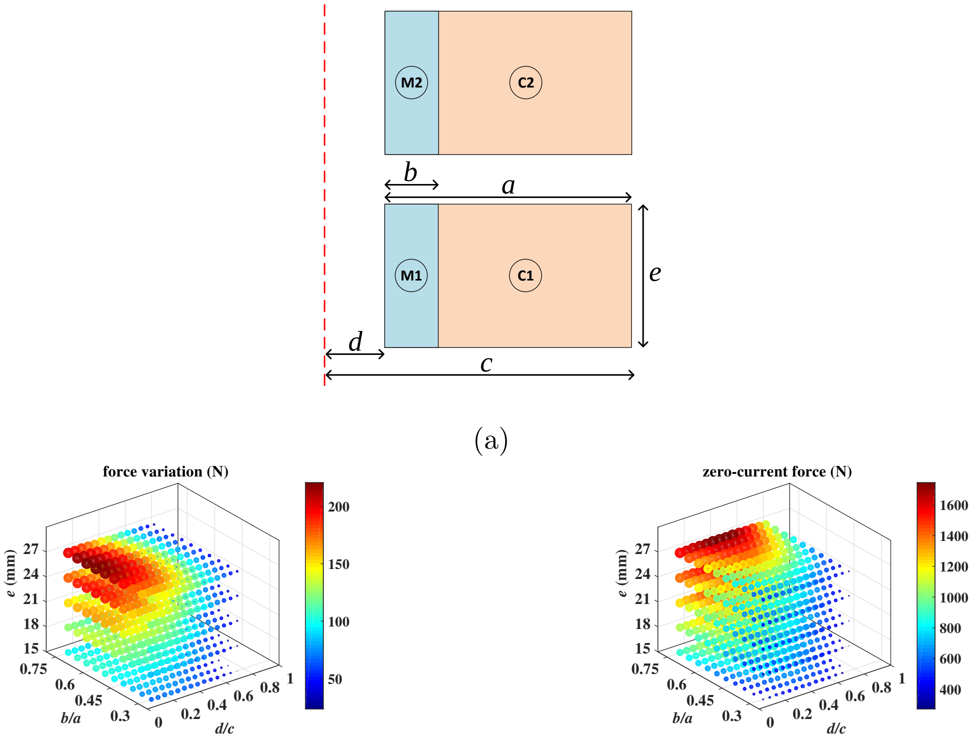

(a)

(b)

(c)

Figure 5.2: Stack design: configuration 1, a: the cylindrical design including a magnet M and a coil C in each stack (red dash line represents the axisymmetry axis), b: force variation, and c: zero-current force.

when coil currents are zero, and force variation is the difference between the electromagnetic force when the coil currents are maximum and minimum. The objectives of the design optimization are to reach a nominal static load of 600 N, and to maximize the force variation. According to the nomenclature represented in Figure 5.2a, the three optimization variable are $0 < b/a < 1$, $0 < d/c < 1$, and $0\ (mm) < e \leq 27\ (mm)$, where $c = 60\ mm$ is the constant parameter.

Figure 5.2b depicts the obtained analytical results for force variation. According to this figure, the optimum value for b/a variable is ~ 0.6. Furthermore, higher force variation is archived if higher e or lower d/c are chosen. The analytical results for zero-current force are shown in Figure 5.2c. One interesting finding is that zero-current force is maximized when the d/c is bigger than zero ($\sim$ 0.4). This means that two ring-shape magnets, despite having less volume, would have higher attraction/repulsion forces comparing with two solid circular magnets with similar outer diameter. Also, as expected, zero-current force will increase as b/a and e variables increase. Based on these findings, and by focusing on the force variation metric, the optimization variables b/a, and e are set to 0.6 and 25 mm respectively. The other variable is set to $d/c = 1/12$, slightly bigger than zero to make space for a guiding shaft and bushing. Considering the obtained zero-current forces, the optimized configuration 1 has a force far larger than the target, which results in a small ratio for the force variation to the zero-current force ratio. Therefore it is desired to reduce the magnitude of zero-current force, while maintaining the obtained force variation. For this purpose, configuration 2, shown in Figure 5.3a, is proposed in which the upper section of the magnet is replaced by an iron of length f. In order to optimize the modified configuration 2 for finding the optimal value of f/e, a new model is developed using finite element method (FEM). The details of FEM modeling will be further explained later in this section.

Figure 5.3b illustrates the magnitudes of zero-current force and force variation for different f/e values. As it can be observed, as f/e increases, zero-current force drops significantly, while force variation decrease only very slightly. Therefore, the iron thickness can be selected to address different levels of zero-forces, according to the external load masses. Based on the target for zero-current force, f/e is set equals to 0.105. It should be noted that the optimization results, presented in this section, are preliminary, and required to be further adjusted according to the final hybrid design, manufacturing constraints, and availability of the parts in the market.

The final design for the proposed active electromagnetic actuator is presented in Figure 5.4. In this figure, a half section view of an actuator with two stacks is shown. In each stack, three smaller magnets (available in the market) are used that together make a bigger magnet with the height selected in the optimization process. As it can be seen, comparing

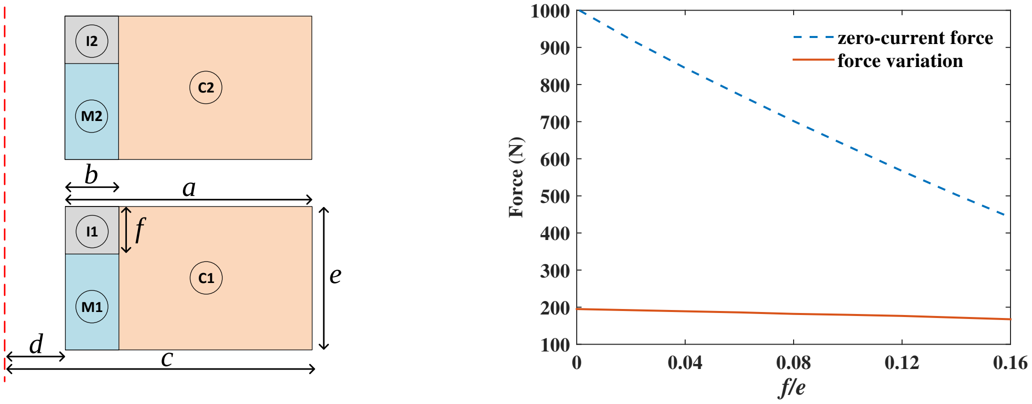

(a) (b)

Figure 5.3: Stack design: configuration 2, a: the cylindrical design includes a magnet M, a coil C, and an iron I in each stack (red dash line represents the axisymmetry axis), and b: Effect of iron thickness on the force variation and the zero-current force.

to the configuration 2, new iron parts are added above the top stack, lower the bottom stack, and also around the coils. The additional iron parts, helps to increase the force variation by ∼ 15%. They further, close the magnetic flux, avoiding flux leakage and eddy current problems. The shape and dimensions of the iron parts are selected to fit inside the hybrid isolator, presented in Section 5.2.

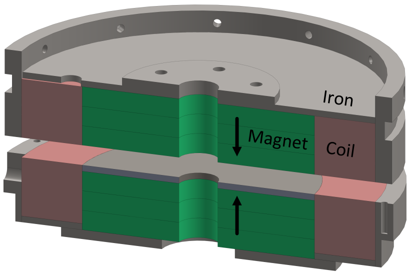

Figure 5.4: Final design for active electromagnetic actuator (half section view).

An updated FEM 2D axisymmetric model is developed in COMSOL® multiphysics (Version 5.2) to match the final design of active electromagnetic actuator. In this model, the remnant magnetic flux density of magnets is $B_{rem} = 1.3\ T$, and the coils wire size, according to American Wire Gauge standard system, is $AWG = 28$. Figure 5.5 represents the FEM results for norm values of magnetic flux density (color map) together with the magnetic flux directions (white arrows) at different locations. Using this FEM model, Figure 5.6 is produced which predicts the electromagnetic force (F_e) between the two stacks at different distances (3 to 10.5 mm) and applied currents (-2.5 to 2.5 A). This figure provides many useful information about the performance of the active electromagnetic actuator. For instance, the horizontal line l_{12} (between points p_1 and p_2) indicates that the actuator can move a heavy load mass of 61.16 kg (600 N) within a range of 3.5 mm by only changing current from -1 to 1 A. In another example, the vertical line l_{34} (between points p_3 and p_4) shows that at a fixed distance of 4 mm, a force variation of 155.5 N is achieved, again, by changing current from -1 to 1 A.

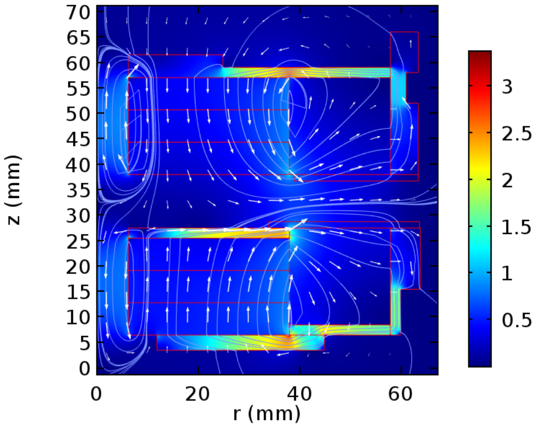

Figure 5.5: FEM modeling of electromagnetic actuator, norm and direction of magnetic flux densities are presented by color map and arrows, respectively.

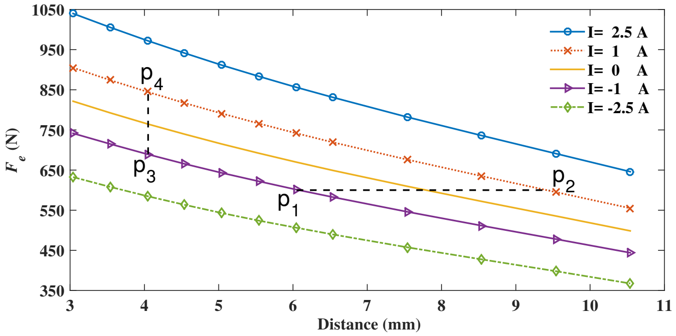

Figure 5.6: Electromagnetic actuator force at different distances and applied currents.

In order to ensure that the results of the FEM model are accurate, similar steps to the ones explained in section 2.2.2 are taken. Table 5.1 presents the details of the COMSOL FEM model of the active electromagnetic component.

Table 5.1: Details of COMSOL FEM model of the active electromagnetic component.

Mesh Type	Mesh Maximum Size	Boundary Condition	Termination Relative Tolerance
triangular	iron, magnet and coil: 0.2 [mm], other: 4 [mm]	magnetic insulation	1e-4

As previously stated, one of the main goals of this work is to propose a new active actuator with a large force density. In order to have a better analysis of the electromagnetic actuator, its force variation is compared with an optimized voice coil presented by Okyay et. al. [1]. An FEM model of the voice coil is developed in COMSOL® multiphysics (Version 5.2), and further, for a fair comparison, the model is scaled up to have relatively similar height and diameter as our actuator. Additional, optimization is also performed to slightly increase the voice coil performance. Table 5.2 lists the force variation produced by the scaled voice coil (when the coil is completely inside the iron yoke and has the maximum possible force), and the proposed actuator at different stack distances. As it is shown in the table, the proposed actuator has a considerable higher force variation. This higher force variation would result in the design of lighter actuators. The proposed electromagnetic actuator is $\sim 25\%$ lighter than of a voice coil with the same 310 N force variation at ± 2 A applied currents. It should be further mentioned that, voice coil has a zero force at zero current, while the proposed actuator has a biased force at zero current that is due to its magnetic spring. This feature, in the proposed actuator, eliminates the need for employing spiral springs to support dead loads.

Table 5.2: Comparison of the proposed active electromagnetic actuator with voice coil (scaled) presented in [1].

Actuator	**Force variation** (N)		
	$I = \pm 1$ A	$I = \pm 2$ A	$I = \pm 2.5$ A
Voice coil [1] (scaled)	136.8	256.5	308.9
Proposed, distance=3.5 mm	159	318	397.5
Proposed, distance=4 mm	155.5	310	387.5
Proposed, distance=4.5 mm	151.5	303	378

5.2 Integration of Pneumatic Spring into the Hybrid Vibration Isolator

In this section, the previously proposed active electromagnetic actuator is combined with a pneumatic spring to make a hybrid device. The proposed hybrid device is presented in Figure 5.7. In this figure, materials are color coded, where black, blue, grey, yellow, brown, green and cyan colors represent rubber, aluminum, iron (steel), nylon polymer, copper, magnet and titanium parts, respectively.

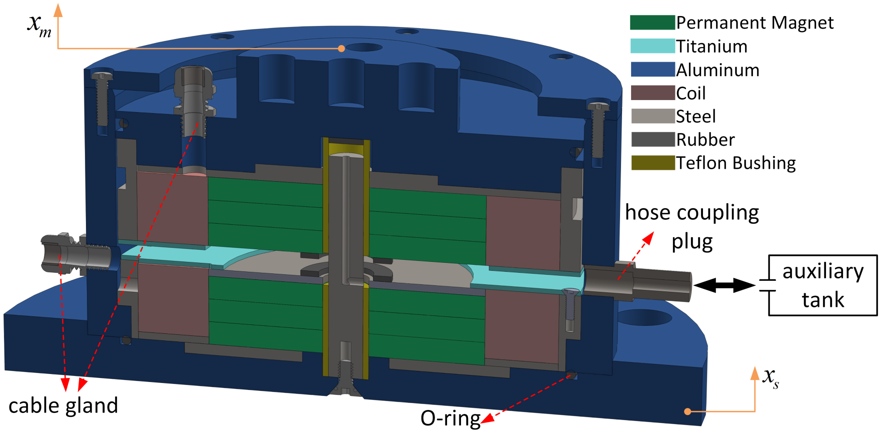

Figure 5.7: Electromagnetic-pneumatic hybrid actuator: the half section view of the final design.

The bottom stack is mounted on a base inside an aluminum shell, while the top stack is floated above the bottom stack. To ensure a pure vertical motion for the top stack a small shaft (with bushing) is used in the center of the device. To secure the coils inside the stacks, two titanium disks are employed. Titanium is a non-magnetic metal, and thus coils will not be shielded, and furthermore, due to the low conductivity, there will be no eddy current damping problem. The pneumatic spring includes the pressurized air filling the gap between the two stacks, and being connected to an auxiliary tank using a hose. Owning to the large area of the stacks, with only a air pressure of 5-10 *psi*, the nominal mass can be considerably increased. The reciprocating motion of the top stack is sealed using a nitrile o-ring. Furthermore, two cable glands are used to seal the outgoing cables of the coils. The dimensions of some parts are considered bigger than the requirement for the prototyping stage, and thus, can be significantly reduced for a commercialization implementation. For instance, for the low range of air pressure in the pneumatic spring, a much thinner shell can be used.

5.3 Force Modeling

The dynamics of electromagnetic and pneumatic components are relatively complex, making their modeling a challenging task. Implementation of complicated models (such as FEM models for electromagnetic component) is not practical for real time control applications. Therefore, simple yet accurate models are required to capture the main features of the components with a minimum computation load. This section discusses and presents mathematical models for both electromagnetic and pneumatic components.

The total vibration isolation force is given by:

$$F = F_e(z, I) + F_p(x) + F_r(x, \dot{x}) \tag{5.19}$$

where $F_e(z, I)$ and $F_p(x)$ are the force contributions of electromagnetic and pneumatic components, respectively, and $F_r(x, \dot{x})$ is the friction force. I is the applied current to the coils, $x = x_m - x_s$ is the relative displacement of top to bottom stacks, and $z = x + z_0$ is the distance between top and bottom stacks, with an initial distance of z_0.

The friction force is assumed to have combined coulomb and viscous friction forces as:

$$F_r = -c_r\dot{x} - c_c sign(x) \tag{5.20}$$

where c_r and c_c are the force coefficients of coulomb and viscous frictions, respectively.

The force contribution of the electromagnetic component (F_e), is previously modeled for different distances (z) and applied currents (I) using finite element and theoretical methods in reference [132]. The theoretical and FEM models are too complicated to be implemented in real time control loops. Here a simplified nonlinear model of the electromagnetic component is obtained by utilizing curve fitting technique. Several models are considered for the curve fitting, among which, the following model is selected as it has a good comprise of high accuracy and simplicity. In the proposed curve fitting model, the electromagnetic force is given by:

$$\begin{aligned} F_e(z, I) &= F_{e1}(z) + F_{e2}(z)I & (5.21)\\ F_{e1}(z) &= az^2 + bz + c & (5.22)\\ F_{e2}(z) &= dz + e & (5.23) \end{aligned}$$

where a, b, c, d, and e are the curve fitting coefficients. It should be noted that, even at a zero applied current, there is still a repulsive force ($F_{e1}(z)$) between the top and bottom stacks. This force is due to magnets used in the two stacks, providing a magnetic spring for the system. In the presented model, although the electromagnetic force has a nonlinear relation with distance z, it is linearly proportional to the applied current I. This linear relation with current, helps in designing simple controllers with feedback linearization techniques. The model can simply predict the desired current (I_d) that is needed to generate a required amount of electromagnetic force (F_{ed}), specified by the controller. The values of curve fitting coefficients are listed in Table 5.3. These coefficients are obtained for a model in which the units of z and I are millimeter and ampere, respectively.

Table 5.3: Coefficients of the proposed curve fitting model for the electromagnetic forces.

Curve fit parameter	a	b	c	d	e
Value	1.942	-56.85	846.8	61.32	-2.638

The curve fitting results together with the error residuals are illustrated in Figure 5.8. The evaluated residuals correspond to less than 0.6 % relative error.

In order to model the force contribution of pneumatic spring (F_p), three models are considered: Nishimura [133], Vampire model [134], and Berg model [135]. These models are among the most common ones for predicting the pneumatic spring forces. It is found that the accuracy of all these models are very similar in predicting the pneumatic spring forces of the proposed device. Thus, Nishimura model is selected for modeling and control purposes, due to its simplicity. According to the Nishimura model, pneumatic spring force is:

$$\begin{aligned} F_p(x) =& F_{n0} + F_{n1} \\ F_{n1} =& -k_2 x - k_1(x-y) \\ c_n\dot{y} + \lambda k_1 y =& k_1(x-y) \end{aligned} \tag{5.24}$$

where F_{n0} is the portion of the static force compensated by pneumatic spring, and y is an

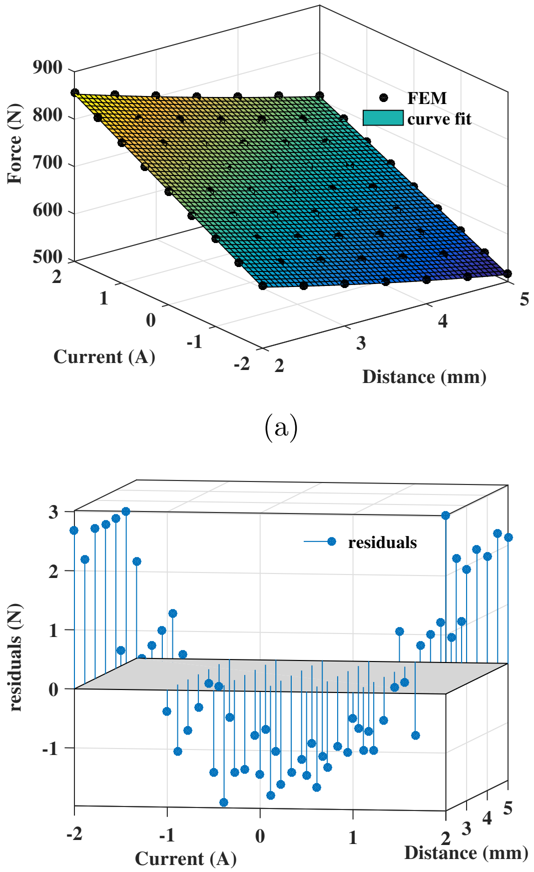

(a)

(b)

Figure 5.8: Curve fitting model for electromagnetic forces, a: curve fit forces, and b: error residuals.

auxiliary variable. The definition of F_{n0}, k_2, k_1, c_n, and λ are:

$$\begin{aligned}
F_{n0} =& A_e(P_0 - P_{at}) \\
k_1 =& nA_e^2 \frac{P_0}{V_a} \\
k_2 =& (P_0 - P_{at}) \frac{dA_e}{dx} \\
c_n =& RA_e^2 W_0 \\
\lambda =& \frac{V_a}{V_b}
\end{aligned} \tag{5.25}$$

where A_e is the effective area, P_0 and P_{at} are the initial and atmospheric pressures, respectively. n is the polytropic index, V_a and V_b are the volume of pneumatic spring and auxiliary tank, respectively. R is the flow resistance coefficient, and W_0 is the specific weight of the gas at the static equilibrium state.

5.4 Controller Design

This section is allocated to the formulation of different controllers for the active component of the vibration isolator. For each of the cases defined in section 1.3.2 (acceleration and force transmissibilities), different controllers are designed and experimentally tested under steady-state sinusoidal and random vibrations.

In order to energize the electromagnetic coils, a current source amplifier is used for both of the coils. The command signal (V_c) sent to the amplifier is:

$$V_c = k_n g_{amp}(V_{i,j} + V_{pe}) \tag{5.26}$$

where g_{amp} is the voltage to current conversion gain of the amplifier, $k_n = 2$ is the number of coils energized by the amplifier, $V_{i,j}$ is the control signal determined by the controller i for isolation case j, and V_{pe} is a penalty function used to ensure that relative displacement of top and bottom stacks will remain less than an absolute value of x_{max}, and thus will not hit the limits. The penalty function V_{pe} is given by:

$$\begin{aligned}
V_{pe} =& -k_{pe}(x - sat(x, x_{max})) \\
sat(x, x_{max}) =& min(max(x, -x_{max}), x_{max})
\end{aligned} \tag{5.27}$$

In the following, the control signal $V_{i,j}$ is formulated for two cases: acceleration (where $j = a$) and force (where $j = f$) transmissibilities.

5.4.1 Controlling Acceleration Transmissibility

In order to minimize the acceleration transmissibility, a proportional-integrator and a sliding mode controllers are utilized. The control signal of the proportional-integral controller ($V_{PI,a}$) is given by:

$$V_{PI,a} = -k_{P,a}\ddot{x}_m - k_{I,a}\dot{x}_m \tag{5.28}$$

where $k_{P,a}$ and $k_{I,a}$ are, respectively, the proportional and integral coefficients for acceleration transmissibility case.

In the design of the sliding mode controller (SMC), the first step is to define the sliding surface σ_a. In this study, σ_a is chosen as:

$$\sigma_a = x_m\gamma + \dot{x}_m \tag{5.29}$$

where γ is the surface constant. In this work, the second order twisting sliding mode controller, described in reference [136], is employed where the control signal ($V_{SMC,a}$) is calculated by the following equation:

$$V_{SMC,a} = -r_1 sign(\sigma_a) - r_2 sign(\dot{\sigma}_a) \tag{5.30}$$

in which r_1 and r_2 are constants.

5.4.2 Controlling Force Transmissibility

In the case of force transmissibility, the isolator is preloaded with a static load of F_{st} that is given by:

$$F_{st} = F_{e1}(z_0) + F_{n0} \tag{5.31}$$

where F_{e1} and F_{n0} are the contributions of electromagnetic and pneumatic springs, respectively, and z_0 is the static/initial distant between top and bottom stacks. The control objective is to minimize the dynamic load that is defined as the difference between the current force and static force ($F - F_{st}$).

The control signal of the proportional-integral-derivative controller ($V_{PID,f}$) is:

$$\begin{aligned} V_{PID,f} = &- k_{P,f}(F - F_{st}) \\ &- k_{I,f}\int (F - F_{st})dt - k_{D,f}\dot{F} \end{aligned} \tag{5.32}$$

where $k_{P,f}$, $k_{I,f}$ and $k_{D,f}$ are, respectively, the proportional, integral and derivative coefficients for force transmissibility case.

For the sliding mode controller, similar to the acceleration transmissibility case, here the second order twisting sliding mode controller is utilized. The SMC control signal is:

$$V_{SMC,f} = r_3 sign(\sigma_f) + r_4 sign(\dot{\sigma}_f) \tag{5.33}$$

in which, r_3 and r_4 are constants, and σ_f is the sliding surface, defined by:

$$\sigma_f = \lambda \int (F - F_{st})dt + F - F_{st} \tag{5.34}$$

where λ is the sliding surface constant.

In this work, we have also employed a model-based nonlinear controller for the force transmissibility case. Based on the concept of feedback linearization, a model based control force is added to the linear PID controller, to compensate for the nonlinear parts of the electromagnetic component. Based on equation (5.19), the desired electromagnetic force (F_{ed}) that is required to minimize the dynamic force is:

$$F_{ed} = F_{st} - F_p - F_r \tag{5.35}$$

In this equation, the magnitude of F_p and F_r are estimated from the models developed in Section 5.3. The desired current needed in the coils (I_d) to generate F_{ed} can be calculated from the electromagnetic model presented in Section 5.3. By substituting equation (5.35) in to equation (5.23), I_d is calculated as:

$$I_d = \frac{F_{st} - F_p - F_r - F_{e1}(z)}{F_{e2}(z)} \tag{5.36}$$

Therefore, the control signal of the feedback-linearization controller ($V_{FL,f}$) becomes:

$$\begin{aligned} V_{FL,f} = & I_d - k_{P,f}(F - F_{st}) \\ & - k_{I,f} \int (F - F_{st})dt - k_{D,f}\dot{F} \end{aligned} \tag{5.37}$$

Chapter 6

Active Hybrid Electromagnetic Vibration Isolator: Experimental and Simulation Results

Based on the design described in the previous chapter, the hybrid vibration isolator prototype is built, and is shown in Figure 6.1. The prototype has a weight of approximately 6.1 kg which can be significantly reduced in a commercialized product.

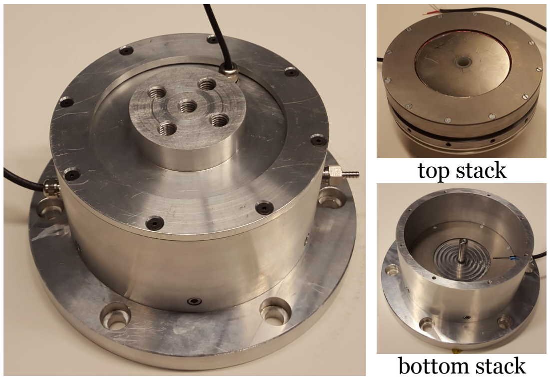
top stack
bottom stack

Figure 6.1: Electromagnetic-pneumatic hybrid actuator: the fabricated prototype.

6.1 Design and Model Validation

6.1.1 FEM Model Validation

This section validates the FEM results, and the electromagnetic force capability of the proposed actuator through experimental results. Furthermore, here, the time response of the electromagnetic component is analysed via FEM model to confirm the potential of the active electromagnetic actuator for wide bandwidth applications. The experimental setup, depicted in Figure 6.2a is prepared to validate the accuracy of the FEM model in predicting the electromagnetic forces. This setup is used to measure the displacement of an external load mass of 66 kg, when a step input current is applied to the coils. In the experiments, an AMC 50a20 current source amplifier and a Celesco SP2 string potentiometer are employed to amplify the input signal command and to measure displacement, respectively. The amplifier and the position sensor are interfaced with MATLAB® using an NI-6221 DAQ.

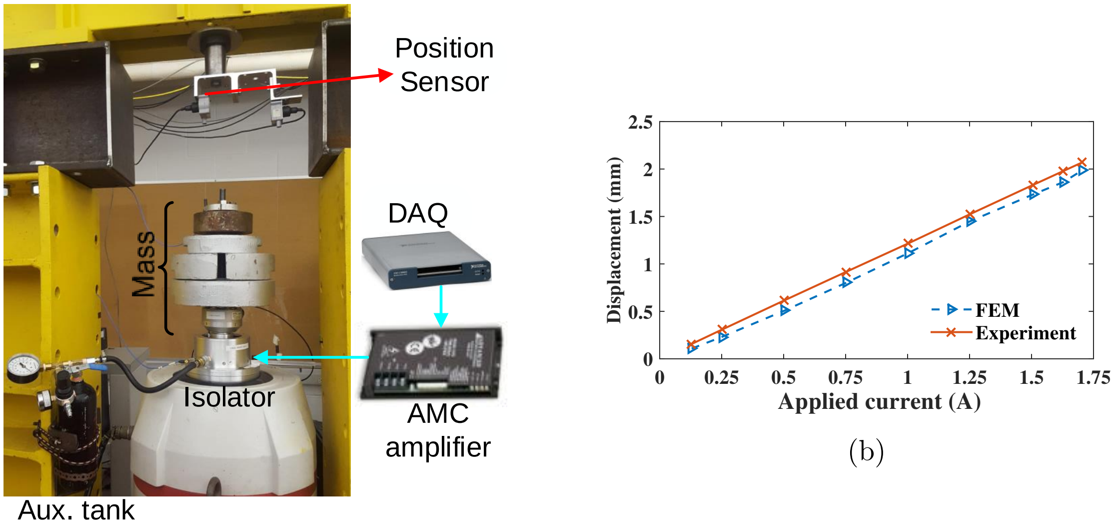

(a)

(b)

Figure 6.2: Experimental results, a: experimental setup, and b: displacements (change in stacks distance) corresponding to a step current input.

The experiments include applying a step current input to the coils and measuring the corresponding displacements. The experimentally measured displacements due to different applied step input currents are shown in Figure 6.2b, and compared with the predicted values from FEM model. It can be seen that there is a good agreement between experimental and FEM results, which validates the accuracy of the FEM model and the optimization solution. The results presented in Figures 5.6 and 6.2b, and together with the comparison given in Table 5.2, confirm the potentials of the active electromagnetic actuator in producing high density active forces, and in moving heavy masses within a large distance range. In the next step, further analysis is done to confirm the capability of the actuator in producing wide bandwidth forces. For this purpose, three different analyses are performed. In the first one, the apparent inductance (L_c) of coils are experimentally measured using a E4980A Agilent Precision LCR meter for a frequency range of 0-1000 Hz, as shown in Fig. 6.3a. The coil inductances are measured within stacks to include the iron path. The stack's coils have a resistance of $R_c \approx 11.5\ \Omega$, and therefore, based on the obtained results for the apparent inductance, the time constant ($\frac{L_c}{R_c}$) of coils are less than 5.2 ms.

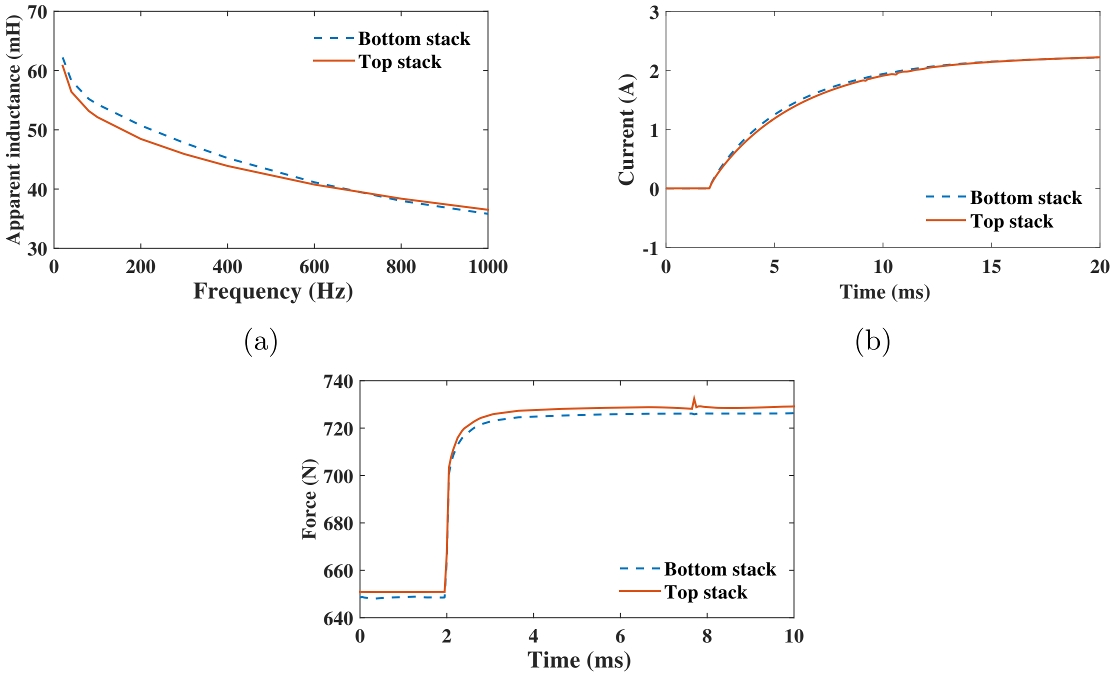

(a) (b)

(c)

Figure 6.3: Bandwidth analysis, a: apparent inductance at different frequencies (experiment), and b: time response of the coil currents for a step voltage input (FEM), and c: time response of the electromagnetic force for a step current input (FEM).

In the second analysis, the transient current responses of the coils to a step voltage are obtained. The current response, presented in Fig. 6.3b, is provided using the FEM model. A step input voltage of 23 V is applied at the time $t = 2$ ms to the coils, while the stacks distance is kept constant. The obtained current result has a time constant of less than 5 ms. The time constants reported in the first and second analyses demonstrate that with a proper controller, the active electromagnetic forces can be changed sufficiently fast for wide bandwidth applications. In a closed loop control system, current source amplifier can be used to enhance the time response for the electromagnetic coils. The third analysis is done to ensure that, in particular, the eddy current effect will not be a problem in generating wide bandwidth active forces. Due to the time varying magnetic field, electrical current (known as eddy current) is induced in the conductive materials, producing an opposing electromagnetic force that adversely affects the time response of the active actuator. In the proposed hybrid actuator, the electromagnetic flux density is carefully sealed by implementing iron (steel) parts around the coils and magnets, in order to minimize the flux leakage into the conductive aluminum parts. The transient electromagnetic force for a step input current of 1.5 A is presented in Fig. 6.3c. It is seen that the electromagnetic force increases from initial value to its final value in less than 2 ms, meaning that the eddy current effect is negligible. Finally, regarding the electromagnetic hysteresis effect, the electromagnets themselves are instantly magnetized and demagnetized, and thus, do not produce hysteresis effect. However, the iron pieces contribute and the effects are included in the provided performance graphs (e.g. Fig. 6.3).

6.1.2 Mathematical Model Validation

In order to validate the mathematical models (curve fit and Nishimura models for the electromagnetic and pneumatic components, respectively) developed in Section 5.3, the acceleration transmissibility of the hybrid vibration isolator, when the controller is off, is experimentally obtained, and compared with theoretical model. For this aim, the experimental test setup shown in Figure 6.4 is configured. In this setup, a load mass representing an equipment is connected to a moving foundation by the hybrid vibration isolator. The vibration isolator is connected to an auxiliary tank by a short hose. For the moving foundation, a V721 LDS shaker is used. The shaker is configured to apply a sinusoidal or random displacement profiles using a 33220A Agilent function generator. The displacements and accelerations (of both the mass and shaker) are measured using Celesco SP2 string potentiometers and Kistler accelerometers, respectively. All of the sensors are interfaced with MATLAB Simulink windows real time target toolbox using an NI-6221 DAQ. A 50A20 PWM amplifier from Advanced Motion Controls is used to energize the electromagnetic

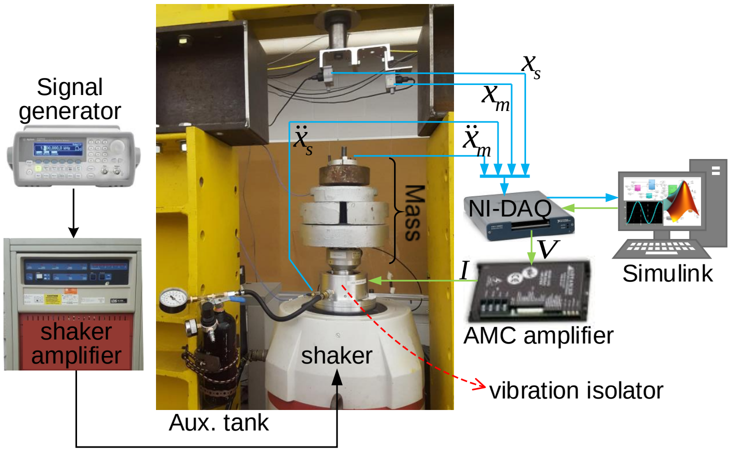

Figure 6.4: Experimental setup for model validation and acceleration transmissibility.

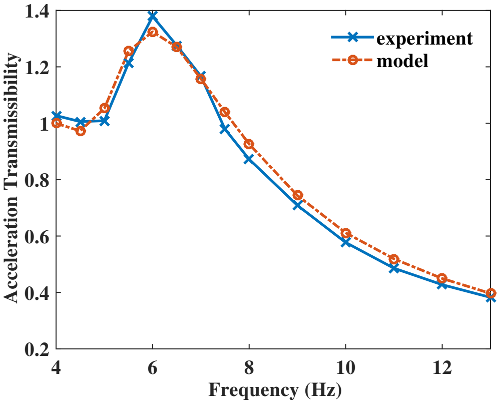

Figure 6.5: Comparison of mathematical and experimental results for acceleration transmissibility.

coils. In order to decrease the time response of the coils, the PWM amplifier is set to work in current mode. The applied current to each coil has maximum and minimum limits of -2.5 and 2.5 A, respectively (coils have a wire gauge of 22 AWG, and potentially have higher maximum current limits).

Figure 6.5 depicts the acceleration transmissibility results for the case where controller is off (zero applied currents). The results are obtained for excitation frequencies of 4-13 Hz, all with a constant displacement amplitude of 0.6 mm. As it can be seen, there is a good agreement between model and experimental results. This agreement validates the model, developed in Section 5.3. When the controller is off, the vibration isolator acts as a passive element. In this case, while the stiffness and support is provided by both of electromagnetic and pneumatic components, the damping force almost entirely is the contribution of pneumatic component. As it is expected, in a passive mode, the vibration isolation has a good vibration isolation at higher frequencies, but exhibits an undesired peak in lower frequencies.

6.2 Control Results

6.2.1 Acceleration Transmissibility (T_a)

In order to minimize the acceleration transmissibility, feedback controllers that are developed in Section 5.4.1 are implemented. It should be noted that in the controller experiments, the auxiliary tank is removed, so that the effect of the pneumatic spring is reduced, and thus the performance of the electromagnetic active actuator is scrutinized more closely.

Table 6.1: Controller results (RMS values) for normalized mass accelerations under random excitation.

Controller	Off	SMC	PID
Normalized mass acceleration	0.3987	0.1183	0.2122
Reduction (%)	—	70.3	46.8

Figure 6.6 represents experimental results for acceleration transmissibility under harmonic excitations. In this figure the displacement amplitude is set fixed at 0.5 mm for all frequencies. In Figure 6.6a, the time domain results of the mass acceleration for frequency of 8 Hz is illustrated. The mass accelerations are normalized by the RMS of the shaker

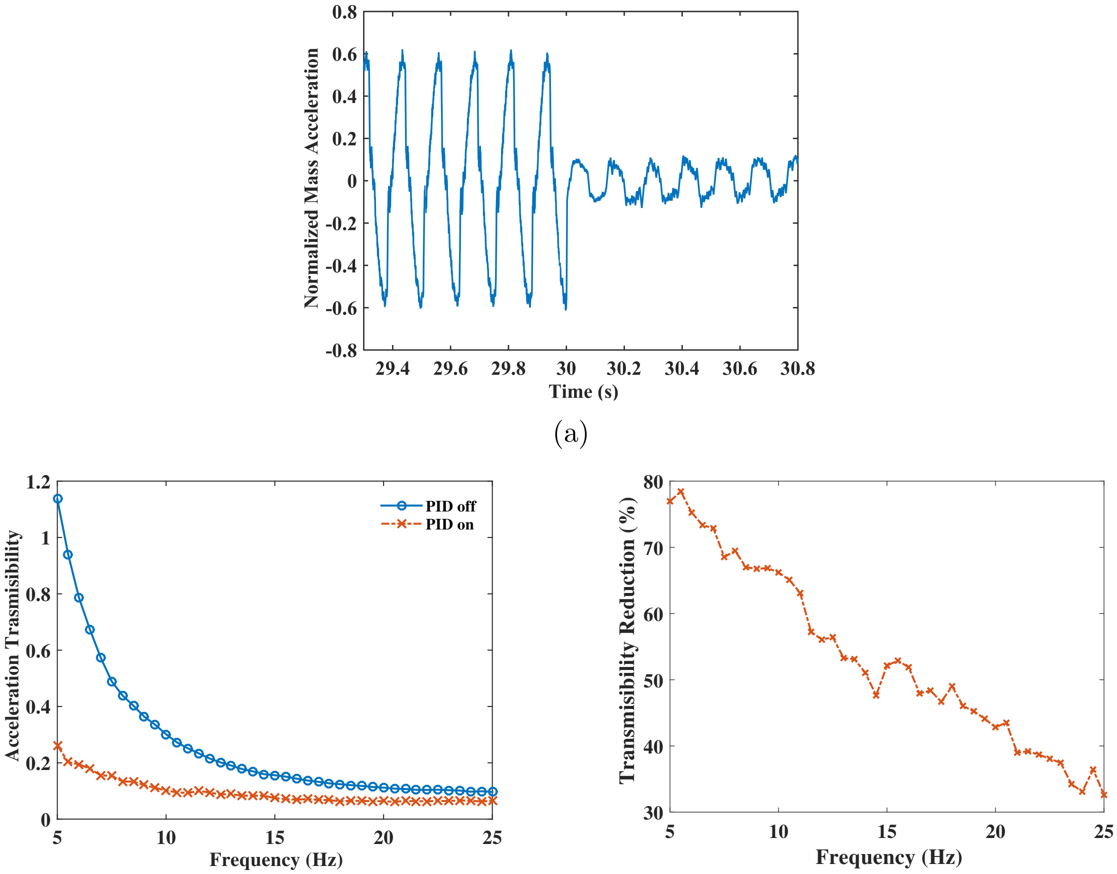

(a)

(b)

(c)

Figure 6.6: Acceleration transmissibility results under harmonic excitation with a displacement amplitude of 0.5 mm, and using a PID controller, a: time domain results for normalized mass acceleration under 8 Hz excitation (the controller starts at $t = 30\ s$), b: acceleration transmissibility for 5-25 Hz frequencies, and c: reduction of acceleration transmissibility under different controllers.

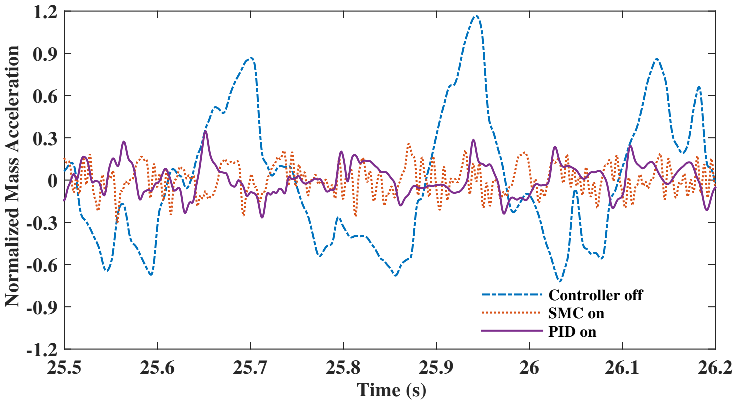

Figure 6.7: Acceleration transmissibility results under random excitation.

acceleration. This figure can be divided into two sections. In section one, starting from 0 to 30 s, the normalized mass accelerations are presented for the case where the controller is off (i.e. $V_c = 0$), and the system acts as a passive element. In the second part from 30 s, the PID controller starts energizing the coils, and thus reducing the amplitude of the normalized mass accelerations. Similar experiments are conducted for excitation frequencies of 5 to 25 Hz, and the summary of the results are shown in Figure 6.6b. Furthermore, the effectiveness of the controller, in reducing the acceleration transmissibility, is depicted in Figure 6.6c for different excitation frequencies. As it is observed in the acceleration transmissibility results, lower frequencies are the realm of the active electromagnetic actuator and feedback controller. In these regions passive elements are not adequately effective, however, their transmissibility can be improved by up to 80% using a feedback controller. In high frequencies, the passive elements have much lower transmissibility, and thus requiring less assist from the controller and active electromagnetic actuator. As the excitations shift from lower to higher frequencies the improvements, coming from the feedback controller, drop to 30%.

In addition to the harmonic excitations, the performance of the feedback controller, in reducing the acceleration transmissibility, is also examined under random excitations. Figure 6.7 illustrates, the normalized mass accelerations under PID and SMC controllers, and under no controller. A summary of the obtained results, for random excitations, is listed in Table 6.1. It can be seen that SMC and PID control algorithms improve the performance of the passive elements by up to 70.3 and 46.8 % respectively. The results obtained using the SMC controller show better vibration suppression, however, this controller introduces high frequency-low amplitude vibrations to the system. Therefore, depending on the application, SMC or PID control algorithms would be preferred for implementation.

6.2.2 Force Transmissibility (T_f)

For the case of force transmissibility, the experimental setup is updated, as shown in Figure 6.8. The dead load mass is removed, and the vibration isolator, from above, is locked to a fixture (that is bolted to the ground).

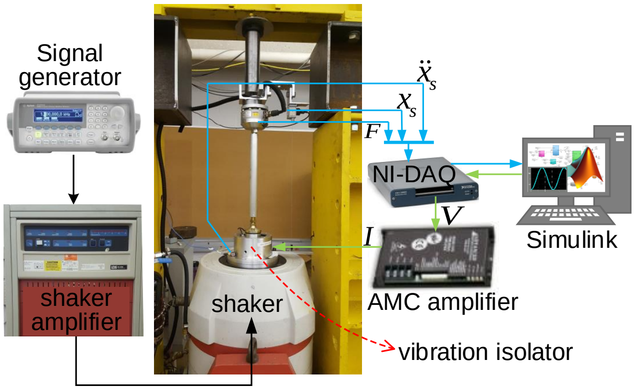

Figure 6.8: Experimental setup for force transmissibility (T_f).

The performance of the vibration isolator and controllers, in terms of force transmissibility (T_f), is investigated in Figure 6.9 where the shaker applies a sinusoidal excitation to the bottom stack with a fixed displacement amplitude of 0.5 mm. In Figure 6.9a, the time response of the system for the frequency of 9.5 Hz is shown. As it can be observed, as the PID controller starts working at $t = 31s$, the magnitude of the normalized forces (normalized by the input/shaker acceleration) drastically drops. Similar experiments are conducted for different frequencies and controllers, and a summary of the results is illustrated in Figure 6.9b. Furthermore, Figure 6.9c is provided to represents the how different controllers improve the force transmissibility, comparing to the case when controller is disabled.

Similar to the acceleration transmissibility case, here the active electromagnetic actuator and the implemented controllers are able to significantly improve the force transmissibility in lower frequencies (by up to 95%). The PID controller is still able to greatly affect the force transmissibility, even in higher frequencies. By shifting from 5 to 25 Hz, the

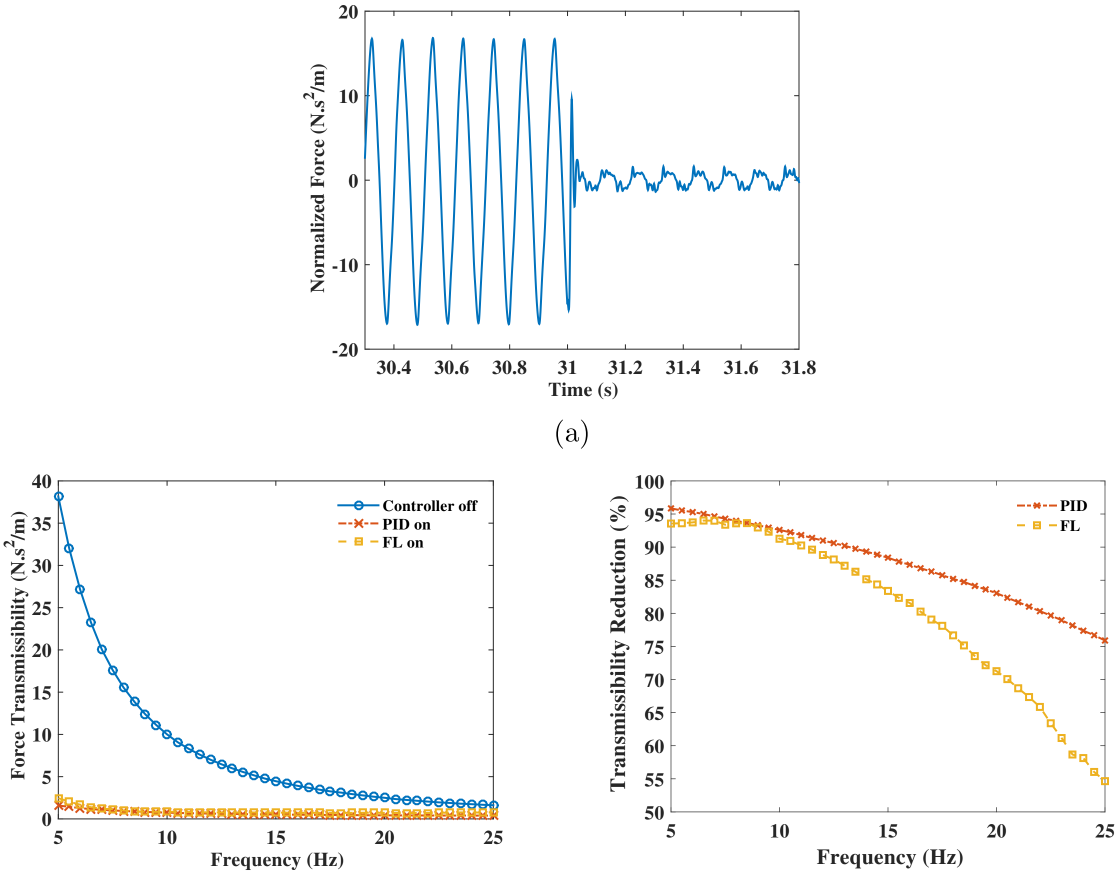

(a)

(b)

(c)

Figure 6.9: Force transmissibility (T_f) under harmonic excitations with a displacement amplitude of 0.5 mm, a: normalized force at 9.5 Hz excitation and under a PID control (the controller starts at $t = 31$ s), b: Force transmissibility for 5-25 Hz frequencies ,and c: reduction of force transmissibility under different controllers.

reduction of force transmissibility under the PID controller, slightly decrease from 95% to 80%. The results obtained using the FL controller shows that the controller works as effective as the PID controller in lower frequencies, while its T_f reduction in higher frequencies drops to 55% (which is still an acceptable reduction percentage).

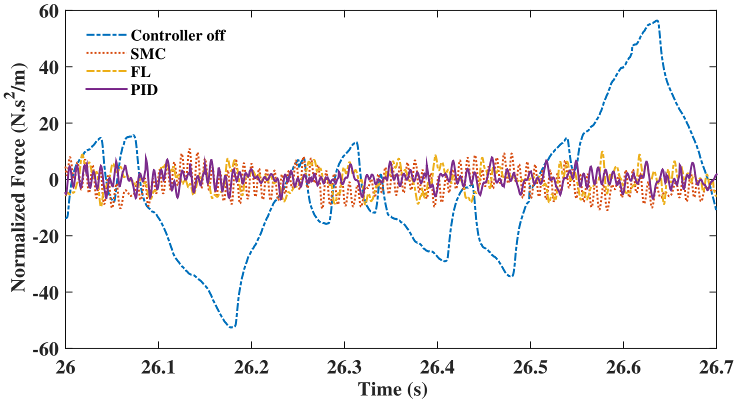

Figure 6.10: Normalized force results under random excitation.

The normalized force response of the system under random excitations is studied in Figure 6.10, where the normalized forces are compared for SMC, FL and PID controllers. The results of this figure are summarized in Table 6.2. The SMC and PID controllers are the least and the most effective ones.

Table 6.2: Controller results (RMS values) for normalized force under random excitation.

Controller	Off	SMC	FL	PID
Normalized force ($N.s^2/m$)	20.95	6.76	3.35	2.16
Reduction (%)	—	67.72	84.00	89.67

Generally, it can be observed that the PID controller works better than FL and SMC controllers in both of T_a and T_f cases.

6.3 Comparison Between the Proposed Semi-active and Active Hybrid Devices

In this PhD work two different hybrid systems are proposed: A semi-active hybrid damper and an active hybrid vibration isolator. These two systems are different in many ways including the definition, application, size, actuation mode and etc. Below the main differences of the two devices are listed.

- The first device, by definition, is a damper that provides damping force with no stiffness, while the second one is a vibration isolator that includes both of damping and stiffness elements inside.
- Both of the systems have an electromagnetic component that can be used in either semi-active or active mode. However, in the damper, a semi-active mode and in the vibration isolator, an active mode is considered during the design and optimization and characterization.
- In the proposed damper, the electromagnetic component is required to be combined with another component that can provide high levels of fail-safe damping. Thus a hydraulic component is selected as the complementary component. On the other hand, for the proposed vibration isolator, the complementary component is required to provide extra fail-safe stiffness for the isolation. Furthermore the complementary component should not adversely affect the performance of the active electromagnetic component. Thus, here a pneumatic spring is selected as the complementary component.
- The hybrid damper has a hydraulic damping of 1300 $N.s/m$ together with an electromagnetic variable damping of 0-240 $N.s/m$. The Hybrid damper does not provide stiffness and has no support for external static loads. The hybrid vibration isolator is designed to have a static force of $600 - 800$ N for an external dead load masses. In addition to the pneumatic and magnetic spring forces, the system is able to provide a force variation of 318 N, and 397.5 N by applying ± 2 A and ± 2.5 A currents, respectively.
- Weights of both devices are close to each other (around $6 - 7$ kg). The proposed damper has a large aspect ratio of around 4 while the low profile vibration isolator has a very small aspect ratio of around 0.5.

- In general, it can be said that the by moving forward from the first device to the second one, a semi-active damper with a large aspect ratio becomes an active vibration isolation system with a small aspect ratio.

Chapter 7

Conclusions and Future Work

Recently, many researchers have studied electromagnetic technologies in active/semi-active vibration isolators. Despite the introduction of many promising concepts in the literature, the area is still at an exploratory stage and better designs are needed for practical applications. This thesis focuses on developing hybrid electromagnetic vibration isolation systems to address the shortcomings of the currently available electromagnetic vibration isolators. In this thesis concept of hybrid electromagnetic vibration isolation is proposed and experimentally validated in which an electromagnetic component is combined with a passive element in a single package. The electromagnetic component provides force control for the system, and the passive element addresses the shortcomings of the electromagnetic component.

In this work conceptual designs were proposed for both cases of semi-active and active systems. The proposed semi-active conceptual design is a hybrid electromagnetic damper that composed of a viscous medium and an electromagnetic generator. The viscous component provides a baseline and fail-safe damping force while the electromagnetic components add the adaptability and energy recovery to the system. The active conceptual design was developed by implementing an active electromagnetic actuator and a passive pneumatic spring. This device is aimed at isolating vibrations at both low and high frequencies. While the passive component guarantees a low vibration transmissibility at high frequencies, the active force controller corrects and improve vibration transmissibility for a wide frequency range.

The detail design of the semi-active hybrid electromagnetic damper was reported (based on the concept proposed in Section 1.3.2). This damper was developed to address the need to have variable and fail-safe damping mechanism in the automotive suspension systems.

The electromagnetic component was modeled using LEMC and FEM methods, and accordingly an optimized solution was presented for the geometric parameters. In order to have a better understanding of the adaptive electromagnetic damping mechanism, an extended analysis was also presented in which the effects of some of the important parameters on the performance of the electromagnetic component were studied.

Following the design of the semi-active hybrid electromagnetic damper, experimental and simulation results were provided to investigate the performance of the proposed design. Based on the proposed hybrid concept (electromagnetic hybrid damper) and the optimized design, a prototype was fabricated and tested. A good agreement was observed between the results obtained from modified FEM model and experimental tests. The results showed that a baseline and variable damping coefficient of 1300 Nsm^{-1} and 0-238 Nsm^{-1} were achieved through the viscous and electromagnetic components, respectively. This variability can be exploited as a tool to enhance the dynamic performance of system according to the road profile and driving condition. To achieve variable damping, the apparent external resistance shunted across each coil requires adjustment through an electrical circuit and controller.

Upon the validation of the concept semi-active hybrid electromagnetic damper, a multi-objective optimization process is used to design and optimize a vehicle suspension system that is equipped with the proposed damper. The electromagnetic component was modeled using the method of lumped equivalent magnetic circuit and was integrated into a quarter car suspension model. The ride comfort, road holding and energy harvesting are the three criteria used to optimize the suspension systems performance. The optimization results were presented as a Pareto front providing a set of solutions. According to the results, the overall-optimized suspension system delivers better ride comfort and road holding quality, compared to the conventional and not-optimized hybrid design, and is also able to regenerate higher rates of electrical energy compared to the not-optimized regenerative suspension model.

The detail design of a new active hybrid electromagnetic vibration isolator was reported based on the proposed concept in Section 1.2. The designed electromagnetic component has a modular design, meaning that the length of actuator's stroke can be modified, simply by reconfiguring the actuator with different number of stacks. The electromagnetic component was modeled, and furthermore optimized using analytical and finite element methods. It was demonstrated that the proposed low-profile actuator has a larger force density, comparing to the voice coil of similar size. The electromagnetic component has a compact design with a diameter of $\sim 125\ mm$ and a height of $\sim 60\ mm$. According to the results, it has a force variation of $\sim 318\ N$ for the currents of $I = \pm 2\ A$. The hydraulic component is also modeled using Nishimura method. Using the developed models, three controllers were developed, for the vibration isolator, based on PID, sliding mode and feedback linearization techniques.

The designed active hybrid electromagnetic vibration isolator was validated by presenting experimental and simulation results. It was also shown that the electromagnetic force has a small time constant of less than 5.2 ms, and the eddy current effect is negligible, making the active force suitable for wide bandwidth applications. The effectiveness of the previously designed controllers were examined in two cases: acceleration and force transmissibilities. In both cases, the results showed that the PID controller is more effective than the other two. Comparing to the passive mode (when the applied current is zero), the controllers are able to improve the performance by up to 80 % and 95 % for acceleration and force transmissibilities, respectively.

7.1 Future Work

A few suggestions are made in this section for future work to carry on the research that is conducted in this thesis.

- In practice, it was seen that in the semi-active hybrid electromagnetic damper, oil is leaking from the hydraulic into the electromagnetic component. This leak does not damage the electromagnetic component, yet it reduces the performance of the hydraulic component. Design revisions are needed to address this problem. The aluminum shaft should be further replaced with a stronger material such as non magnetic steel to avoid shaft bending.
- The semi-active hybrid electromagnetic damper was implemented in a simulated vehicle suspension system to study its effects on the vehicle ride comfort, road holding as well as the energy harvesting. The simulation results can be further investigated using experimental data. For this aim, the fabricated damper can be installed in a mid-size SUV. A closed loop controller can also be developed to regulate the external resistance of the coils to control the damping of the suspension, and enhance the ride comfort and road holding.
- In section 2.4.2 effects of some parameters on the performance of the electromagnetic damper were investigated which, despite their effect on the system performance, in many studies are either neglected or not considered. The outcome of those investigations raised some questions regarding the suitability of some of the commonly used optimization strategies. The answer to those questions are left as a future research topic.

- The proposed active hybrid electromagnetic actuator has a modular design. This feature is not fully investigated in this work. It is suggested that a new actuator is modeled with more number of stacks (3-4 stacks) to study the effects of added weights as well as the mutual inductance between coils.

- Both of the proposed semi-active and active actuators are designed with extra caution (e.g. using heavy brass bushings in the semi-active actuator). This resulted in heavy and bulky designs. Commercial versions of both actuators can be designed where the weights are expected to reduce significantly.

References

[1] A. Okyay, M. B. Khamesee, and K. Erkorkmaz, "Design and optimization of a voice coil actuator for precision motion applications," *Magnetics, IEEE Transactions on*, vol. 51, no. 6, pp. 1–10, 2015.

[2] L. Zuo, B. Scully, J. Shestani, and Y. Zhou, "Design and characterization of an electromagnetic energy harvester for vehicle suspensions," *Smart Materials and Structures*, vol. 19, no. 4, p. 045003, 2010.

[3] X. Tang, T. Lin, and L. Zuo, "Electromagnetic vibration energy harvesting with high power density using a magnet array," in *SPIE Smart Structures and Materials+ Nondestructive Evaluation and Health Monitoring*, pp. 83410Y–83410Y, International Society for Optics and Photonics, 2012.

[4] A. Gupta, J. Jendrzejczyk, T. Mulcahy, and J. Hull, "Design of electromagnetic shock absorbers," *International Journal of Mechanics and Materials in Design*, vol. 3, no. 3, pp. 285–291, 2006.

[5] H. Wang, "Analytical analysis of a beam flexural-mode piezoelectric actuator for deformable mirrors," *Journal of Astronomical Telescopes, Instruments, and Systems*, vol. 1, no. 4, pp. 049001–049001, 2015.

[6] L. Zuo and X. Tang, "Large-scale vibration energy harvesting," *Journal of intelligent material systems and structures*, vol. 24, no. 11, pp. 1405–1430, 2013.

[7] B. Ebrahimi and B. Hamesee, *Development of Hybrid Electromagnetic Dampers for Vehicle Suspension Systems.* PhD thesis, University of Waterloo, 2009.

[8] R. Palomera-Arias, *Passive electromagnetic damping device for motion control of building structures.* PhD thesis, Massachusetts Institute of Technology, 2005.

[9] B. Erkus, M. Abé, and Y. Fujino, "Investigation of semi-active control for seismic protection of elevated highway bridges," *Engineering Structures*, vol. 24, no. 3, pp. 281–293, 2002.

[10] B. Ebrahimi, "Development of hybrid electromagnetic dampers for vehicle suspension systems," 2009.

[11] Z. Li, L. Zuo, J. Kuang, and G. Luhrs, "Energy-harvesting shock absorber with a mechanical motion rectifier," *Smart Materials and Structures*, vol. 22, no. 2, p. 025008, 2012.

[12] G. Mikułowski, R. Wiszowaty, and J. Holnicki-Szulc, "Characterization of a piezoelectric valve for an adaptive pneumatic shock absorber," *Smart Materials and Structures*, vol. 22, no. 12, p. 125011, 2013.

[13] D. Shi, L. Chen, R. Wang, H. Jiang, and Y. Shen, "Design and experiment study of a semi-active energy-regenerative suspension system," *Smart Materials and Structures*, vol. 24, no. 1, p. 015001, 2014.

[14] B. Vlasic, "Us sets higher fuel efficiency standards," *New York Times*, p. B1, 2012.

[15] L. Zuo, "Energy Harvesting, Ride Comfort, and Road Handling of Regenerative Vehicle Suspensions," *Journal of Vibration and Acoustics*, vol. 135, p. 011002, feb 2013.

[16] S. Savaresi, C. Poussot-Vassal, and C. Spelta, *Semi-active suspension control design for vehicles*. 2010.

[17] Audi-AG, "Audi magnetic ride," 2011.

[18] Audi-AGb, "Adaptive air suspension," 2012.

[19] Audi-AGc, "Dynamic ride control," 2011.

[20] Mercedes-Benz, "Active body control abc."

[21] BMW, "Dynamic drive."

[22] A. Gupta, J. a. Jendrzejczyk, T. M. Mulcahy, and J. R. Hull, "Design of electromagnetic shock absorbers," *International Journal of Mechanics and Materials in Design*, vol. 3, no. 3, pp. 285–291, 2006.

[23] Y. Kawamoto, Y. Suda, H. Inoue, and T. Kondo, “Electro-mechanical suspension system considering energy consumption and vehicle manoeuvre,” *Vehicle System Dynamics*, vol. 46, pp. 1053–1063, sep 2008.

[24] K. Nakano, “Combined Type Self-Powered Active Vibration Control of Truck Cabins,” *Vehicle System Dynamics*, vol. 41, pp. 449–473, dec 2004.

[25] I. L. Cassidy, J. T. Scruggs, S. Behrens, and H. P. Gavin, “Design and experimental characterization of an electromagnetic transducer for large-scale vibratory energy harvesting applications,” *Journal of Intelligent Material Systems and Structures*, vol. 22, no. 17, pp. 2009–2024, 2011.

[26] G. Zhang, J. Cao, and F. Yu, “Design of active and energy-regenerative controllers for DC-motor-based suspension,” *Mechatronics*, vol. 22, pp. 1124–1134, dec 2012.

[27] Y. Zhang, K. Huang, F. Yu, Y. Gu, and D. Li, “Experimental verification of energy-regenerative feasibility for an automotive electrical suspension system,” *2007 IEEE International Conference on Vehicular Electronics and Safety*, pp. 1–5, dec 2007.

[28] L. C. Rome, L. Flynn, E. M. Goldman, and T. D. Yoo, “Generating electricity while walking with loads.,” *Science (New York, N.Y.)*, vol. 309, no. September, pp. 1725–1728, 2005.

[29] Z. Li, L. Zuo, J. Kuang, and G. Luhrs, “Energy-harvesting shock absorber with a mechanical motion rectifier,” *Smart Materials and Structures*, vol. 22, p. 025008, feb 2013.

[30] Z. Li, Z. Brindak, and L. Zuo, “Modeling of an electromagnetic vibration energy harvester with motion magnification,” *the ASME 2011 International Mechanical Engineering Congress & Exposition IMECE2011*, pp. 285–293, 2011.

[31] R. A. Oprea, M. Mihailescu, A. I. Chirila, and I. D. Deaconu, “Design and efficiency of linear electromagnetic shock absorbers,” in *2012 13th International Conference on Optimization of Electrical and Electronic Equipment (OPTIM)*, vol. 42, pp. 630–634, IEEE, may 2012.

[32] D. Ryba, “Semi-active Damping with an Electromagnetic Force Generator,” *Vehicle System Dynamics*, vol. 22, pp. 79–95, jan 1993.

[33] J. Eastham, “Novel synchronous machines: linear and disc,” *Electric Power Applications, IEE Proceedings B*, pp. 49–58, 1990.

[34] L. Zuo, B. Scully, J. Shestani, and Y. Zhou, "Design and characterization of an electromagnetic energy harvester for vehicle suspensions," in *Smart Materials and Structures*, vol. 19, p. 045003, apr 2010.

[35] X. Tang, T. Lin, and L. Zuo, "Electromagnetic vibration energy harvesting with high power density using a magnet array," in *SPIE Smart Structures and Materials+ Nondestructive Evaluation and Health Monitoring*, pp. 83410Y–83410Y, International Society for Optics and Photonics, 2012.

[36] J. Eastham, "Novel synchronous machines: linear and disc," in *IEE Proceedings B-Electric Power Applications*, vol. 137, pp. 49–58, IET, 1990.

[37] G. Dajaku and D. Gerling, "Stator slotting effect on the magnetic field distribution of salient pole synchronous permanent-magnet machines," *IEEE Transactions on magnetics*, vol. 46, no. 9, pp. 3676–3683, 2010.

[38] Y. Zhang, K. Huang, F. Yu, Y. Gu, and D. Li, "Experimental verification of energy-regenerative feasibility for an automotive electrical suspension system," in *Vehicular Electronics and Safety, 2007. ICVES. IEEE International Conference on*, pp. 1–5, IEEE, 2007.

[39] R. Oprea, M. Mihailescu, A. Chirila, and I. Deaconu, "Design and efficiency of linear electromagnetic shock absorbers," in *Optimization of Electrical and Electronic Equipment (OPTIM), 2012 13th International Conference on*, pp. 630–634, IEEE, 2012.

[40] D. Ryba, "Semi-active damping with an electromagnetic force generator," *Vehicle System Dynamics*, vol. 22, no. 2, pp. 79–95, 1993.

[41] M. Montazeri-Gh and O. Kavianipour, "Investigation of the passive electromagnetic damper," *Acta Mechanica*, vol. 223, no. 12, pp. 2633–2646, 2012.

[42] R. L. Forward, "Electronic damping of vibrations in optical structures," *Appl. Opt.*, vol. 18, pp. 690–697, Mar 1979.

[43] S. Prakash, T. R. Kumar, S. Raja, D. Dwarakanathan, H. Subramani, and C. Karthikeyan, "Active vibration control of a full scale aircraft wing using a reconfigurable controller," *Journal of Sound and Vibration*, vol. 361, pp. 32 – 49, 2016.

[44] G. Wang, C. Chen, and S. Yu, "Optimization and static output-feedback control for half-car active suspensions with constrained information," *Journal of Sound and Vibration*, vol. 378, pp. 1 – 13, 2016.

[45] P. Li, J. Lam, and K. C. Cheung, "Multi-objective control for active vehicle suspension with wheelbase preview," *Journal of Sound and Vibration*, vol. 333, no. 21, pp. 5269 – 5282, 2014.

[46] L.-X. Guo and L.-P. Zhang, "Robust h control of active vehicle suspension under non-stationary running," *Journal of Sound and Vibration*, vol. 331, no. 26, pp. 5824 – 5837, 2012.

[47] F. Hausberg, C. Scheiblegger, P. Pfeffer, M. Plchl, S. Hecker, and M. Rupp, "Experimental and analytical study of secondary path variations in active engine mounts," *Journal of Sound and Vibration*, vol. 340, pp. 22 – 38, 2015.

[48] C.-M. Lee, V. Goverdovskiy, and A. Sotenko, "Helicopter vibration isolation: Design approach and test results," *Journal of Sound and Vibration*, vol. 366, pp. 15–26, 2016.

[49] M. Abdel-Rohman, "Feasibility of active control of tall buildings against wind," *Journal of Structural Engineering*, vol. 113, no. 2, pp. 349–362, 1987.

[50] E. Asadi, R. Ribeiro, M. Behrad Khamesee, and A. Khajepour, "A new adaptive hybrid electromagnetic damper: modelling, optimization, and experiment," *Smart Materials and Structures*, vol. 24, no. 7, p. 075003, 2015.

[51] L. Sun, C. Hansen, and C. Doolan, "Evaluation of the performance of a passive–active vibration isolation system," *Mechanical Systems and Signal Processing*, vol. 50, pp. 480–497, 2015.

[52] Y.-H. Liu and W.-H. Wu, "Active vibration isolation using a voice coil actuator with absolute velocity feedback control," *International Journal of Automation and Smart Technology*, vol. 3, no. 4, pp. 221–226, 2013.

[53] C. Hansen, S. Snyder, X. Qiu, L. Brooks, and D. Moreau, *Active control of noise and vibration*. CRC Press, 2012.

[54] X. Tan and J. S. Baras, "Modeling and control of hysteresis in magnetostrictive actuators," *Automatica*, vol. 40, no. 9, pp. 1469–1480, 2004.

[55] J. Shaw, "Active vibration isolation by adaptive control," in *Control Applications, 1999. Proceedings of the 1999 IEEE International Conference on*, vol. 2, pp. 1509–1514, IEEE, 1999.

[56] B. Rebbechi, C. Howard, and C. Hansen, “Active control of gearbox vibration,” in *Proceedings of the Active Control of Sound and Vibration Conference*, pp. 295–304, Fort Lauderdale, 1999.

[57] J. Li, X. Zhou, H. Zhao, M. Shao, N. Li, S. Zhang, and Y. Du, “Development of a novel parasitic-type piezoelectric actuator,” *IEEE/ASME Transactions on Mechatronics*, vol. PP, no. 99, pp. 1–1, 2016.

[58] J. H. Jacobs and T. T. Hyde, “Hybrid passive and active vibration isolator architecture,” Mar. 12 2002. US Patent 6,354,576.

[59] C. Yong, D. Zimcik, V. K. Wickramasinghe, and F. Nitzsche, “Development of the smart spring for active vibration control of helicopter blades,” *Journal of Intelligent Material Systems and Structures*, vol. 15, no. 1, pp. 37–47, 2004.

[60] C. Erin, B. Wilson, and J. Zapfe, “An improved model of a pneumatic vibration isolator: theory and experiment,” *Journal of sound and vibration*, vol. 218, no. 1, pp. 81–101, 1998.

[61] P.-C. Chen and M.-C. Shih, “Modeling and robust active control of a pneumatic vibration isolator,” *Journal of Vibration and Control*, vol. 13, no. 11, pp. 1553–1571, 2007.

[62] M. Heertjes and N. van de Wouw, “Nonlinear dynamics and control of a pneumatic vibration isolator,” *Journal of Vibration and acoustics*, vol. 128, no. 4, pp. 439–448, 2006.

[63] G. T. Pinson, “Active vibration stabilizer and isolator,” Apr. 5 1988. US Patent 4,735,296.

[64] J. Lim and K.-M. Lee, “Design of electromagnetic actuators using layout optimization with distributed current source models,” *IEEE/ASME Transactions on Mechatronics*, vol. 20, no. 6, pp. 2726–2735, 2015.

[65] K. Nakano, Y. Suda, and S. Nakadai, “Self-powered active vibration control using a single electric actuator,” *Journal of Sound and Vibration*, vol. 260, no. 2, pp. 213–235, 2003.

[66] S.-M. Kim, S. Pietrzko, and M. J. Brennan, “Active vibration isolation using an electrical damper or an electrical dynamic absorber,” *Control Systems Technology, IEEE Transactions on*, vol. 16, no. 2, pp. 245–254, 2008.

[67] X. He, T. Ng, S. Sivashanker, and K. Liew, “Active control of fgm plates with integrated piezoelectric sensors and actuators,” *International journal of Solids and Structures*, vol. 38, no. 9, pp. 1641–1655, 2001.

[68] M. Brennan, J. Garcia-Bonito, S. Elliott, A. David, and R. Pinnington, “Experimental investigation of different actuator technologies for active vibration control,” *Smart materials and structures*, vol. 8, no. 1, p. 145, 1999.

[69] H. Y. Kim, H. Kim, D.-G. Gweon, and J. Jeong, “Development of a novel spherical actuator with two degrees of freedom,” *IEEE/ASME Transactions on Mechatronics*, vol. 20, no. 2, pp. 532–540, 2015.

[70] H.-T. Zhang, Z. Chen, P. Chen, X. Zhang, and H. Ding, “Saturated output regulation approach for active vibration control of thin-walled flexible workpieces with voice coil actuators,” *IEEE/ASME Transactions on Mechatronics*, vol. 21, no. 1, pp. 266–275, 2016.

[71] D. B. Roemer, M. M. Bech, P. Johansen, and H. C. Pedersen, “Optimum design of a moving coil actuator for fast-switching valves in digital hydraulic pumps and motors,” *IEEE/ASME Transactions on Mechatronics*, vol. 20, no. 6, pp. 2761–2770, 2015.

[72] A. Preumont, M. Horodinca, I. Romanescu, B. De Marneffe, M. Avraam, A. Deraemaeker, F. Bossens, and A. A. Hanieh, “A six-axis single-stage active vibration isolator based on stewart platform,” *Journal of sound and vibration*, vol. 300, no. 3, pp. 644–661, 2007.

[73] D. L. Trumper and T. Sato, “A vibration isolation platform,” *Mechatronics*, vol. 12, no. 2, pp. 281–294, 2002.

[74] J. Spanos, Z. Rahman, and G. Blackwood, “A soft 6-axis active vibration isolator,” in *American Control Conference, Proceedings of the 1995*, vol. 1, pp. 412–416, IEEE, 1995.

[75] L. Miller, M. Ahmadian, C. Nobles, and D. Swanson, “Modelling and performance of an experimental active vibration isolator,” *Journal of vibration and acoustics*, vol. 117, no. 3A, pp. 272–278, 1995.

[76] S. Wakui, “Active vibration isolator, exposure apparatus, exposure method and device manufacturing method,” Sept. 11 2001. US Patent 6,286,644.

[77] M.-K. Zhou, Z.-K. Hu, X.-C. Duan, B.-L. Sun, L.-L. Chen, Q.-Z. Zhang, and J. Luo, "Performance of a cold-atom gravimeter with an active vibration isolator," *Physical Review A*, vol. 86, no. 4, p. 043630, 2012.

[78] R. Banik and D.-G. Gweon, "Design and optimization of voice coil motor for application in active vibration isolation," *Sensors and Actuators A: Physical*, vol. 137, no. 2, pp. 236–243, 2007.

[79] Y.-D. Chen, C.-C. Fuh, and P.-C. Tung, "Application of voice coil motors in active dynamic vibration absorbers," *Magnetics, IEEE Transactions on*, vol. 41, no. 3, pp. 1149–1154, 2005.

[80] K. Park, D. Choi, A. Ozer, S. Kim, Y. Lee, and D. Joo, "A voice coil actuator driven active vibration isolation system with the consideration of flexible modes," *Review of Scientific Instruments*, vol. 79, no. 6, p. 065106, 2008.

[81] G. K. Foshage, T. Davis, J. M. Sullivan, T. Hoffman, and A. Das, "Hybrid active/passive actuator for spacecraft vibration isolation and suppression," in *SPIE's 1996 International Symposium on Optical Science, Engineering, and Instrumentation*, pp. 104–122, International Society for Optics and Photonics, 1996.

[82] Y. Suda, S. Nakadai, and K. Nakano, "Hybrid suspension system with skyhook control and energy regeneration (development of self-powered active suspension)," *Vehicle system dynamics*, vol. 29, no. S1, pp. 619–634, 1998.

[83] I. Martins, M. Esteves, F. P. da Silva, and P. Verdelho, "Electromagnetic hybrid active-passive vehicle suspension system," in *Vehicular Technology Conference, 1999 IEEE 49th*, vol. 3, pp. 2273–2277, IEEE, 1999.

[84] "An anti-windup strategy for active vibration isolation systems," *Control Engineering Practice*, vol. 14, no. 1, pp. 17–27, 2006.

[85] R. Roberto, "Regenerative and adaptive shock absorber: A hybrid design," 2014.

[86] H. Lu, J. Zhu, and Y. Guo, "Development of a slotless tubular linear interior permanent magnet micromotor for robotic applications," *IEEE transactions on magnetics*, vol. 41, no. 10, pp. 3988–3990, 2005.

[87] A. Basak and G. Shirkoohi, "Computation of magnetic field in dc brushless linear motors built with ndfeb magnets," *IEEE Transactions on Magnetics*, vol. 26, no. 2, pp. 948–951, 1990.

[88] B. Sapiński and S. Krupa, "Efficiency improvement in a vibration power generator for a linear mr damper: numerical study," *Smart Materials and Structures*, vol. 22, no. 4, p. 045011, 2013.

[89] R. Palomera-Arias, J. J. Connor, and J. A. Ochsendorf, "Feasibility study of passive electromagnetic damping systems," *Journal of structural engineering*, vol. 134, no. 1, pp. 164–170, 2008.

[90] N.-C. Tsai and C.-W. Chiang, "Design and analysis of magnetically-drive actuator applied for linear compressor," *Mechatronics*, vol. 20, no. 5, pp. 596–603, 2010.

[91] M. Jadhav, S. Belkar, and R. Kharde, "Analysis of displacement sensitive twin tube shock absorber," *Analysis*, vol. 5, no. 5, pp. 31–41, 2012.

[92] U. Ferdek and J. Łuczko, "Modeling and analysis of a twin-tube hydraulic shock absorber," *Journal of Theoretical and Applied Mechanics*, vol. 50, no. 2, pp. 627–638, 2012.

[93] J. Wang, D. Howe, and G. W. Jewell, "Analysis and design optimization of an improved axially magnetized tubular permanent-magnet machine," *IEEE transactions on energy conversion*, vol. 19, no. 2, pp. 289–295, 2004.

[94] R. Ribeiro, E. Asadi, M. B. Khamesee, and A. Khajepour, "Hybrid variable damping control: design, simulation, and optimization," *Microsystem Technologies*, vol. 20, no. 8-9, pp. 1723–1732, 2014.

[95] N. Bianchi, S. Bolognani, D. D. Corte, and F. Tonel, "Tubular linear permanent magnet motors: an overall comparison," *IEEE transactions on industry applications*, vol. 39, no. 2, pp. 466–475, 2003.

[96] E. Asadi, R. Ribeiro, M. B. Khamesee, and A. Khajepour, "Analysis, prototyping and experimental characterization of an adaptive hybrid-electromagnetic damper for automotive suspension systems," *IEEE Transactions on Vehicular Technology*, 2016.

[97] D. Zhu, S. P. Beeby, M. J. Tudor, and N. R. Harris, "Electromagnetic Vibration Energy Harvesting Using an Improved Halbach Array," *PowerMEMS 2012*, no. 1, pp. 1–4, 2012.

[98] D. Zhu, S. Beeby, J. Tudor, and N. Harris, "Increasing output power of electromagnetic vibration energy harvesters using improved Halbach arrays," *Sensors and Actuators A: Physical*, vol. 203, pp. 11–19, dec 2013.

[99] J. den Hartog, *Mechanical vibrations.* 1956.

[100] M. Soliman and E. Abdel-Rahman, "Output Power Optimization for Electromagnetic Vibration Energy Harvesters," *ASME 2010 ...*, 2010.

[101] T. Inoue, Y. Ishida, and M. Sumi, "Vibration Suppression Using Electromagnetic Resonant Shunt Damper," *Journal of Vibration and Acoustics*, vol. 130, no. 4, p. 041003, 2008.

[102] J. Wang, G. W. Jewell, and D. Howe, "A general framework for the analysis and design of tubular linear permanent magnet machines," *IEEE Transactions on Magnetics*, vol. 35, no. 3, pp. 1986–2000, 1999.

[103] A. L. K.-T. Wong, "Novel semi-active suspension with tunable stiffness and damping characteristics," 2013.

[104] R. Sabzehgar and M. Moallem, "Modeling and control of a three-phase boost converter for resistive input behavior," *IEEE Transactions on Industrial Electronics*, vol. 60, no. 12, pp. 5854–5863, 2013.

[105] H. K. Fathy, P. Y. Papalambros, A. G. Ulsoy, and D. Hrovat, "Nested plant/controller optimization with application to combined passive/active automotive suspensions," in *American Control Conference, 2003. Proceedings of the 2003*, vol. 4, pp. 3375–3380, IEEE, 2003.

[106] B. L. Gysen, J. J. Paulides, J. L. Janssen, and E. A. Lomonova, "Active electromagnetic suspension system for improved vehicle dynamics," *IEEE Transactions on Vehicular Technology*, vol. 59, no. 3, pp. 1156–1163, 2010.

[107] Ö. Gündoğdu, "Optimal seat and suspension design for a quarter car with driver model using genetic algorithms," *International Journal of Industrial Ergonomics*, vol. 37, no. 4, pp. 327–332, 2007.

[108] J. Tamboli and S. Joshi, "Optimum design of a passive suspension system of a vehicle subjected to actual random road excitations," *Journal of sound and vibration*, vol. 219, no. 2, pp. 193–205, 1999.

[109] G. Verros, S. Natsiavas, and C. Papadimitriou, "Design optimization of quarter-car models with passive and semi-active suspensions under random road excitation," *Journal of Vibration and Control*, vol. 11, no. 5, pp. 581–606, 2005.

[110] G. Georgiou, G. Verros, and S. Natsiavas, "Multi-objective optimization of quarter-car models with a passive or semi-active suspension system," *Vehicle System Dynamics*, vol. 45, no. 1, pp. 77–92, 2007.

[111] N. Srinivas and K. Deb, "Muiltiobjective optimization using nondominated sorting in genetic algorithms," *Evolutionary computation*, vol. 2, no. 3, pp. 221–248, 1994.

[112] R. T. Marler and J. S. Arora, "Survey of multi-objective optimization methods for engineering," *Structural and multidisciplinary optimization*, vol. 26, no. 6, pp. 369–395, 2004.

[113] H. Gao, J. Lam, and C. Wang, "Multi-objective control of vehicle active suspension systems via load-dependent controllers," *Journal of Sound and Vibration*, vol. 290, no. 3, pp. 654–675, 2006.

[114] M. Gobbi and G. Mastinu, "Analytical description and optimization of the dynamic behaviour of passively suspended road vehicles," *Journal of sound and vibration*, vol. 245, no. 3, pp. 457–481, 2001.

[115] M. Gobbi, F. Levi, and G. Mastinu, "Multi-objective stochastic optimisation of the suspension system of road vehicles," *Journal of sound and vibration*, vol. 298, no. 4, pp. 1055–1072, 2006.

[116] N. Jalili, "A comparative study and analysis of semi-active vibration-control systems," *Journal of vibration and acoustics*, vol. 124, no. 4, pp. 593–605, 2002.

[117] N. Nariman-Zadeh, M. Salehpour, A. Jamali, and E. Haghgoo, "Pareto optimization of a five-degree of freedom vehicle vibration model using a multi-objective uniform-diversity genetic algorithm (muga)," *Engineering Applications of Artificial Intelligence*, vol. 23, no. 4, pp. 543–551, 2010.

[118] J. H. Crews, M. G. Mattson, and G. D. Buckner, "Multi-objective control optimization for semi-active vehicle suspensions," *Journal of sound and Vibration*, vol. 330, no. 23, pp. 5502–5516, 2011.

[119] C. M. Fonseca and P. J. Fleming, "An overview of evolutionary algorithms in multi-objective optimization," *Evolutionary computation*, vol. 3, no. 1, pp. 1–16, 1995.

[120] R. G. D'Souza, K. C. Sekaran, and A. Kandasamy, "Improved nsga-ii based on a novel ranking scheme," *arXiv preprint arXiv:1002.4005*, 2010.

[121] K. Deb, A. Pratap, S. Agarwal, and T. Meyarivan, “A fast and elitist multiobjective genetic algorithm: Nsga-ii,” *IEEE transactions on evolutionary computation*, vol. 6, no. 2, pp. 182–197, 2002.

[122] M. Ataei and A. Yousefi-Koma, “Three-dimensional optimal path planning for waypoint guidance of an autonomous underwater vehicle,” *Robotics and Autonomous Systems*, vol. 67, pp. 23–32, 2015.

[123] M. Ataei, A. Yousefi-Koma, and M. S. Panahi, “Multicriterion offline path planning of a biomimetic underwater vehicle using nsga ii,” in *ASME 2010 10th Biennial Conference on Engineering Systems Design and Analysis*, pp. 737–741, American Society of Mechanical Engineers, 2010.

[124] M. Ataei, E. Asadi, A. Goodarzi, A. Khajepour, and M. B. Khamesee, “Multi-objective optimization of a hybrid electromagnetic suspension system for ride comfort, road holding and regenerated power,” *Journal of Vibration and Control*, p. 1077546315585219, 2015.

[125] L. Zuo and S. A. Nayfeh, “Structured h2 optimization of vehicle suspensions based on multi-wheel models,” *Vehicle System Dynamics*, vol. 40, no. 5, pp. 351–371, 2003.

[126] L. Zuo and P.-S. Zhang, “Energy harvesting, ride comfort, and road handling of regenerative vehicle suspensions,” *Journal of Vibration and Acoustics*, vol. 135, no. 1, p. 011002, 2013.

[127] ISO, *Mechanical Vibration and Shock: Evaluation of Human Exposure to Whole-body Vibration. Part 1, General Requirements: International Standard ISO 2631-1: 1997 (E).* ISO, 1997.

[128] L. Zuo and S. Nayfeh, “Low order continuous-time filters for approximation of the iso 2631-1 human vibration sensitivity weightings,” *Journal of sound and vibration*, vol. 265, no. 2, pp. 459–465, 2003.

[129] D. Hrovat, “Applications of optimal control to advanced automotive suspension design,” *Transactions-american Society Of Mechanical Engineers Journal Of Dynamic Systems Measurement And Control*, vol. 115, pp. 328–328, 1993.

[130] N. Derby and S. Olbert, “Cylindrical magnets and ideal solenoids,” *American Journal of Physics*, vol. 78, no. 3, pp. 229–235, 2010.

[131] W. Robertson, B. Cazzolato, and A. Zander, “A simplified force equation for coaxial cylindrical magnets and thin coils,” *IEEE Transactions on Magnetics*, vol. 47, no. 8, pp. 2045–2049, 2011.

[132] E. Asadi, A. Khajepour, and M. B. Khamesee, “A new low-profile electromagnetic-pneumatic actuator for high bandwidth applications,” *Submitted To Ieee/asme Transaction On Mechatronics*, 2016.

[133] N. ODA and S. Nishimura, “Vibration of air suspension bogies and their design,” *Bulletin of JSME*, vol. 13, no. 55, pp. 43–50, 1970.

[134] J. Evans and M. Berg, “Challenges in simulation of rail vehicle dynamics,” *Vehicle System Dynamics*, vol. 47, no. 8, pp. 1023–1048, 2009.

[135] M. Berg, “A three-dimensional airspring model with friction and orifice damping,” in *The Dynamics Of Vehicles On Roads And On Tracks-supplement To Vehicle System Dynamics, Volume 33. Proceedings Of The 16th Iavsd Symposium Held In Pretoria, South Africa, August 30-September 3, 1999*, 2000.

[136] Y. Shtessel, C. Edwards, L. Fridman, and A. Levant, *Sliding mode control and observation.* Springer, 2014.

APPENDICES

Appendix A

Analytical Solution for σ (the RMS Values of the Selected Objective Functions)

The values of $\sigma_{\ddot{x}_s}$, σ_{x_1-y} and σ_{f_e} are analytically evaluated using the following approach. For an integral of the form:

$$I = \int_{-\infty}^{\infty} \frac{f_n(\omega)f_n(-\omega)}{g_n(\omega)g_n(-\omega)} d\omega \tag{A.1}$$

where

$$\begin{aligned} f_n(\omega)f_n(-\omega) &= b_0\omega^{2n-2} + b_1\omega^{2n-4} + ... + b_{n-1} \\ g_n(\omega) &= a_0\omega^n + a_1\omega^{n-1} + ... + a_n \end{aligned} \tag{A.2}$$

The analytical solution is:

$$I = \frac{\pi i M_n}{a_0 \triangle_n} \tag{A.3}$$

where

$$M_n = \begin{vmatrix} b_0 & b_1 & b_2 & \cdots & \cdots & \cdots & b_{n-1} \\ a_0 & a_2 & a_4 & \cdots & \cdots & \cdots & 0 \\ 0 & a_1 & a_3 & a_5 & \cdots & \cdots & 0 \\ 0 & a_0 & a_2 & a_4 & . & . & . \\ \vdots & 0 & a_1 & a_3 & . & . & . \\ \vdots & \vdots & \vdots & \vdots & \vdots & \vdots & \vdots \\ 0 & 0 & . & . & . & a_{n-2} & a_n \end{vmatrix}_{n\times n}$$

$$\triangle_n = \begin{vmatrix} a_1 & a_3 & a_5 & \cdots & 0 & 0 & 0 \\ a_0 & a_2 & a_4 & \cdots & \cdots & \cdots & 0 \\ 0 & a_1 & a_3 & a_5 & \cdots & \cdots & 0 \\ 0 & a_0 & a_2 & a_4 & . & . & . \\ \vdots & 0 & a_1 & a_3 & . & . & . \\ \vdots & \vdots & \vdots & \vdots & \vdots & \vdots & \vdots \\ 0 & 0 & . & . & . & a_{n-2} & a_n \end{vmatrix}_{n\times n} \tag{A.4}$$